Analyses of Quark Helicity Distributions in the Polarized Nucleon Measured at HERMES

by

Hiroshi Ohsuga

Thesis submitted to Department of Physics in partial
fulfillment of the requirements for the degree of

Doctor of Science

at Tokyo Institute of Technology

February 2005

Abstract

Quark helicity distributions were measured by experiment at DESY-HERA HERMES. The HERMES experiment measures the spin structure of the nucleon with Deep Inelastic Scattering (DIS) of 27.6 GeV longitudinally polarized positron beam at HERA and longitudinally polarized gas targets (H, D). The experiment was motivated to solve the "nucleon spin puzzle" found by the EMC experiment in 1988.

HERMES uses the Ring Imaging CHerenkov (RICH) detector which has dual radiators: aerogel and $\mathrm{C_4F_{10}}$ gas. The RICH allows us to identify pions, kaons and protons in the momentum region of 2 - 15 GeV/c. Hadrons are detected in coincidence with the scattered positron. HERMES is the first DIS experiment with a full hadron identification capability. Using informations from the RICH, cross section asymmetries between the parallel and anti-parallel configuration of the beam and target spins were measured for charged pions and kaons separately for the first time. From the measured double spin asymmetries, helicity distributions of individual quark flavors were extracted for $u, \bar{u}, d, \bar{d}$ and s.

Main focuses of this thesis are 1) evaluation of efficiency of the hadron identification with RICH, and 2) evaluation of systematic uncertainties in the quark helicity distributions due to uncertainties on the unpolarized parton distribution functions (PDFs) used in the analyses. The uncertainty in the hadron identification with RICH is mainly due to imperfection of the RICH description in the HERMES Monte Carlo simulation. The estimation of the hadron identification efficiency was performed by hadron tagging using 'decaying particle method' which

uses decaying particles such as $\rho, \phi, \Lambda, K_s^0$ in the experimental data. The evaluated RICH uncertainty was propagated to the systematic error on the double spin asymmetries. The effect of the uncertainties in the unpolarized PDFs was evaluated using the 40 eigenvector PDF sets of the CTEQ6.1M parameterization. The quark helicity distributions are obtained by HERMES with high precision in a self-consistent way with less assumptions in the analysis than any of previous experiments, making use of its hadron identification capabilities.

Contents

List of Figures

List of Tables

Chapter 1

Introduction

In 1950s, a number of new pion-like or proton-like particles were discovered. Gell-Mann and Ne'eman proposed the "Eightfold Way" in 1961 which is a theory to classify the particles into groups based on properties of SU(3) symmetries. This theory predicted the existence of a heavy subatomic particle. The particle was discovered by an experiment at Brookhaven National Laboratory in 1963 and was called Ω^-. In the same year (and after the discovery of Ω^-), Gell-Mann [1] and Zweig [2] independently developed a theory that three different particles, which was called "quarks" by Gell-Mann, constructed so-called baryons and a quark and an anti-quark make up mesons. In 1968, this quark model was confirmed by a Rutherford-type experiment at SLAC by Friedman, Kendall and Taylor. The experiment also showed scaling behavior of unpolarized structure functions $F_1(x, Q^2), F_2(x, Q^2)$ which depend on the properties of the target:

$$\begin{aligned} F_1(x, Q^2) &\rightarrow F_1(x), \\ F_2(x, Q^2) &\rightarrow F_2(x), \end{aligned}$$

where x is Bjørken x and Q^2 the squared invariant mass of the virtual photon. Since this feature was found by a suggestion by Bjørken, the scaling was called Bjørken scaling.

In the same year, to give an explanation of the the Bjørken scaling, Feynman proposed [3] the Parton Model based on an idea that the nucleon was constructed from point-like particles which was called "partons". Later the partons were identified with the quarks and the Quark Parton Model (QPM) was established.

In late 1970s, SLAC E80 [4, 5] and E130 [6] performed the measurements of the double spin asymmetries for the deep inelastic scattering of longitudinally polarized electrons off longitudinally polarized protons. The polarized structure functions $g_1(x)$ was extracted from the asymmetry data and was integrated over x. The experiment covered the region of $0.1 < x < 0.64$ and extrapolated outside the measured region. Though their conclusion was consistent with a theoretical prediction by Ellis and Jaffe, the extrapolation at lower x was not clear while the behavior of the polarized structure function can be expected to fall smoothly at higher x. Precise measurements of the polarized structure function extended to lower x was performed by European Muon Collaboration (EMC) [7, 8] in 1987. The result showed that only 12 % of the proton spin was contributed from the quark spins. This fact led to the so-called $spin\ crisis$. Afterward the polarized spin structure function g_1 was measured at Spin Muon Collaboration (SMC) [9] and at SLAC [10, 11], and the result of the EMC was confirmed. The spin of the neutron was also investigated.

The nucleon spin can be written as

$$\frac{1}{2} = \frac{1}{2}\Delta\Sigma + \Delta G + L_q + L_g, \tag{1.1}$$

where $\Delta\Sigma$ and ΔG are contributions from the quark and gluon spins respectively and L_q and L_g are their orbital angular momentum.

The HERMES experiment performed measurements of the Deep Inelastic Scattering (DIS) cross section of the polarized positron beam at HERA and polarized gas targets (H, D). This thesis presents polarizations of u, d, s quarks and the corresponding anti-quarks determined by the HERMES experiment.

In 2000 H. Kobayashi reported results of the polarized quark distributions in [12]. His analysis is based on 4 independent input asymmetries for the proton target from the 1996 and 1997 data taking periods. Various decomposition of the polarized quark distributions were performed. In 2001 F. Sato performed a 5 parameter fit of $(\Delta u, \Delta d, \Delta\bar{u}, \Delta\bar{d}, \Delta s = \Delta\bar{s})$ using the DIS events accumulated from 1995 to 1998 [13]. Now the DIS events collected during the 1996 to 2000 data taking periods are analyzed (We excluded 1995 data for $^3\mathrm{He}$ because it was found that contributions from elastic scattering process was large.) In particular 5 million DIS events were taken in 2000 and it improves the statistics substantially.

This thesis will describes the extraction of the contributions of different quark flavors to the nucleon spin. In chapter 2, the spin structure of the nucleon is described. The HERMES experiment is described in chapter 3. The Ring Imaging Čerenkov detector at HERMES is presented in chapter 4. In chapter 5, asymmetries measured at the HERMES experiment are described. The quark polarizations and helicity distributions determined by using these asymmetries are presented in

Experiment			
Year	Collaboration	Main Results	Ref.
1950s		A number of new particles were discoverd.	
1967	SLAC	Weak Q^2 dependence of DIS cross section with increasing Q^2. Scaling of unpolarized structure function.	
1976, 1978	SLAC E80	Measurement of double spin asymmetries in polarized DIS.	[4, 5]
1983	SLAC E130	Consistent with the theory by Ellis and Jaffe.	[6]
1988	EMC	Spin crisis: The quarks in nucleon carried only 12 % of the nucleon spin.	[7, 8]
Theory			
Year	Theorist	Prediction	Ref.
1964	Gell-Man and Zweig	Quark Model: proposed independently by Gell-Man and Zweig.	[1]
1969	Feynman	Parton Model: the nucleon is constructed by three constitutent particles.	[3]
1972	Feynman	Quark Parton Model: The parton is consistent with the quark	[14]
1973	Ellis and Jaffe	Sum Rule: $\int dx g_1(x) \simeq 0.2$.	[15]

Table 1.1: Overview of investigations of the nucleon structure.

chapter 6.

Chapter 2

Spin Structure of the Nucleon

2.1 Deep Inelastic Scattering

Lepton-nucleon Deep Inelastic Scattering(DIS) is a powerful tool to investigate the spin structure of nucleon. In first order QED, the DIS process is described by one photon exchange. Figure 2.1 shows a schematic view of the DIS process. An incoming lepton is scattered off a target nucleon. Then the nucleon is broken and forms a final hadronic state:

$$l + N \rightarrow l' + X \tag{2.1}$$

where l and l' are the incoming and the scattered lepton respectively, N the nucleon and X the final hadronic state. In inclusive measurements only the scattered lepton is detected, while at least one hadron in the final hadronic system X is detected in coincidence with the lepton in semi-inclusive measurements.

2.1.1 Kinematics of the Deep-inelastic Scattering

In this section, kinematic variables used in a DIS process are defined. The DIS process can be characterized by two kinematic variables. This thesis mainly uses the following two variables:

$$\begin{aligned} Q^2 &= -q^2 = -(k-k')^2 \overset{\text{lab}}{=} 4EE' \sin^2\frac{\theta}{2}, && (2.2) \\ x &= \frac{Q^2}{2P\cdot q} \overset{\text{lab}}{=} \frac{Q^2}{2M\nu}, && (2.3) \end{aligned}$$

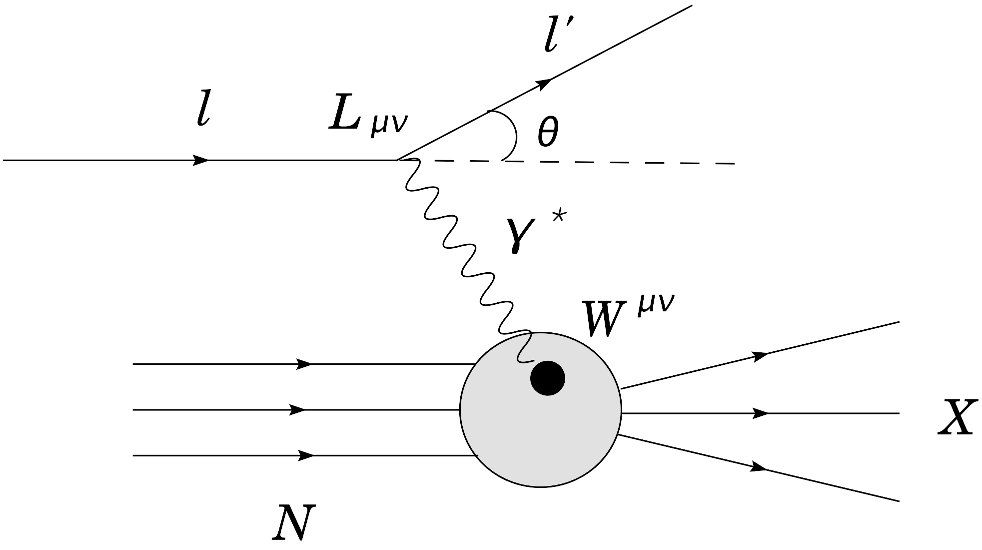

Figure 2.1: Schematic view of the deep inelastic scattering process.

where $k \overset{\text{def}}{=} (E, \vec{\boldsymbol{k}})$ and $k' \overset{\text{def}}{=} (E', \vec{\boldsymbol{k'}})$ are four-momenta of the incoming and the scattered lepton respectively, θ the polar angle of the scattered lepton, M the mass of the nucleon, P and q four momenta of the target nucleon and the virtual photon exchanged between the lepton and the nucleon, and ν the energy of the virtual photon. The former variable Q^2 expresses the negative square of the four-momentum of the virtual photon. The latter variable x is the Bjørken scaling variable. This variable can be interpreted as the fractional momentum of the quark which absorbs the virtual photon to the momentum of the nucleon. In elastic scattering x is equal to 1, while $x < 1$ corresponds to inelastic scattering. A squared invariant mass of the hadronic final system X is

$$W^2 = (P+q)^2 \overset{\text{lab}}{=} M^2 + 2M\nu - Q^2. \tag{2.4}$$

The resonance region where the nucleon is not broken but goes to an excited state and the DIS region are defined by

$$\begin{array}{rclr} W & \leq & 2\,\text{GeV} & \text{for the resonance region,} \\ W & > & 2\,\text{GeV} & \text{for the DIS region.} \end{array} \tag{2.5}$$

For semi-inclusive measurements, a fractional energy of the virtual photon carried by the hadron h is introduced:

$$z = \frac{P_\mu P^\mu}{P_\mu q^\mu} \overset{\text{lab}}{=} \frac{E_h}{\nu}. \tag{2.6}$$

The Feynman scaling variable in the hadronic center mass system is defined by

$$x_F = \frac{|\vec{p_L}|}{|\vec{q}|}, \tag{2.7}$$

where $\vec{p_L}$ represents the longitudinal hadron momentum in the hadronic center mass system. The other kinematic variables are presented in Table 2.1.

2.1.2 DIS cross section

The DIS differential cross section for inclusive measurement in the lowest order QED can be written as [16]

$$\frac{d^2\sigma}{d\Omega dE'} = \frac{\alpha^2}{2MQ^4}\frac{E'}{E}L_{\mu\nu}W^{\mu\nu}, \tag{2.8}$$

where α represents the electromagnetic coupling constant and $L_{\mu\nu}$ and $W^{\mu\nu}$ the lepton and hadron tensors, respectively. The both tensors can be split into symmetrical and anti-symmetrical parts (indicated as superscripts (S) and (A) respectively) as

$$L_{\mu\nu} = L_{\mu\nu}^{(S)} + iL_{\mu\nu}^{(A)}, \tag{2.9}$$

$$W_{\mu\nu} = W_{\mu\nu}^{(S)} + iW_{\mu\nu}^{(A)}, \tag{2.10}$$

where

$$L_{\mu\nu}^{(S)} = 2\left[k_\mu k'_\nu + k_\nu k'_\mu - g_{\mu\nu}(k\cdot k' - m_e^2)\right], \tag{2.11}$$

$$L_{\mu\nu}^{(A)} = 2m_e\epsilon_{\mu\nu\alpha\beta}s^\alpha(k-k')^\beta, \tag{2.12}$$

where $g_{\mu\nu}$ is the metric tensor, m_e the mass of the lepton, $\epsilon_{\mu\nu\alpha\beta}$ the totally anti-symmetric Levi-Civita tensor and $s \overset{\text{lab}}{=} \frac{1}{m_e}(|\vec{\boldsymbol{k}}|, \frac{\vec{\boldsymbol{k}}}{|\vec{\boldsymbol{k}}|}E)$ spin four-vector of the incident positron for longitudinal polarization. These lepton tensors can be exactly obtained in QED calculation.

Positron beam and Target nucleon	
$k^\mu = (E, \vec{\boldsymbol{k}})$	Four-momentum of the incident proton
$k'^\mu = (E', \vec{\boldsymbol{k'}})$	Four-momentum of the scatterd lepton
θ, ϕ	Polar and azimuthal angles of the scatted lepton
$P^\mu \overset{\text{lab}}{=} (M, \vec{0})$	Four-momentum of the target nucleon

Inclusive DIS	
$\nu = \frac{P_\mu q^\mu}{M} \overset{\text{lab}}{=} E - E'$	Energy of the virtual photon
$q^\mu = k^\mu - k'^\mu = (\nu, \vec{q})$	Four-momentum of the virtual photon
$Q^2 = -q_\mu q^\mu \overset{\text{lab}}{\cong} 4EE' \sin^2 \frac{\theta}{2}$	Squared invariant mass of the virtual photon
$W^2 = (P^\mu + q^\mu)^2 \overset{\text{lab}}{=} M^2 + 2M\nu - Q^2$	Squared mass of the final hadronic state
$x = \frac{Q^2}{2P_\mu q^\mu} \overset{\text{lab}}{=} \frac{Q^2}{2M\nu}$	Bjørken scaling variable
$y = \frac{P_\mu q^\mu}{P_\mu k^\mu} \overset{\text{lab}}{=} \frac{\nu}{E}$	Fractional energy transfer of the virtual photon

Semi inclusive DIS	
$z = \frac{P_\mu P^\mu}{P_\mu q^\mu} \overset{\text{lab}}{=} \frac{E_h}{\nu}$	Fractional energy of the virtual photon carried by a hadron h
$\vec{p_L} = (\vec{p_h} \cdot \frac{\vec{q}}{\lvert\vec{q}\rvert}) \frac{\vec{q}}{\lvert\vec{q}\rvert}$	Longitudinal momentum of a hadron in γN c.m. frame
$\vec{p_T} = \vec{p_h} - \vec{p_L}$	Transverse momentum of a hadron in γN c.m. frame
$x_F = \frac{\lvert\vec{p_L}\rvert}{\lvert\vec{q}\rvert} \cong \frac{2\vec{p_L}}{W}$	Feynman scaling variable

Table 2.1: Definition of kinematic quantities in DIS.

The Unpolarized Cross Section

The hadron tensor is more complicated since the hadron is not a point-like particle. In case that the leptons are unpolarized, the unpolarized differential cross section can be expressed as the product of the lepton and the hadron symmetrical parts:

$$\frac{d^2\sigma}{d\Omega dE'} = \frac{\alpha^2}{2MQ^4}\frac{E'}{E}L^{(S)}_{\mu\nu}W^{\mu\nu}_{(S)}, \tag{2.13}$$

where

$$W^{(S)}_{\mu\nu} = 2\left(-g_{\mu\nu} - \frac{q_\mu q_\nu}{Q^2}\right)F_1(x,Q^2) + \left(P_\mu + \frac{P\cdot q}{Q^2}q_\mu\right)\left(P_\nu + \frac{P\cdot q}{Q^2}q_\nu\right)\frac{F_2(x,Q^2)}{P\cdot q}, \tag{2.14}$$

where $F_1(x,Q^2)$ and $F_2(x,Q^2)$ are dimensionless unpolarized structure functions which are Lorentz-invariant and explain the internal structure of the nucleon. In the Bjørken limit (ν $\mathrm{(energy\ of\ virtual\ photon)}$ $\rightarrow \infty$ and $Q^2 \rightarrow \infty$ with x finite), the two structure functions are scaling as

$$F_1(x,Q^2) \rightarrow F_1(x), \tag{2.15}$$
$$F_2(x,Q^2) \rightarrow F_2(x). \tag{2.16}$$

This scaling was observed by a Rutherford-type experiment at SLAC by Friedman, Kendall and Taylor. However the concept had been suggested by Bjørken and therefore the scaling is called Bjørken scaling. Furthermore these structure functions are related each other, which is known as Callan-Gross relation [17]:

$$2xF_1(x) = F_2(x). \tag{2.17}$$

These structure functions were measured with various fixed targets at EMC [18], BCDMS [19], E665 [20], NMC [21] and SLAC [22], and in e-p collisions at H1 [23] and ZEUS [24, 25]. Figure2.2 [26] shows the structure function $F_2(x,Q^2)$ measured by these experiments.

From Eq. (2.11) and Eq. (2.14), the unpolarized differential cross section can be written as

$$\frac{d^2\sigma}{d\Omega dE'} = \left(\frac{d\sigma}{d\Omega}\right)_{\mathrm{Mott}}\frac{\pi}{EE'x}\left(F_2(x,Q^2) + \frac{2\mu}{M}F_1(x,Q^2)\tan^2\frac{\theta}{2}\right), \tag{2.18}$$

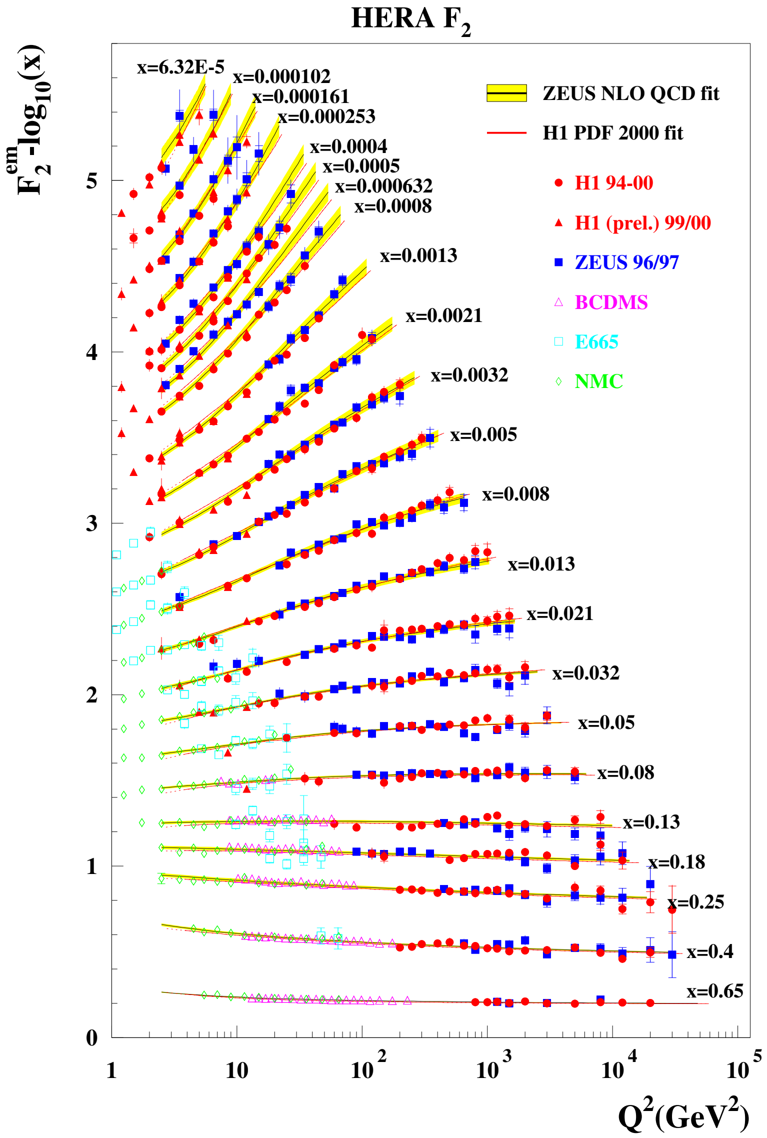

Figure 2.2: The structure function measured as a function of Q^2 for various x. The data are offset by $-\log_{10}(x)$ for better presentation.

where

$$\left(\frac{d\sigma}{d\Omega}\right)_{\text{Mott}} = \frac{4\alpha^2 E'^2}{Q^4}\cos^2\frac{\theta}{2}. \tag{2.19}$$

The Mott cross section is the Rutherford cross section at relativistic energy which includes effects of the lepton spin.
Eq. (2.18) can alternatively be expressed in terms of the photo-absorption cross sections $\sigma_L(x,Q^2)$ and $\sigma_T(x,Q^2)$ for longitudinally and transversely polarized virtual photons on a nucleon:

$$\frac{d^2\sigma}{d\Omega dE'} = \frac{\alpha}{2\pi^2 Q^2}\frac{\mu^2(1-x)}{E^2 x(1-\varepsilon)}\left(\sigma_T(x,Q^2) + \varepsilon\sigma_L(x,Q^2)\right), \tag{2.20}$$

where

$$\varepsilon = \frac{1-y-0.25\gamma^2 y^2}{1-y+0.25y^2(\gamma^2+2)}, \tag{2.21}$$

where the assumption of $2m_e^2 \ll Q^2$ is used and $\gamma \equiv \frac{Q^2}{\nu^2}$. The ratio of the photo absorption cross sections $R(x,Q^2) = \frac{\sigma_L(x,Q^2)}{\sigma_T(x,Q^2)}$ was measured by the several experiments [27]. The ratio R can be related to the unpolarized structure functions $F_1(x,Q^2)$ and $F_2(x,Q^2)$ as

$$R(x,Q^2) = \frac{1+\gamma^2}{2x}\frac{F_2(x,Q^2)}{F_1(x,Q^2)} - 1. \tag{2.22}$$

Hence the structure function $F_2(x,Q^2)$ can be written with $F_1(x,Q^2)$ and $R(x,Q^2)$

$$F_1(x,Q^2) = \frac{1+\gamma^2}{2x(1+R(x,Q^2))}F_2(x,Q^2). \tag{2.23}$$

In the Bjørken limit, the photo-absorption cross section σ_L vanishes due to helicity conservation. In this limit, $R(x,Q^2) \to 0$ and Eq. (2.23) is close to Eq. (2.17).

Polarized Cross Section

For the longitudinally polarized lepton, the anti-symmetric hadron tensor

$$W_{\mu\nu}^{(A)} = \frac{\epsilon_{\mu\nu\alpha\beta}q^\alpha}{\nu}\left[S^\beta g_1(x,Q^2) + \left(S^\beta - \frac{S\cdot q}{P\cdot q}P^\beta\right)g_2(x,Q^2)\right], \tag{2.24}$$

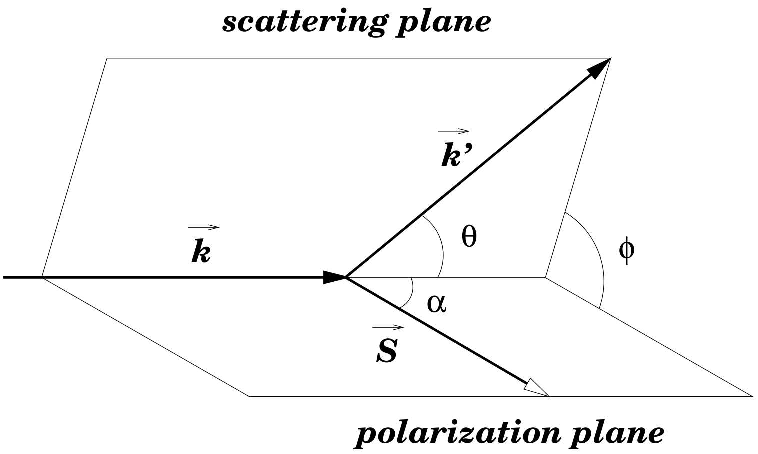

Figure 2.3: The definition of angles. Here $\vec{\boldsymbol{k}}$ and $\vec{\boldsymbol{k}}'$ are momentum vectors of the incoming and scattered lepton respectively, $\vec{\boldsymbol{S}}$ is the spin polarization vector of the target, angles θ and ϕ represent the polar angle with respect to $\vec{\boldsymbol{k}}$ and azimuthal angle which is defined by an angle between scattering plane and polarization plane. The additional angle α is the angle between $\vec{\boldsymbol{k}}$ and $\vec{\boldsymbol{S}}$.

appears in the DIS cross section. Here $g_1(x, Q^2)$ and $g_2(x, Q^2)$ are the polarized structure functions and S represents the spin polarization vector of the nucleon target. The definition of angles between the various vectors is shown in Figure 2.3.

The two polarized structure functions can be obtained by the cross section difference as

$$\frac{d^2\sigma^{\overset{\rightarrow}{\Leftarrow}}}{dxdQ^2} - \frac{\sigma^{\overset{\rightarrow}{\Rightarrow}}}{dxdQ^2} = \frac{8\pi\alpha^2}{Q^4}\frac{y}{E} \cdot \left[(E + E' \cos\theta)\, g_1(x, Q^2) - \frac{Q^2}{\nu} g_2(x, Q^2)\right], \tag{2.25}$$

where $\overset{\rightarrow}{\Rightarrow}$ and $\overset{\rightarrow}{\Leftarrow}$ indicate that the target and beam spins are aligned parallel ($\alpha = 0$ in Figure 2.3) or anti-parallel ($\alpha = \pi$), respectively. When the target is transversely polarized, the cross section difference can be written as

$$\frac{d^2\sigma^{\rightarrow\Uparrow}}{dxdQ^2} - \frac{\sigma^{\rightarrow\Downarrow}}{dxdQ^2} = \frac{8\pi\alpha^2}{Q^4}\frac{y}{E} \cdot E' \cdot \sin\theta\cos\phi \left[g_1(x, Q^2) + \frac{2E}{\nu} g_2(x, Q^2)\right]. \tag{2.26}$$

The polarized structure function g_1 has been measured by fixed target experiments at E142 [28], E143 [29] E154 [30], E155 [31, 32], EMC [7, 8], SMC [33, 34] and HERMES [35, 36]. The measurements of other polarized structure function g_2 were performed by fixed target experiments at E142 [28], E143 [37], E154 [38], E155 [39, 40]. Figure 2.4 and Figure 2.5 show the x-weighted polarized structure functions $xg_1(x)$ and $xg_2(x)$ respectively.

The Q^2 dependence of the polarized structure function g_1 for proton and for neutron is shown in Figure 2.6. There is no evidence of strong Q^2 dependence of g_1.

2.2 Quark-Parton Model

To explain Bjørken scaling (Eq.(2.15)), the Parton Model is proposed by Feynman [3] in 1969. In the model, the nucleon is comprised of three point-like particles with spin-$\frac{1}{2}$ which are called partons. If it is true, the DIS process can be described as elastic scattering between a lepton and a parton. Later the Quark Parton Model (QPM) is proposed by Bjørken and Paschos [41] and Feynman [14]. In QPM, the partons are identical to the quarks which were proposed by Gell-Mann [1] and Zweig [2].

QPM can be formulated in the infinite momentum frame, where the target nucleon moves with infinite momentum, the mass and transverse momentum of parton are negligible and the fractional momentum of hadron is identical with the Bjørken x as follows:

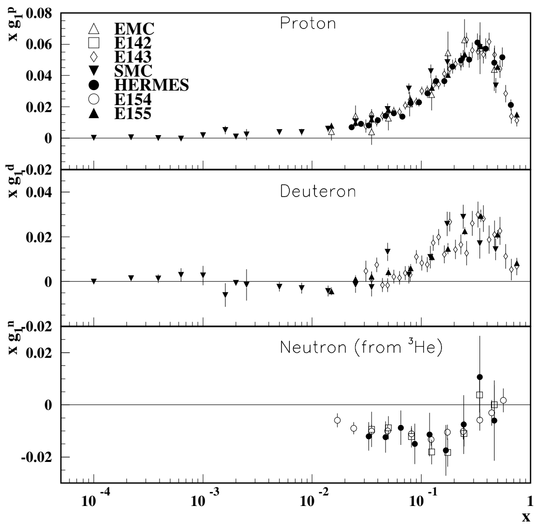

Figure 2.4: The x-weighted polarized structure function xg_1. The upper, middle and lower panels are those on the proton, the deuterium and the neutron respectively.

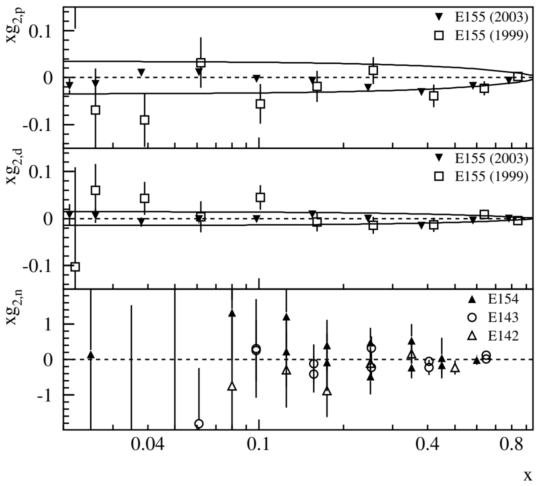

Figure 2.5: The x-weighted polarized structure function xg_2. The upper, middle and lower panels are those on the proton, the deuterium and the neutron respectively.

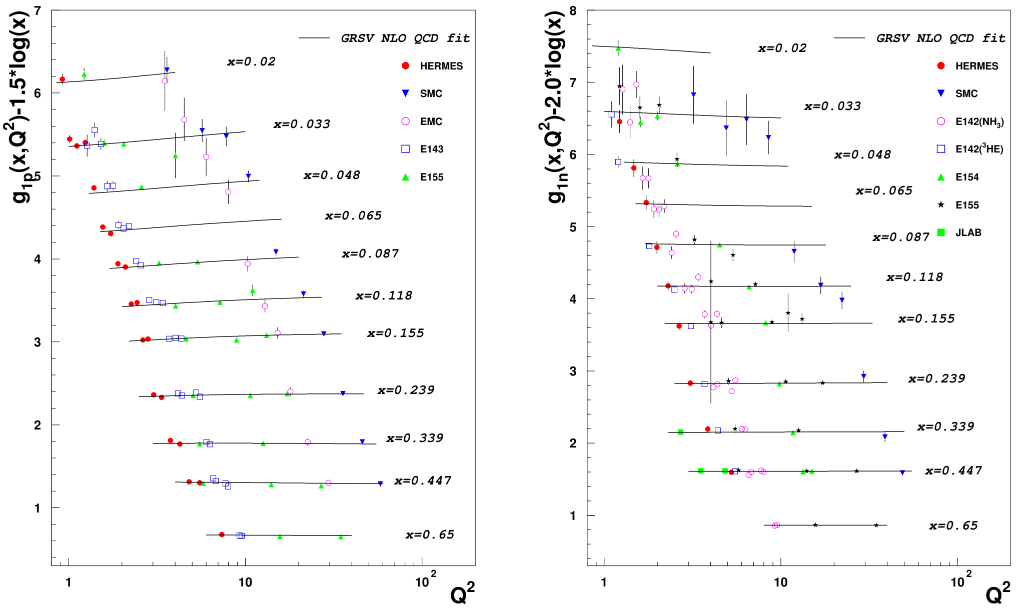

Figure 2.6: Q^2 dependence of the polarized structure function g_1 for proton (right panel) and for neutron (left panel).

The four-momentum of a parton can be expressed as

$$(\xi P + q)^2 = (m_q)^2, \tag{2.27}$$

where $P = (M, \vec{\mathbf{0}})$ and $q = (\nu, \vec{\boldsymbol{q}})$ are the four-momenta of the target and the virtual photon, and m_q is the mass of the parton and can be neglected. Hence the momentum fraction ξ becomes

$$\begin{aligned} \xi &= \frac{Q^2}{2M\nu}\frac{2}{1+\sqrt{1+\frac{Q^2}{\nu^2}}} \qquad (2.28) \\ &= \frac{2x}{1+\sqrt{q+\frac{4(Mx)^2}{Q^2}}}. \qquad (2.29) \end{aligned}$$

In the limit of $Q^2 \gg M^2$

$$\xi \simeq \frac{x}{1+\frac{(Mx)^2}{Q^2}} \simeq x. \tag{2.30}$$

Hence the Bjørken x indicates the fractional momentum of hadron.

The cross section for electron-parton scattering can be exactly calculated in QED. Assuming that each parton in the nucleon contributes to the inclusive DIS cross section incoherently, the structure functions $F_1(x)$ and $F_2(x)$ can be related to the quark densities $q(x)$ with the momentum fraction x as

$$\begin{aligned} F_1(x) &= \frac{1}{2}\sum_q e_q^2 q(x), \qquad (2.31) \\ F_2(x) &= x\sum_q e_q^2 q(x), \qquad (2.32) \end{aligned}$$

where e_q represents the charge of the parton in unit of e and the sum runs over all the quark flavors. For the nucleon, u, d, s and their anti-quarks are enough to express the structure functions. Analogously the polarized structure function $g_1(x)$ can be related to $q^{+(-)}$ which are the quark density for the parallel (anti-parallel) alignment of the quark spin and the target spin:

$$g_1(x) = \frac{1}{2}\sum_q e_q^2(q^+(x) - q^-(x)) \equiv \frac{1}{2}\sum_q e_q^2 \Delta q(x), \tag{2.33}$$

where $\Delta q(x)$ is the polarized quark density. As shown in Figure 2.5, g_2 is negligible compared to the size of g_1:

$$g_2(x) \simeq 0. \tag{2.34}$$

2.3 Cross Section Asymmetries

The cross section asymmetry is defined as

$$A_{||}(x, Q^2) = \frac{d\sigma^{\overset{\rightarrow}{\Leftarrow}} - d\sigma^{\overset{\rightarrow}{\Rightarrow}}}{d\sigma^{\overset{\rightarrow}{\Leftarrow}} + d\sigma^{\overset{\rightarrow}{\Rightarrow}}}, \tag{2.35}$$

where $\sigma^{\overset{\rightarrow}{\Leftarrow}}$ and $\sigma^{\overset{\rightarrow}{\Rightarrow}}$ indicate the differential cross sections $\frac{d^2\sigma^{\overset{\rightarrow}{\Leftarrow}}}{dxdQ^2}$ and $\frac{d^2\sigma^{\overset{\rightarrow}{\Rightarrow}}}{dxdQ^2}$ respectively. The two processes are illustrated in Figure 2.7. An advantage of the measurement of the asymmetry is to suppress systematic contributions such as efficiency and acceptance effects.

As already mentioned, the DIS process is interpreted as the interaction of a virtual photon with the target in lowest order QED. The photo-absorption asymmetries which are the cross section asymmetries for parallel and anti-parallel alignment of the target and virtual photon spins are given by

$$\begin{aligned} A_1 = \frac{\sigma_{\frac{1}{2}} - \sigma_{\frac{3}{2}}}{\sigma_{\frac{1}{2}} + \sigma_{\frac{3}{2}}} &= \frac{g_1 - \gamma^2 g_2}{F_1}, && (2.36) \\ A_2 = \frac{2\sigma_I}{\sigma_{\frac{1}{2}} + \sigma_{\frac{3}{2}}} &= \frac{\gamma(g_1 + g_2)}{F_1}, && (2.37) \end{aligned}$$

where $\sigma_{\frac{1}{2}(\frac{3}{2})}$ are the photo-absorption cross sections for the parallel (anti-parallel) alignments of the virtual photon and target spins (Figure 2.7) and σ_I is the interference cross section between the transverse and longitudinal polarization of the virtual photon. The experimentally accessible asymmetry $A_{||}$ can be related to the photo-absorption asymmetries A_1 and A_2:

$$A_{||} = D(A_1 + \eta A_2), \tag{2.38}$$

where D represents the depolarization factor of the virtual photon with respect to the polarization of the lepton. The variables D and η can be written as

$$\begin{aligned} D &= \frac{1 - (1 - y)\varepsilon}{1 + \varepsilon R}, && (2.39) \\ \eta &= \frac{\varepsilon \gamma y}{1 - (1 - y)\varepsilon}. && (2.40) \end{aligned}$$

From Eq. (2.36), (2.37) and (2.38), A_1 can be re-written as

$$A_1 = \frac{A_{||}}{D(1 + \eta\gamma)} - \frac{\eta\gamma(1 + \gamma^2)}{1 + \eta\gamma} \cdot \frac{g_2}{F_1}. \tag{2.41}$$

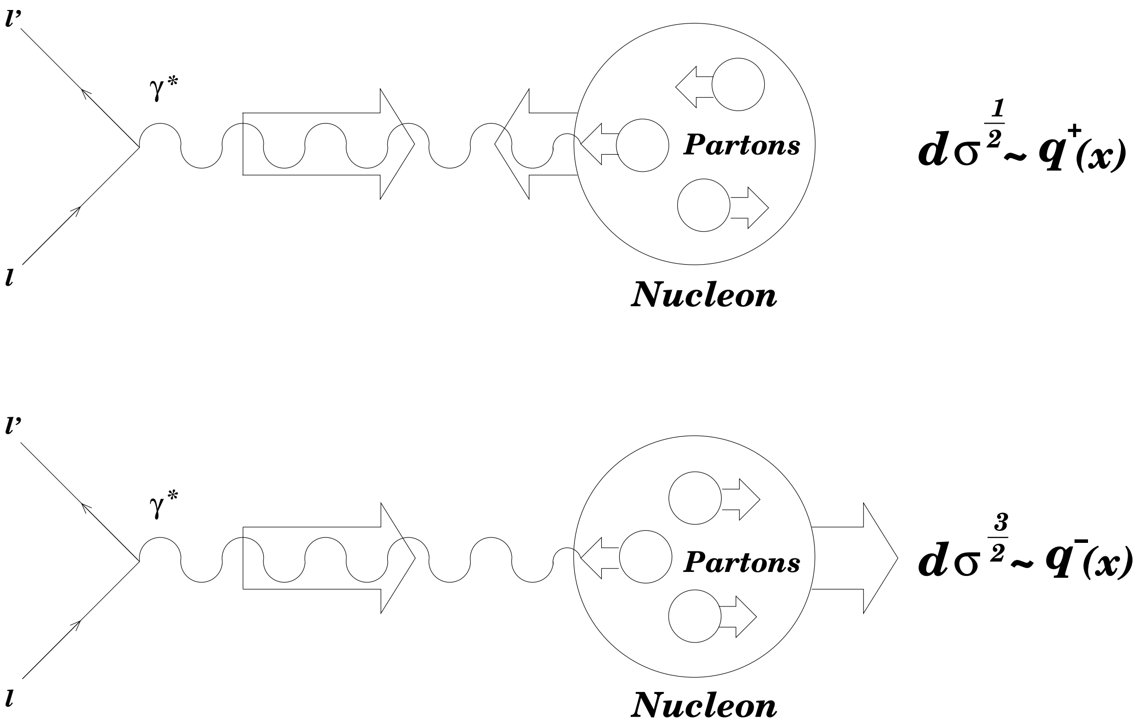

Figure 2.7: Schematic diagram of the polarized DIS in QPM. Arrows indicate the spins of the virtual photon, the partons and the nucleon.

Neglecting g_2, A_1 can be expressed as

$$A_1 \simeq \frac{A_{||}}{D(1+\eta\gamma)}. \tag{2.42}$$

2.4 Semi-inclusive Measurement of Deep Inelastic Scattering

In semi-inclusive measurements, at least one hadron h is detected in coincidence with the scattered lepton:

$$l + N \rightarrow l' + h + X. \tag{2.43}$$

In DIS process, a virtual photon is emitted from the incoming positron. The virtual photon is absorbed by a quark in the nucleon and the quark fragments into hadrons. Therefore the identification of the hadron is very important to access information on the struck quark. The hadrons in the final state can be separated into the current fragments and target fragments [42]. In the current fragmentation region the flavor of the struck quark and the types of produced hadrons have a strong correlation, while the target fragments relate to the spectator remnant of the nucleon. The EMC collaboration found that the fast-forward hadron contains the struck quark with high probability [43]. To select the fast-forward hadron in the DIS events, the cuts on kinematic variables z and x_F are used.

The differential cross section for the semi-inclusive measurement of DIS can be obtained as

$$\frac{d^3\sigma^h(x,Q^2,z)}{dxdQ^2dz} = \frac{d^2\sigma_{inc}(x,Q^2)}{dxdQ^2} \cdot \frac{\sum_f e_f^2 q_f(x,Q^2) D_f^h(z,Q^2)}{\sum_f e_f^2 q_f(x,Q^2)}, \tag{2.44}$$

where the sum runs over all the quark flavors, $\frac{d^2\sigma_{inc}(x,Q^2)}{dxdQ^2}$ is the inclusive differential cross section, D_f^h represents the fragmentation function which is the probability that a quark of flavor f hadronizes into a hadron of type h with an energy fraction z of the energy of the virtual photon. The fragmentation function is described in detail in Section 6.2.1. Under the assumption that the fragmentation functions are spin-independent, the unpolarized and the polarized structure function can be modified as

$$F_1^h(x,Q^2,z) \;=\; \frac{1}{2}\sum_f e_f^2 q_f(x,Q^2) D_f^h(z,Q^2), \tag{2.45}$$

$$g_1^h(x,Q^2,z) \;=\; \frac{1}{2}\sum_f e_f^2 \Delta q_f(x,Q^2) D_f^h(z,Q^2). \tag{2.46}$$

From Eq. (2.36) and the assumption of $g_2 = 0$, the semi-inclusive photo-absorption asymmetries can be obtained as

$$\begin{aligned} A_1^h(x,Q^2) &\simeq \frac{\int dz g_1^h(x,Q^2,z)}{\int dz F_1^h(x,Q^2,z)} \\ &= \frac{\sum_f e_f^2 \Delta q_f(x,Q^2) \int dz D_f^h(z,Q^2)}{\sum_f e_f^2 q_f(x,Q^2) \int dz D_f^h(z,Q^2)} \end{aligned} \tag{2.47}$$

2.5 Sum Rules

The n-th moment $\Gamma_1^n(S_1^n)$ of the polarized (unpolarized) structure function $g_1(F_1)$ is defined as

$$\Gamma_1^n \;\equiv\; \int_0^1 dx\, x^{(n-1)} g_1(x,Q^2), \tag{2.48}$$

$$S_1^n \;\equiv\; \int_0^1 dx\, x^{(n-1)} F_1(x,Q^2). \tag{2.49}$$

In addition, the first moments of the polarized quark density $\Delta q(x)$ is defined as

$$\Delta q = \int_0^1 dx\, \Delta q(x). \tag{2.50}$$

The proton matrix elements a_i are the expectation values of axial vector currents $J_{5\mu}^i$ defined by

$$2Ma_0 S_\mu \;=\; \langle P,S|J_{5\mu}^0|P,S\rangle, \tag{2.51}$$

$$Ma_3 S_\mu \;=\; \langle P,S|J_{5\mu}^3|P,S\rangle, \tag{2.52}$$

$$Ma_8 S_\mu \;=\; \langle P,S|J_{5\mu}^8|P,S\rangle. \tag{2.53}$$

They can be related to the first moments Δq as

$$a_0 \;=\; \Delta\Sigma = (\Delta u + \Delta\bar{u}) + (\Delta d + \Delta\bar{d}) + (\Delta s + \Delta\bar{s}), \tag{2.54}$$

$$a_3 \;=\; \left|\frac{g_A}{g_V}\right| = (\Delta u + \Delta\bar{u}) - (\Delta d + \Delta\bar{d}), \tag{2.55}$$

$$a_8 \;=\; (\Delta u + \Delta\bar{u}) + (\Delta d + \Delta\bar{d}) - 2(\Delta s + \Delta\bar{s}), \tag{2.56}$$

where $\left|\frac{g_A}{g_V}\right|$ is the axial charge of the nucleon [44] and the value can be obtained from neutron β decay:

$$a_3 = \left|\frac{g_A}{g_V}\right| = 1.2670 \pm 0.0030. \tag{2.57}$$

The matrix element a_8 is obtained from hyperon β decay [45]:

$$a_8 = 0.585 \pm 0.025. \tag{2.58}$$

2.5.1 Gottfried Sum Rule

The Gottfried sum rule is the difference of first moments of the unpolarized structure functions for proton and neutron:

$$\begin{aligned} S_G &= S^1_{1p} - S^1_{1n} \\ &= \int_0^1 dx\ (F_{1p}(x) - F_{1n}(x)) \\ &= \frac{1}{3} + \frac{2}{3}\int_0^1 dx(\bar{u}(x) - \bar{d}(x)). \end{aligned} \tag{2.59}$$

The NMC collaboration performed the measurement [46] of S_G and reported a valued of

$$S_G = 0.235 \pm 0.026. \tag{2.60}$$

This result indicates a flavor asymmetry of the light sea quark densities $(\bar{u}(x) - \bar{d}(x))$.

2.5.2 Bjørken Sum Rule

Under the assumption of SU(2) isospin symmetry, the first moments of the polarized structure functions for proton and neutron are given by

$$\begin{aligned} \Gamma_{1p} &= \frac{1}{2}\cdot\frac{1}{9}\left(4\Delta u + \Delta d + \Delta s + 4\Delta\bar{u} + \Delta\bar{d} + \Delta\bar{s}\right) \\ &= \frac{1}{9}a_0\Delta\mathcal{C}_S(Q^2) + \left(\frac{1}{12}a_3 + \frac{1}{36}a_8\right)\Delta\mathcal{C}_{NS}(Q^2), \end{aligned} \tag{2.61}$$

$$\begin{aligned} \Gamma_{1n} &= \frac{1}{2}\cdot\frac{1}{9}\left(\Delta u + 4\Delta d + \Delta s + \Delta\bar{u} + 4\Delta\bar{d} + \Delta\bar{s}\right) \\ &= \frac{1}{9}a_0\Delta\mathcal{C}_S(Q^2) - \left(\frac{1}{12}a_3 - \frac{1}{36}a_8\right)\Delta\mathcal{C}_{NS}(Q^2). \end{aligned} \tag{2.62}$$

where $\Delta(C)_{S(NS)}$ is the polarized singlet (non-singlet) coefficient function for the QCD correction. They are given by [47]

$$\begin{aligned} \Delta\mathcal{C}_S(Q^2) &= 1 - \frac{\alpha_s(Q^2)}{\pi} - 1.0959\left(\frac{\alpha_s(Q^2)}{\pi}\right)^2, && (2.63) \\ \Delta\mathcal{C}_{NS}(Q^2) &= 1 - \frac{\alpha_s(Q^2)}{\pi} - 3.7833\left(\frac{\alpha_s(Q^2)}{\pi}\right)^2 - 20.215\left(\frac{\alpha_s(Q^2)}{\pi}\right)^3, && (2.64) \end{aligned}$$

where α_s is the coupling constant of the strong interaction.

The Bjørken sum rule [48] is the difference of the first moments $\Gamma_{1p} - \Gamma_{1n}$:

$$\Gamma_1^{Bj} \equiv \Gamma_{1p} - \Gamma_{1n} = \frac{1}{6}\left|\frac{g_A}{g_V}\right|\mathcal{C}_{NS}(Q^2). \qquad (2.65)$$

An experimental result [32] from E155 collaboration and theoretical prediction were

$$\begin{aligned} \Gamma_1^{Bj} &= 0.176 \pm 0.003(\mathrm{stat}) \pm 0.007(\mathrm{syst}), \quad (\mathrm{experiment}) \\ \Gamma_1^{Bj} &= 0.182 \pm 0.005, \quad (\mathrm{theory}) \end{aligned} \qquad (2.66)$$

where the both are evaluated at $Q^2 = 5\ \mathrm{GeV}^2$. They are in agreement within the statistical and systematic uncertainties. It implies that SU(2) isospin symmetry is not breaking.

2.5.3 The Ellis-Jaffe Sum Rule

Under the assumption that the polarized densities of the strange and anti-strange quarks and the gluons are unpolarized inside nucleon, $\Delta s + \Delta\bar{s} = \Delta g = 0$, and SU(3) symmetry is true, the first moments of the polarized structure functions are given by

$$\Gamma_{1p} = \frac{a_8}{9}\Delta\mathcal{C}_S(Q^2) + \frac{1}{12}\left(a_3 + \frac{a_8}{3}\right)\Delta\mathcal{C}_{NS}(Q^2), \qquad (2.67)$$

$$\Gamma_{1n} = \frac{a_8}{9}\Delta\mathcal{C}_S(Q^2) - \frac{1}{12}\left(a_3 - \frac{a_8}{3}\right)\Delta\mathcal{C}_{NS}(Q^2). \qquad (2.68)$$

Theoretical prediction is

$$\begin{aligned} \Gamma_{1p}(Q^2 = 5\mathrm{GeV}^2) &= 0.170 \pm 0.005, \quad (\mathrm{theory}) \\ \Gamma_{1n}(Q^2 = 5\mathrm{GeV}^2) &= -0.014 \pm 0.005. \quad (\mathrm{theory}) \end{aligned}$$

If experimental results are not in agreement with the prediction, the contributions from the strange quarks or gluons to the nucleon spin cannot be treated as unpolarized, or SU(3) symmetry is broken. The experimental result will be shown in next section.

2.6 The Nucleon Spin Problem

First Measurements of the spin structure of the nucleon was performed by SLAC E80 [4, 5] and E130 [6]. They measured the double spin asymmetry for the deep inelastic scattering of longitudinally polarized electrons off longitudinally polarized protons. Then the integral of $g_{1p}(x)$ over x in the measured region of $0.1 < x < 0.64$ was calculated as

$$\int_{0.1}^{0.64} dx\; g_{1p}(x) = \int_{0.1}^{0.64} dx\; \frac{1}{2x}\frac{A_{1p}}{F_{2p}}(1+R) = 0.095 \pm 0.008. \qquad (2.69)$$

The contribution from higher x region to the integral is probably small, while the contribution from lower x region is more complicated. The integral of the polarized structure function over the full x range either is consistent with the Ellis-Jaffe sum rule for the proton or not. The result was inconclusive.

The European Muon Collaboration (EMC) carried out precision measurements of the asymmetry in x region of $0.01 < x < 0.7$ [7, 8]. Their experiment is analogous to the experiment by SLAC except for the using polarized high energy muon beam. The integral of g_1 in the measured region was

$$\int_{0.01}^{0.7} dx\; g_{1p}(x) = 0.120 \pm 0.013. \qquad (2.70)$$

The integral which include the contributions outside the measured region was estimated from the parameterization of the asymmetry. The result was

$$\int_{0}^{1.0} dx\; g_{1p}(x) = 0.123 \pm 0.013(\mathrm{stat.}) \pm 0.019(\mathrm{syst.}), \qquad (2.71)$$

which is inconsistent with the Ellis-Jaffe prediction. This was called “spin crisis”. Later the spin structure of the nucleon was investigated by various experiments and the contribution of all the quark spins in the nucleon was reported to be 20% - 30%.

2.6.1 Overview of the investigation of quark helicity distributions

Now we review the investigation of the spin structure of the nucleon.

In 1997, the Spin Muon Collaboration (SMC) measured the quark polarization of u and d valence quark $(\Delta u_v, \Delta d_v)$, and the non-strange sea polarization $\Delta\bar{q}(x)$ [49]. The measurement was performed using DIS of longitudinally polarized muons off longitudinally polarized nucleons. The inclusive and semi-inclusive double spin asymmetries for positive and negative hadron productions were extracted. No hadron identification was made. The asymmetries were used to determine $(\Delta u_v, \Delta d_v, \Delta\bar{q})$ under the assumption that SU(3) symmetric sea $(\Delta\bar{q}(x) \equiv \Delta\bar{u}(x) = \Delta\bar{d}(x) = \Delta s(x) = \Delta\bar{s}(x))$.

In 1999, HERMES reported the first result of the polarized quark distributions [50]. The detail of the HERMES experiment will be described in the next chapter. The polarized quark distributions of $u+\bar{u}$, $d+\bar{d}$ and $s+\bar{s}$ were extracted under the assumption that the contribution of sea quarks is independent of flavor ($\frac{\Delta u_{sea}}{u_{sea}} = \frac{\Delta d_{sea}}{d_{sea}} = \frac{\Delta s}{s} = \frac{\Delta\bar{d}}{\bar{d}} = \frac{\Delta\bar{s}}{\bar{s}}$). The h^+, h^- and inclusive asymmetries were used.

From the spin asymmetry A_1 in inclusive measurement, the polarized structure function g_1 can be obtained by

$$g_1(x, Q^2) = A_1(x, Q^2)\frac{F_2(x, Q^2)}{2x(1 + R(x, Q^2))}. \tag{2.72}$$

The unpolarized structure function F_2 are well-known for the measurements by various experiments. Therefore the polarized PDFs can be extracted to analyze g_1. Here three different phenomenological fits to the inclusive data are introduced. The polarized PDFs of $\Delta u_v = \Delta u - \Delta\bar{u}, \Delta d_v = \Delta d - \Delta\bar{d}, \Delta\bar{q}$ and Δg were determined for each fit.

A functional form of the polarized PDFs assumed by the GRSV group [51] is

$$\Delta f(x) = ax^b(1-x)^c f(x), \tag{2.73}$$

where a, b and c are free parameters, and $f(x)$ is the unpolarized PDF. $(\Delta\bar{q} \equiv \Delta\bar{u} = \Delta\bar{d} = \Delta u_{sea} = \Delta d_{sea})$ and $(\Delta s = \Delta\bar{s} = 0)$ are assumed in SU(3) broken "valence" scenario.

Another functional form of the polarized PDFs assumed by the Blümlein and Böttcher [52] is

$$\Delta f(x) = \left(\int_0^1 dx \Delta f(x)\right) A(a, b, c, d)x^a(1-x)^b(1 + cx + dx^{\frac{1}{2}}), \tag{2.74}$$

where a, b, c and d are free parameters and $A(a, b, c, d)$ is normalization constants which depends only on the free parameters. SU(3) symmetric sea distributions ($\Delta\bar{q} \equiv (\Delta\bar{u} = \Delta\bar{d} = \Delta s = \Delta\bar{s})$) are assumed.

The last one assumed by the Asymmetry Analysis Collaboration (AAC) [45, 53] is

$$\Delta f(x) = \Big(ax^b - c(x^b - x^d)\Big)\, f(x), \tag{2.75}$$

where a, b, c and d are free parameters. SU(3) symmetric sea distributions $(\Delta\bar{q} \equiv \Delta\bar{u} = \Delta\bar{d} = \Delta s = \Delta\bar{s})$ are assumed.

There are some problems of these phenomenological fits:

- An functional form needs to be assumed.
- A number of fit parameters is limited.
- An assumption is needed for sea quarks.
- An assumption is needed in unmeasured region.

To solve these problems, it is important to identify hadrons in coincidence with the scattered lepton. The HERMES experiment has performed such a semi-inclusive measurement after installing the RICH detector in 1998. HERMES measured the π^+, π^-, K^+ and K^- asymmetries for the first time. It enable us to determine the separate contributions of the quark flavors to the nucleon spin ($\Delta u, \Delta d, \Delta s, \Delta\bar{u}, \Delta\bar{d}, \Delta\bar{s}$). It should be emphasized that the flavor decomposition was done x bin by bin, thanks to the asymmetries data from semi-inclusive hadron measurement. Also it should be stressed that no functional forms need to be assumed in unmeasured region. The results is briefly summarized in [54]. The detail of the analysis [55] was published in Physical Review D.

2.6.2 u and d quarks contribution to the proton spin in Constituent Quark Model

The proton is one of the ground-state baryons with spin $\frac{1}{2}$ which is constructed from uud quarks in QPM. The wave function of a spin-up proton can be given by

$$|p\uparrow\rangle = \sqrt{\frac{1}{18}}\,(\mathrm{uud}(\uparrow\downarrow\uparrow + \downarrow\uparrow\uparrow - 2\uparrow\uparrow\downarrow) + \mathrm{udu}(\uparrow\uparrow\downarrow + \downarrow\uparrow\uparrow - 2\uparrow\downarrow\uparrow) + \mathrm{duu}(\uparrow\downarrow\uparrow + \uparrow\uparrow\downarrow - 2\downarrow\uparrow\uparrow)). \tag{2.76}$$

The magnetic moment of the proton μ_p in this model can be given by

$$\begin{aligned}\mu_p &= \sum_{i=1}^{3} \langle p\uparrow | Q_i \left(\frac{e}{2m_i}\right) | p\uparrow\rangle \\ &= \frac{2}{3}(2\mu_u - \mu_d) + \frac{1}{3}\mu_d = \frac{4}{3}\mu_u - \frac{1}{3}\mu_d, \qquad (2.77)\end{aligned}$$

where $Q_i e$ and m_i represent the charge and mass of i-th quark and μ_u and μ_d are the magnetic moment of the u and d quarks. The magnetic moment of the neutron μ_n can be obtained by interchanging the u and d quarks:

$$\mu_n = \frac{2}{3}(2\mu_d - \mu_u) + \frac{1}{3}\mu_u = \frac{4}{3}\mu_d - \frac{1}{3}\mu_u, \qquad (2.78)$$

Then the ratio of two quantities is written as

$$\begin{aligned}\frac{\mu_n}{\mu_p} &= \frac{\frac{4}{3}\mu_d - \frac{1}{3}\mu_u}{\frac{4}{3}\mu_u - \frac{1}{3}\mu_d} \qquad (2.79) \\ &= \frac{\frac{4}{3}\left(-\frac{1}{3}\right) - \frac{1}{3}\left(\frac{2}{3}\right)}{\frac{4}{3}\left(\frac{2}{3}\right) - \frac{1}{3}\left(-\frac{1}{3}\right)} \qquad (2.80) \\ &= -\frac{2}{3}, \qquad (2.81)\end{aligned}$$

where $m_u = m_d$ is assumed. It is in good agreement with the experimental value:

$$\left(\frac{\mu_n}{\mu_p}\right)_{\mathrm{exp}} \simeq -0.685. \qquad (2.82)$$

The spin contribution of u and d quarks to the proton spin can be evaluated in this model:

$$\begin{array}{rcccl} \langle p\uparrow | S(\mathrm{u}) | p\uparrow\rangle &=& \langle p\uparrow | \frac{1}{2}\sigma(\mathrm{u}) | p\uparrow\rangle &=& \frac{2}{3}, \\ \langle p\uparrow | S(\mathrm{d}) | p\uparrow\rangle &=& \langle p\uparrow | \frac{1}{2}\sigma(\mathrm{d}) | p\uparrow\rangle &=& -\frac{1}{6}, \\ \langle p\uparrow | S(\mathrm{u}) + S(\mathrm{d}) | p\uparrow\rangle &=& \langle p\uparrow | \frac{1}{2}(\sigma(\mathrm{u}) + \sigma(\mathrm{d})) | p\uparrow\rangle &=& \frac{1}{2}, \end{array} \qquad (2.83)$$

where S is the spin operator and σ represents Pauli matrix. It indicates that the u quark spin is aligned to the proton spin, while the d quark spin is anti-aligned to the proton spin.

2.6.3 Other Processes to Solve Spin Crisis

A few other process which could contribute to solve the nucleon spin problem are described here.

Drell-Yan Process

The diagram of the Drell-Yan process is shown in Figure 2.8. In proton-proton collisions, a quark and an anti-quark in the nucleon annihilate into a photon which will decay into a lepton pair. This mechanism is called Drell-Yan process. The double spin asymmetry for the longitudinally polarized proton-proton collision is given by

$$A_{LL}^{DY}(x_1, x_2) = \frac{\sum_f e_f^2 \Delta q_f(x_1)\Delta\bar{q}_f(x_2) + \sum_f e_f^2 \Delta q_f(x_2)\Delta\bar{q}_f(x_1))}{\sum_f e_f^2 q_f(x_1)\bar{q}_f(x_2) + \sum_f e_f^2 q_f(x_2)\bar{q}_f(x_1))}. \qquad (2.84)$$

This asymmetry provides information of the quark helicity distributions of quarks and anti-quarks.

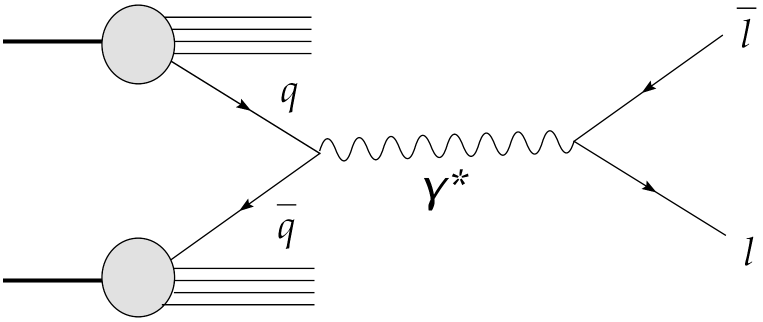

Figure 2.8: Diagram of Drell-Yan process.

Vector Boson Production

Measurements of the asymmetry for W production allow to determine the helicity distributions of anti-quarks since W bosons can be produced via the reactions $u\bar{d} \to W^+$ and $d\bar{u} \to W^-$. Diagrams for W$^{+(-)}$ production is shown in Figure 2.9. The single spin asymmetry for W productions is given by

$$A_{LU}^{pp\to W^+X} = \frac{\Delta u(x_1)\bar{d}(x_2) - \Delta\bar{d}(x_1)u(x_2)}{u(x_1)\bar{d}(x_2) + \bar{d}(x_1)u(x_2)}, \qquad (2.85)$$

$$A_{LU}^{pp\to W^- X} \;=\; \frac{\Delta d(x_1)\bar{u}(x_2) - \Delta\bar{u}(x_1)d(x_2)}{d(x_1)\bar{u}(x_2) + \bar{u}(x_1)d(x_2)}. \qquad (2.86)$$

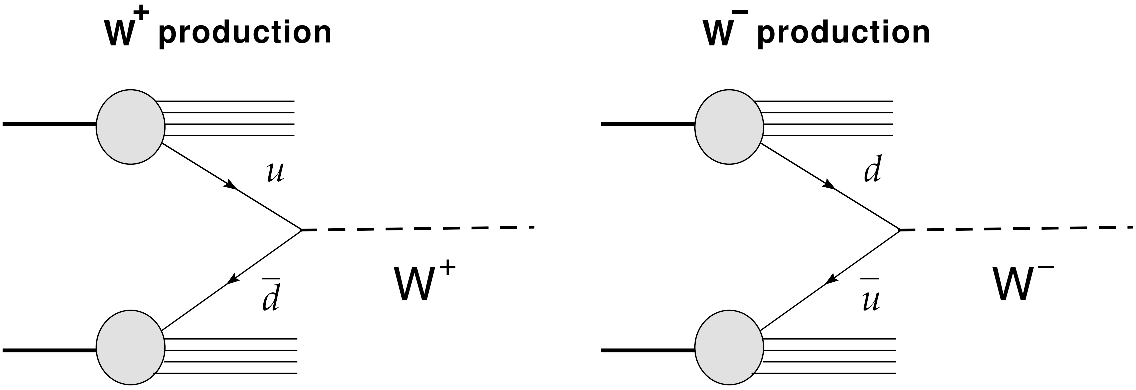

Figure 2.9: Diagram of W boson production.

high p_T prompt photon production

The gluon helicity distribution can be accessed via the asymmetry measurement of prompt photon production with high transverse momentum. In polarized proton-proton collisions, the gluon compton process dominates the production by a factor of 9 with respect to quark anti-quark annihilation process. Figure 2.10 shows these two diagrams of high p_T prompt photon production. The double spin asymmetry for prompt photon production with high transverse momentum is expressed as

$$A_{LL}^{pp\to\gamma X}(p_T) \approx \frac{\Delta G(x_T)}{G(x_T)}\frac{\Delta q(x_T)}{q(x_T)} a_{LL}(qg \to \gamma q), \qquad (2.87)$$

where $x_T = 2\frac{p_T}{\sqrt{s}}$ and σ_{LL} represents the partonic asymmetry for gluon Compton process. The gluon helicity distribution can be obtained by using the known quark helicity distributions.

Heavy quark production

The heavy quark production allows to probe the gluon helicity distribution. In polarized proton-proton collisions, the open charm and bottom are produced via

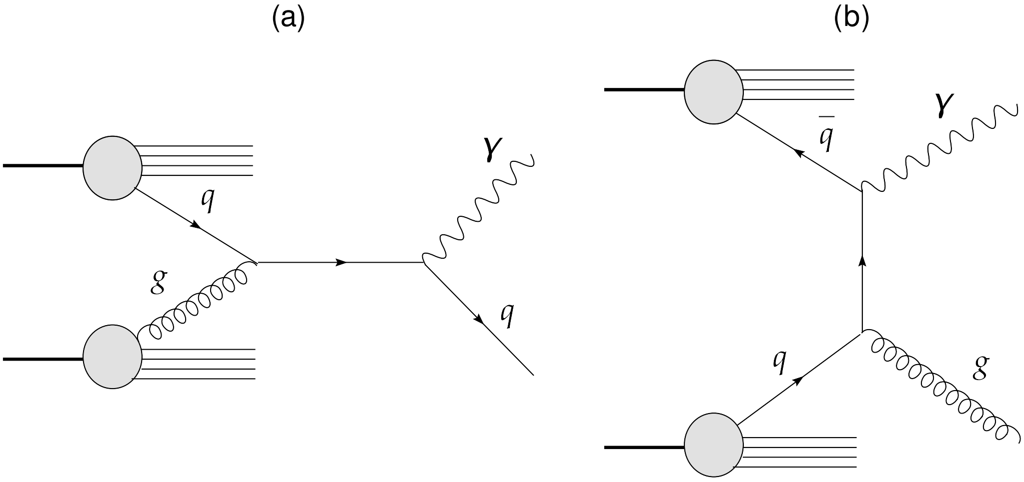

Figure 2.10: Diagram of high p_T prompt photon production. (a) gluon compton scattering (b) quark anti-quark annihilation

gluon fusion. Figure 2.11 shows the diagram of heavy quark production. The double spin asymmetry for heavy quark production is given by

$$A_{LL}^{pp\to QQX} = \frac{\Delta G}{G}\frac{\Delta G}{G}\sigma_{LL}(gg \to Q\bar{Q}). \tag{2.88}$$

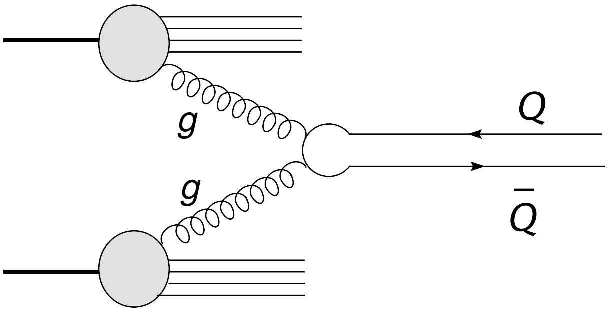

Figure 2.11: Diagram of heavy quark production.

Chapter 3

The HERMES Experiment

HERMES (HERa MEasurement of Spin) is an experiment to investigate the spin structure of the nucleon by using Deep In-elastic positron-nucleon Scattering (DIS) at DESY (Deutshes Elektronen-SYnchrotron) in Hamburg, Germany. HERMES is located in the HERA East Hall and there are two other operating experiments H1 and ZEUS. Both of them are experiments of positron-proton collision located in the HERA North Hall (H1) and in the South Hall (ZEUS). Figure 3.1 shows the schematic view of the experiments at DESY. In this chapter, the HERMES experiment is described.

3.1 The Polarized Positron Beam

The HERMES experiment uses the positron beam with the energy of 27.6 GeV in a synchrotron HERA (Hadron Electron Ring Accelerator). The HERA storage ring has a circumference of 6.3 km. One of the advantages of using the circulating beam is that the beam is transversely self-polarized by Sokolov-Ternov effect [56]. The beam polarization is defined as

$$P = \frac{N^{\uparrow} - N^{\downarrow}}{N^{\uparrow} + N^{\downarrow}}, \tag{3.1}$$

where $N^{\uparrow}$ and $N^{\downarrow}$ represent the number of positrons with aligned spins with respect to the magnetic dipole field and aligned spins in the opposite direction, respectively. The polarization is zero initially after injection and increases with time

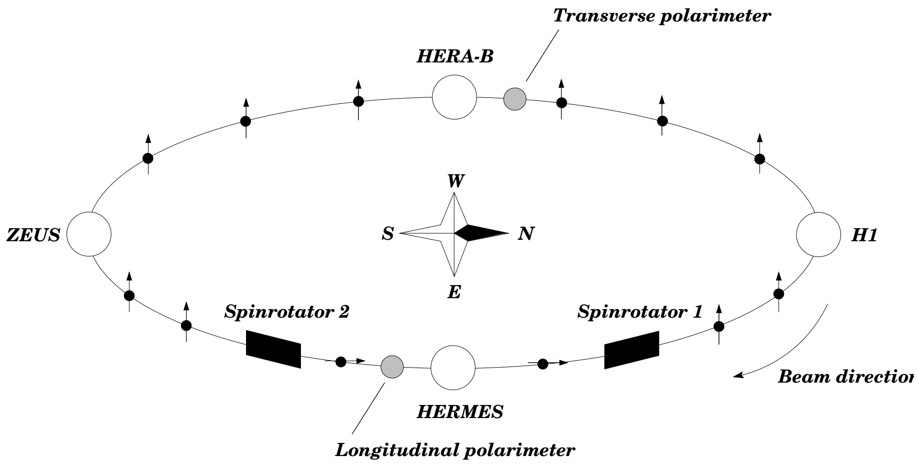

Figure 3.1: Schematic view of the experiments at DESY.

according to

$$P(t) = P_{max} \cdot (1 - e^{-t/\tau}), \tag{3.2}$$

$$P_{max} = \frac{8}{5\sqrt{3}}, \tag{3.3}$$

where P_{max} is maximum polarization value in an ideal case, τ is a variable which accounts for the ring radius and the energy of the beam. Figure 3.2 shows time dependence of the beam polarization. As can be seen, the polarization rises up to 60 % in an hour.

As mentioned above, the beam is transversely polarized. For the study of the polarized quark distributions (Δq), longitudinally polarized beam is required. To achieve this, spin rotators are installed in front of and behind the HERMES detectors. A schematic view of the positron track inside the spin rotator is shown in Figure 3.3. The most upper and middle panels represent the orbit of the beam from top view and side view respectively. The measurements of the beam polarization are performed by the Longitudinal Polarimeter which will be described in the next subsection. The parameters of the beam are summarized in Table 3.1 together with the target informations.

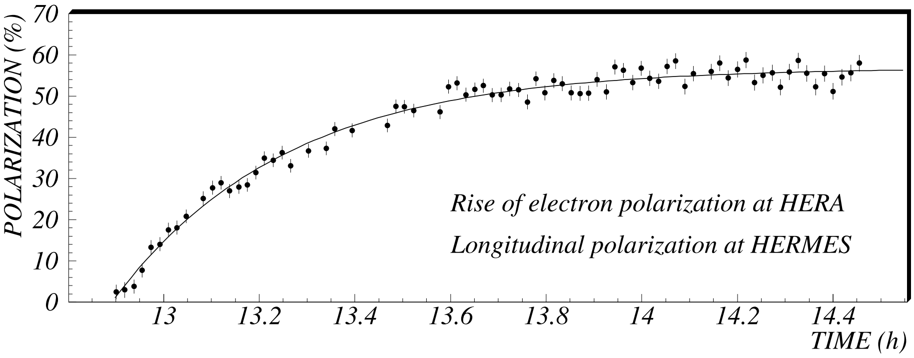

Figure 3.2: Rise time curve of the beam polarization at HERA.

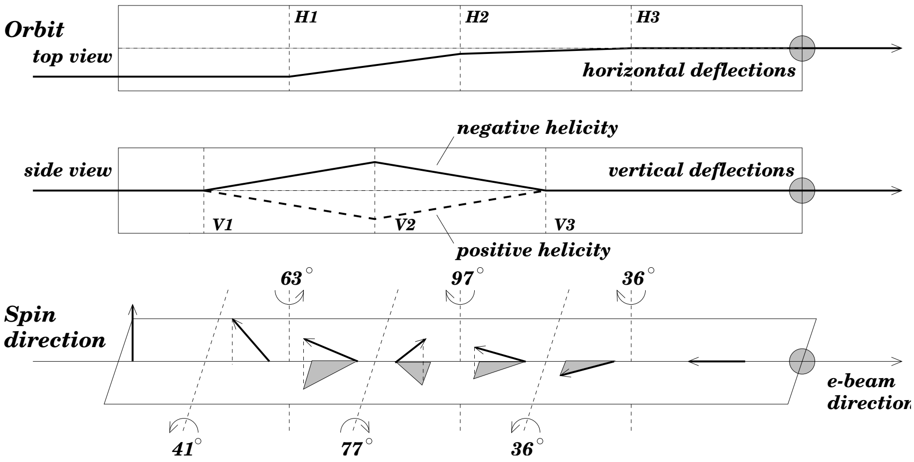

Figure 3.3: Schematic view of the positron track

3.1.1 Longitudinal Polarimeter

Longitudinal Polarimeter (LPOL) is installed 50 m behind the HERMES detectors. The polarimeter is used to measure the beam spin by Compton backscattering [57]. A Schematic view of the LPOL is shown in Figure 3.4. A pulsed Nd:YAG laser produces photons with energy of $E = 2.33$ eV. The laser is synchronized with the positron bunches in the HERA ring. The angle between the positron beam and laser beam is as small as possible to maximize the Compton scattering rate. A LPOL calorimeter was designed for the measurement of the energy of the back scattered Compton photons for each laser pulse to determine the beam polarization.

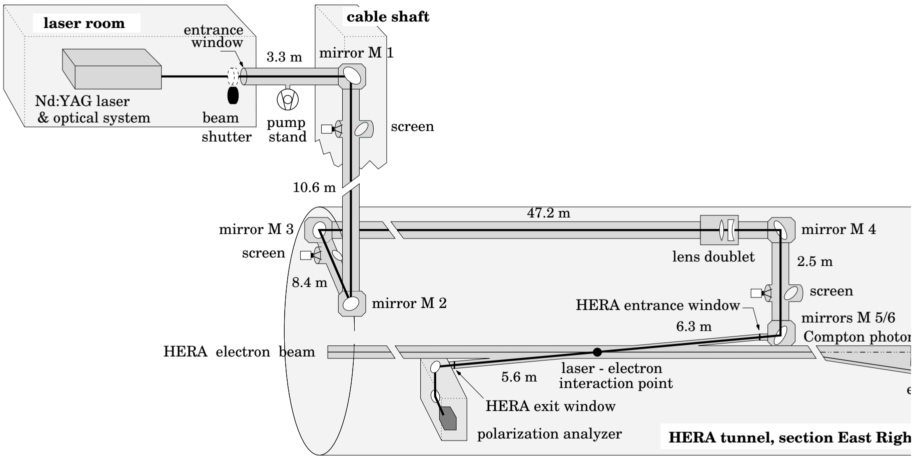

Figure 3.4: Layout of the Longitudinal Polarimeter at HERA.

3.2 Polarized Gas Targets

The HERMES experiment uses polarized gas targets inside the positron beam pipe. To increase the target density, the gas is stored in a “storage cell” which is an open-ended elliptical tube with the longer radius of 29 mm and the other radius of 9.8 mm. Figure 3.5 shows the schematic view of the components of the gas target. To produce and analyze the polarized target, an Atomic Beam Source, Breit Rabi Polarimeter and Target Gas Analyzer are used. The schematic layout of the components are shown in Figure 3.6.

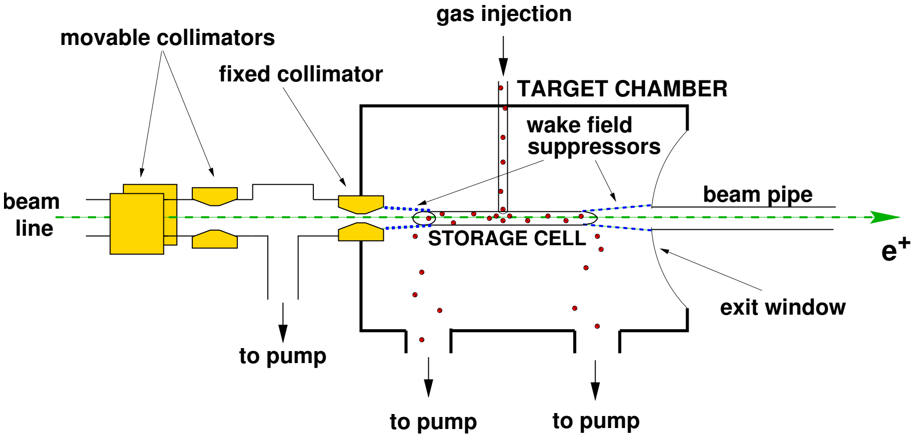

Figure 3.5: The internal gas target.

Atomic Beam Source

The Atomic Beam Source (ABS) [58] provides the longitudinally polarized target based on the principle of Stern-Gerlach separation. The polarized target is achieved as follows:

- Molecular hydrogen is injected into the dissociator and dissociated by an RF discharge.
- A sextupole magnet system focuses the atoms of the same spin state of the electron with respect to the beam axis of ABS.
- The electron spin is transfered to the nuclear spin by Weak Field Transition (WFS) and Strong Field Transition (SFT) with high radio frequency wave.

The orientation of the target spin is reversed every 60 seconds to minimize systematic uncertainty on the asymmetry measurement.

Target Gas Analyzer and Breit Rabi Polarimeter

The target polarization depends on the polarization of the atoms and molecules in the target cell and the degree of dissociation. The measurements of them are performed by the Breit Rabi Polarimeter (BRP) and Target Gas Analyzer (TGA). A small fraction of the target atoms in the storage cell is extracted and analyzed in BRP. Similarly to ABS, BRP consists of a sextupole magnet and RF transitions.

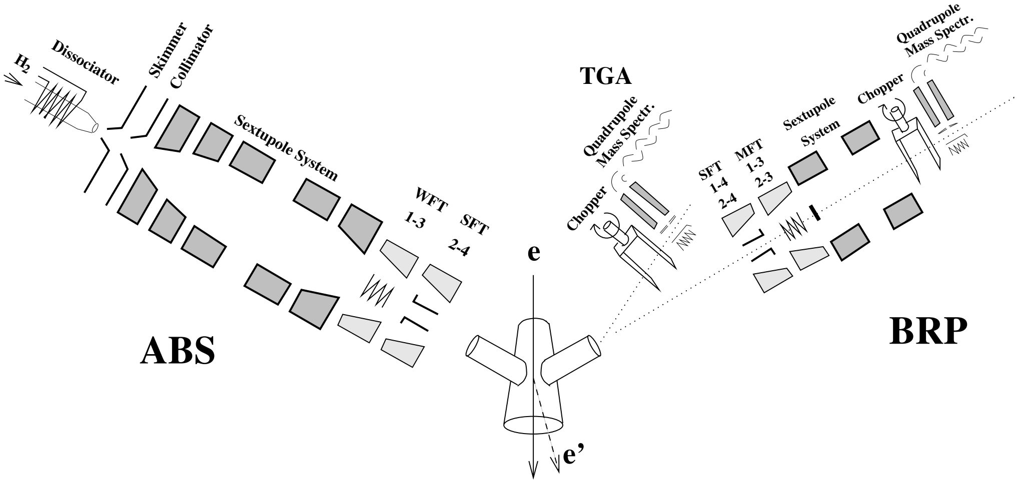

Figure 3.6: The schematic layout of the ABS, BRP and TGA.

The polarization of the target atoms can be calculated from the measurements of the relative occupation numbers of the hyperfine states of the target atoms. The degree of dissociation of the atoms can be evaluated by TGA which is located at an angle of 7 degrees with respect to the axis of the sampling tube. To determine the target polarization precisely, TGA plays an important role to get rid of background from the molecules. From these informations, the target polarization P^T is given by

$$P^T = \alpha_0 \alpha_r P^a + \alpha_0 (1 - \alpha_r) P^m, \tag{3.4}$$

where P^a and P^m are the polarization of the atoms and molecules respectively, α_r and $(1 - \alpha_r)$ represent the fraction of atoms and molecules in the target.

In the year 1996 and 1997 the HERMES experiment was operated with a polarized hydrogen target, while a polarized deuteron target was used from 1998 to 2000. The parameters of the targets are listed in Table 3.1.

3.3 HERMES Spectrometer

The HERMES experiment uses a forward spectrometer which consists of two identical halves below and above the beam line [59]. Figure 3.7 shows a schematic view of the HERMES spectrometer.

	Beam		
Year	Type	Polarization	Fractional Uncertaintiy
1996	e^+	52.8 %	3.4 %
1997	e^+	53.1 %	3.4 %
1998	e^-	52.1 %	3.4 %
1999	e^+	53.3 %	1.8 %
2000	e^+	53.3 %	1.9 %
	Target		
Year	Type	Polarization	Fractional Uncertainty
1996	Hydrogen	74.8 %	5.5 %
1997	Hydrogen	85.0 %	3.8 %
1998	Deuterium	81.7 %	7.5 %
1999	Deuterium	81.0 %	7.0 %
2000	Deuterium	84.5 %	3.5 %

Table 3.1: Parameters of the Polarized hydrogen and deuteron target.

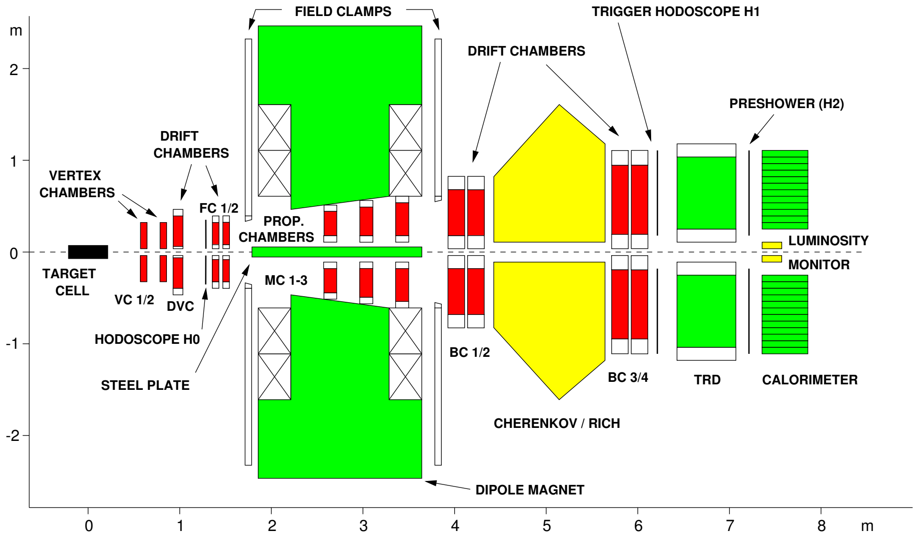

Figure 3.7: The schematic view of the HERMES spectrometer.

The geometrical acceptance of the spectrometer is ± 170 mrad in the horizontal direction and from ± 40 mrad to ± 140 rad in the vertical direction with respect to the beam axis. This constrain is due to steel plates for shielding the positron beam from the field of the spectrometer magnet. The HERMES spectrometer consists of several detectors: a calorimeter, hodoscopes, a transition radiation detector for positron-hadron separation and a RICH detector for hadron identification. Tracking chambers for measurements of the trajectories of charged particles as well as the particle momentum in combination with the magnet, and a luminosity monitor for measurements of the luminosity.

3.3.1 Tracking System

The tracking system consists of 5 tracking chambers (VC1/2, DVC, FC1/2) upstream of, 3 chambers (MC1-3) inside and 4 chambers (BC1-4) downstream of the magnet. The Vertex Chambers (VCs) [60] are silicon gas micro-strip chambers and the Front Chambers (FCs) [61] are drift chambers. Drift Vertex Chambers (DVCs) provide 544 channels per detector half and provide a resolution of 200 μm per plane. These chambers are used to determine the event vertex and the scattering angle with respect to the positron beam. The Magnet Chambers (MCs) [62] are proportional chambers so that they can be operated in the magnetic field. The MCs allows to simplify the matching of the multiple tracks in the forward and rear part of the detector. The Back chambers (BCs) consist of two groups (BC1/2, BC3/4) and they are drift chambers (Figure 3.8). The former ones have the active area of 1880 $\times$ 520 mm^2 while the latter ones 2890 $\times$ 710 mm^2. The drift cell size is 15 mm and provides a resolution of 275 μm and 300 μm per plane for BC1/2 and BC 3/4 respectively. The BCs are used to reconstruct the particle tracks bent by the magnet.

3.3.2 Spectrometer Magnet

The HERMES magnet is a dipole magnet with a field integral of $\int Bdl = 1.3$ Tm. As mentioned, the magnet gap above and below the steel plate allows for the acceptance of 40 mrad $< |\theta_y| <$ 140 mrad and $|\theta_x| <$ 170 mrad. To shield the chambers in front of/behind the magnet from the strong magnet filed, field clumps are installed at upstream/downstream of the magnet.

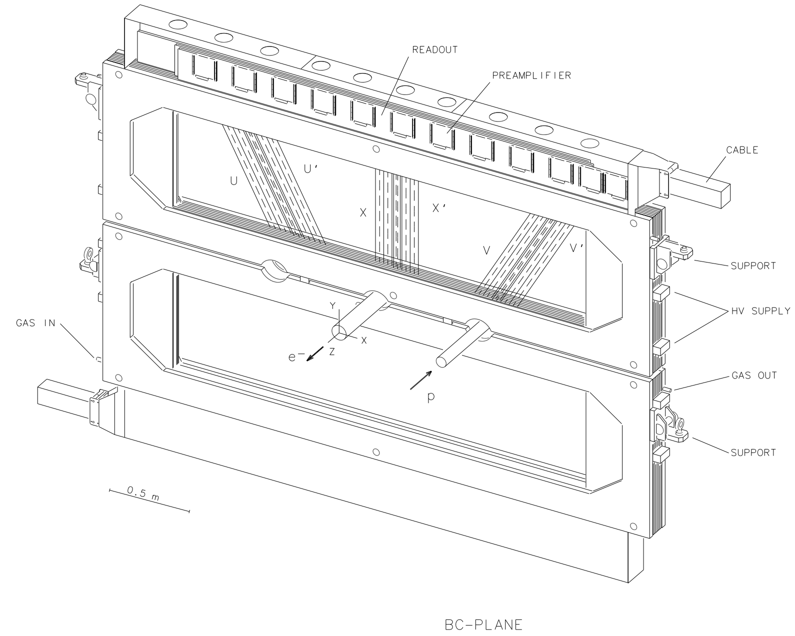

Figure 3.8: Schematic view of the BC chambers.

3.3.3 Particle Identification Detectors

Calorimeter

The electromagnetic calorimeter [63] is used for the identification of leptons for the DIS events. Furthermore the detector is used as first level trigger. Leptons lose all of the energy in the detector, while Hadrons lose only a fraction of the energy. The detector consists of 420 radiation hard F101 lead glass blocks for each half of the detector. The size of a block is $9 \times 9 \times 50\mathrm{cm}^3$. As shown in Figure 3.9, the blocks are arranged in a 42×10 array. To protect the detector from synchrotron radiation, up and bottom calorimeters are moved 50 cm out vertically from the beam pipe during the beam injection and moved in during data taking. The energy resolution of the detector is given by

$$\frac{\sigma(E)}{E} = 1.5 \pm 0.5 + \frac{5.1 \pm 1.1}{\sqrt{E}}, \tag{3.5}$$

where E is the energy of the track in GeV [64].

Hodoscopes

Three hodoscopes H0, H1 and H2 are used for triggering and separation of positrons and hadrons. H0 is installed in front of FC1. It is comprised of a single sheet of 3.2 mm thick plastic scintillator corresponding to 0.7 % radiation length. Backward particles are suppressed from time-of-flight informations. H1 and H2 are located in front of and behind TRD, respectively. Both hodoscopes consist of 42 plastic scintillator paddles with a size of 9.3 $\times$ 91 $\times$ 1 cm^3. H1 serves as first level trigger. H2 performs as a pre-shower detector and allows pion-positron separation. This is based on the difference of the energy deposit for pions (about 2MeV) and positrons (about 20-40 MeV) .

Transition Radiation Detector

The Transition Radiation Detector (TRD) separates leptons from hadrons. The TRD is installed between H1 and H2. It is constructed from 6 modules which have a radiator followed by an X-ray detector and a multi-wire proportional chamber. The radiator consists of a packed 6.5 cm thick matrix of randomly oriented propylene fibers with a diameter of 17 - 20 μm. The chamber contains 90 % Xe and 10 % CH_4 for efficient X-ray absorption. Clusters of electrons in the gas are produced by X-ray absorption and large signals are a sign from the relativistic

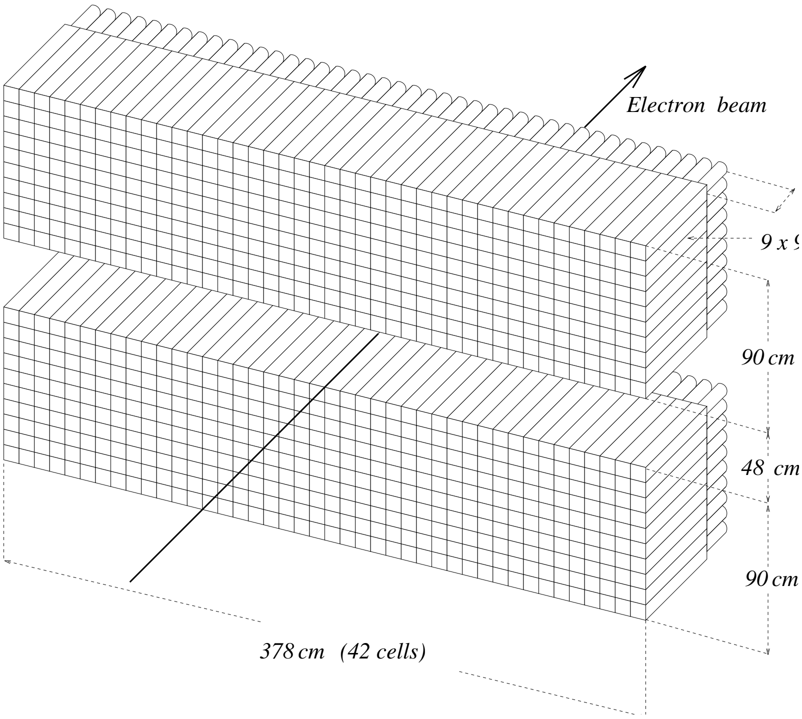

Figure 3.9: Schematic view of the calorimeter

positrons. By the combination of 6 modules, the TRD accomplishes the positron-pion separation with a factor 100:1 at 5 GeV.

Threshold Čerenkov Detector

In the year 1996 and 1997, the threshold Čerenkov detector has been used to identify pions. A particle with velocity v larger than the phase velocity of light in the radiators emits Čerenkov photons at a characteristic angle θ related to the particle velocity as

$$\cos\theta = \frac{1}{\beta n}, \tag{3.6}$$

where $\beta = \frac{v}{c}$, c is the speed of light in vacuum and n is the refractive index of the material. A gas mixture of 70 % $\mathrm{N_2}$ and 30 % $\mathrm{C_4F_{10}}$ was used as a radiator. The refractive index of the radiator is $n = 1.000066$. The threshold momenta for pions, kaons and protons are 3.94, 13.6 and 25.8 GeV/c, respectively. The particle momentum is determined from an orbit of the particle bent by the spectrometer magnet. If particles with momentum of 3.94 $< p <$ 13.6 GeV/c emit the Čerenkov photons in the radiator, the particles are determined to be pions.

Ring Imaging Čerenkov Detector

From 1998 to 2000, the Ring Imaging Čerenkov (RICH) detector has been used. The RICH detector allows to identify not only pions but also kaons and protons by using dual radiators of an aerogel and a $\mathrm{C_4F_{10}}$ gas. The particle type can be determined in the wide momentum range of 2 - 15 GeV/c from the measured Čerenkov angle. The detail will be described in the next chapter.

3.3.4 Luminosity Monitor

The Luminosity monitor performs the measurement of the luminosity L defined as

$$L = \phi \cdot N_t, \tag{3.7}$$

where ϕ represents the flux of the beam and N_t is the number of target within the cross section of the beam. The measurement of the luminosity employs the processes of Bhabha scattering which is elastic scattering $e^+e^- \rightarrow e^+e^-$ and the annihilation of beam positrons with the shell electrons of the target ($e^+e^- \rightarrow \gamma\gamma$). The cross sections of the two processes can be calculated in the framework of QED. The luminosity monitor consists of a pair of electromagnetic calorimeters which are located on either side of the beam pipe (Figure 3.10). The calorimeters detect the symmetrically scattered particles in coincidence. An energy deposition above 4.5 GeV allows to select Bhabha events as well as e^+e^- annihilation events. The energy resolution of the calorimeter is given by

$$\frac{\sigma(E)}{E} = \frac{9.3 \pm 0.1}{\sqrt{E}}. \tag{3.8}$$

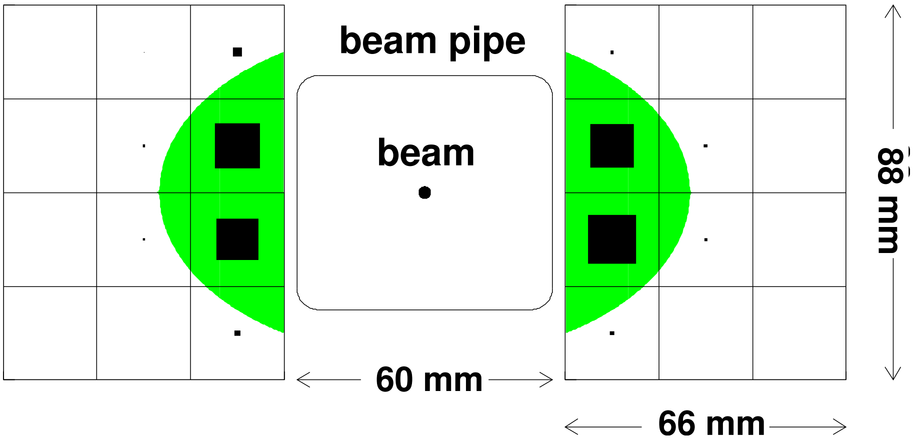

Figure 3.10: Schematic view of the luminosity monitor.

3.3.5 Gain Monitoring System

The Gain Monitoring System (GMS) monitors the stability of the response of the photon multipliers PMTs using a ND:YAG laser with a wavelength of 532 nm [65]. Figure 3.11 shows the photo of the laser. Six different intensities of the laser pulse are generated at a rate of a few Hz. The laser pulse should be sent to the detectors in the absence of a HERMES positron beam pulse in the HERMES detector. For this purpose, the laser trigger is synchronized with the empty bunches of the HERA beam.

To check the stability of the laser itself, PIN photo diodes (S1990, Hamamatu Corp.) are used. Since the gain of the photo diodes are known to be stable, the stability of the detectors are evaluated as the ratio of the detector gains to the photo diode gain. Thus 950 PMTs which are used in the calorimeter, the hodoscopes, the luminosity and the LPOL are monitored with this GMS.

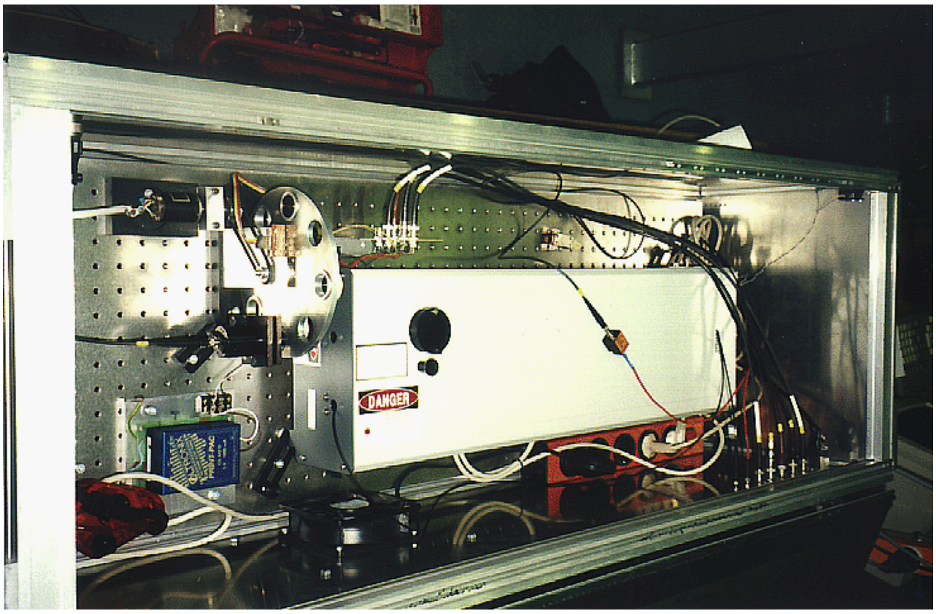

Figure 3.11: Photo of a ND:YAG laser used in the Gain Monitoring System.

Chapter 4

Ring Imaging Čerenkov Detector

4.1 Detector Design

The Ring Imaging Čerenkov (RICH) detector is designed to identify pions, kaons and protons [66]. Two symmetrical RICH modules are installed above and below the positron beam pipe. The schematic view of the upper detector is shown in Figure 4.1. The RICH detector is composed of dual radiators, mirrors and photon detectors. Details of the components are given in Table 4.1.

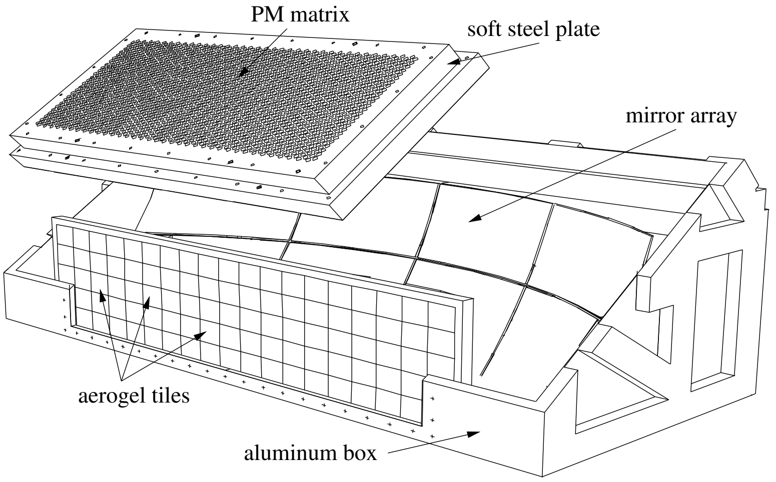

Figure 4.1: Schematic view of the RICH detector.

The most of hadrons produced in DIS events at HERMES are found in the

Components	Characteristics
Housing Box	$2 \times 2 \times 1.3$m^3
Radiators	
C_4F_{10} gas	n=1.00137
aerogel	n=1.0303
	size:11×11cm^2 surface $\times 1.0$cm thickness
	number of tiles:$17 \times 5 \times 5 = 425$
Mirrors	radius:220cm
	size:$\sim 60 \times 40$cm^2
	number of mirrors:8
Photon Detectors	$1934\times$PMTs
	active area:145×60cm^2
PMT	diameter:3/4”
Readout system	LeCroy PCOS4

Table 4.1: The components of the RICH detector.

momentum rage of 2 to 15 GeV/c. Aerogel and C_4F_{10} gas are selected as radiators since aerogel have a large refractive index, on the other hand gases as C_4F_{10} gas have a small refractive index. The combination of the two radiators enables us to separate hadrons clearly in the relevant momentum range.

Charged particles with velocity larger than phase velocity of light in the material emits Čerenkov photons. The Čerenkov angle which is defined as an angle between the particle track and the photon direction is related to particle velocity v

$$\cos\theta = \frac{c/n}{v} = \frac{1}{n\beta}, \tag{4.1}$$

where c is the speed of light and n the refractive index of the material. The particle mass is therefore given by

$$\begin{aligned} m &= \frac{p}{c\beta\gamma}, \\ &= \frac{pn\cos\theta}{c\gamma}, \end{aligned} \tag{4.2}$$

if the momentum is known from the spectrometer magnet. Figure 4.2 shows Čerenkov angle versus hadron momentum for each radiator. No particles with velocity smaller than phase velocity of light can emit Čerenkov photons. The velocity of the particle for emission of Čerenkov photons is required to be $\beta > 0.9705$ for the aerogel and $\beta > 0.9986$ for $\mathrm{C_4F_{10}}$ gas.

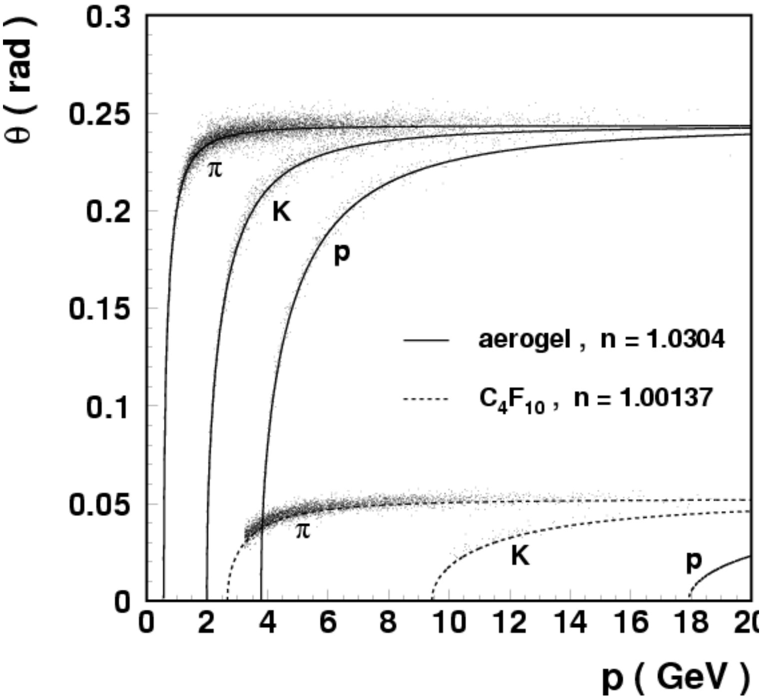

Figure 4.2: Čerenkov angle versus hadron momentum for the aerogel and $\mathrm{C_4F_{10}}$ gas. The dots represent experimental data collected at HERMES. The solid and broken curves correspond to the theoretical predictions.

The threshold momentum is calculated as

$$p_{th} = \frac{mc^2}{\sqrt{n^2 - 1}}, \tag{4.3}$$

where $\beta = 1/n$ for $\theta = 0$ is used. The threshold momenta of pions, kaons and protons for aerogel are 0.6, 2.0 and 3.8 GeV/c. In the momentum region less than the threshold, the RICH detector performs as a threshold Čerenkov counter. On the other hand, in the momentum region larger than the threshold, a measurement of the Čerenkov angle is required to identify hadrons. The maximum momentum for separation of two types of hadrons is

$$p_{max} = \sqrt{\frac{m_2^2 - m_1^2}{2\tan\theta \cdot n_\sigma(\sigma_\theta/\sqrt{N})}}, \tag{4.4}$$

where m_1 and m_2 are masses of two particles, θ is the Čerenkov angle, σ_θ is the angular resolution for single photon, N is the number of fired PMTs and n_σ is the number of standard deviation [67]. The value of $n_\sigma = 4.652$ is adopted in the design to achieve a misidentification of $\leq$ 1 %. The number of average fired PMTs is 11.2 for the aerogel and 13.1 for C_4F_{10}. The numerical values of p_{th} and p_{max} are summarized in Table 4.2 together with the characteristic values of HERMES RICH detector.

	aerogel (n=1.0303)	C_4F_{10} gas (n=1.00137)
averaged N_{PMT}	11.2	13.1
σ_θ	9.2	9.5
$p_{th}(\pi)$	0.6 GeV/c	2.7 GeV/c
$p_{th}(K)$	2.0 GeV/c	9.4 GeV/c
$p_{th}(p)$	3.8 GeV/c	17.9 GeV/c
$p_{max}(\pi/K)$	5.9 GeV/c	13.2 GeV/c
$p_{max}(K/p)$	10.0 GeV/c	22.3 GeV/c

Table 4.2: Threshold and maximum separation momenta for pion, kaon and proton.

Figure 4.3 illustrates the momentum ranges for hadron identification in both radiators. The emitted photons are reflected on the mirror array and generate rings on the PMT plane. A typical hit pattern on the PMT plane is shown in Figure 4.4. The larger (smaller) ring is due to photons emitted in aerogel (C_4F_{10} gas) by a positive pion at 4.4 GeV/c. For all the fired PMTs the Čerenkov angles are evaluated and hadron type is determined. The detail is discussed in Section 4.2.

4.1.1 Aerogel

Silica aerogel is used as a radiator for the RICH detector [68]. The typical refractive index of the aerogel at $\lambda = 633$ nm is 1.03 and the average size of a tile

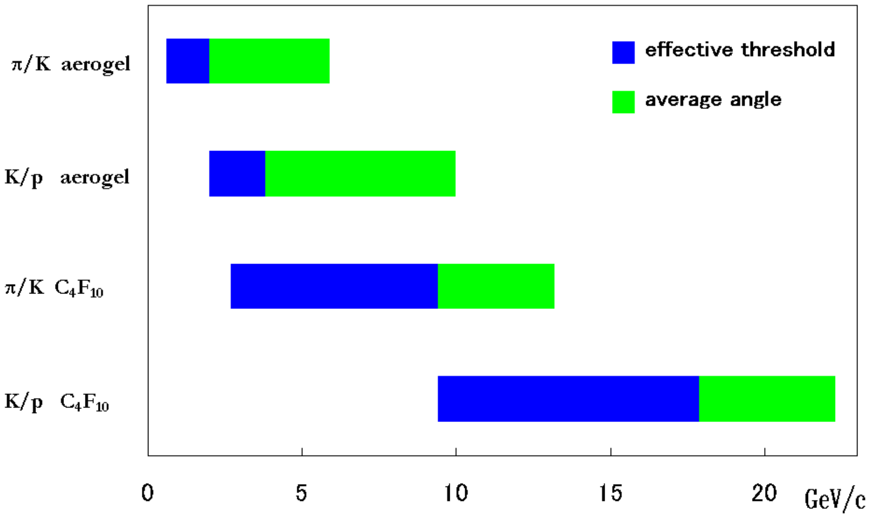

Figure 4.3: Momentum ranges for various hadron separations. In the darkly shaded region the information of the Čerenkov angle is not required for the the hadron identification, but only an information of whether the PMTs are fired or not is needed. On the other hand the Čerenkov angle is required in the lightly shaded region.

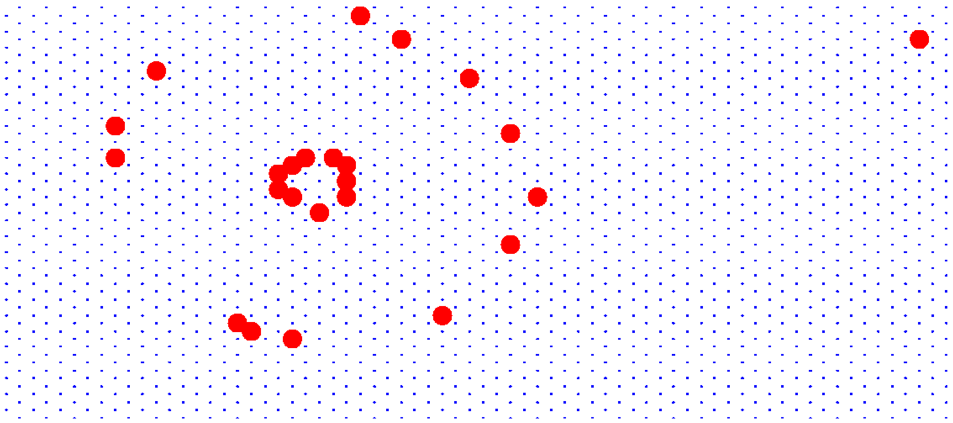

Figure 4.4: A hit pattern on the PMT plane by a positive pion at 4.4 GeV/c. The inner ring is due to C_4F_{10} gas and the outer due to aerogel.

is 11.4cm × 11.4cm × 1.13cm. The 1680 aerogel tiles were produced at Matsushita Electric Works [69, 70]. 348 aerogel tiles were excluded at the beginning due to visible crack and the refractive indices of 1332 aerogel tiles were measured at Tokyo Tech. The measurement is motived to achieve the distribution of the refractive index of the tiles below 1% as follows

$$\frac{\Delta(n-1)}{n-1} = 2\frac{\Delta\theta}{\theta} \leq 1\%. \tag{4.5}$$

It is therefore required to be Root Mean Square(RMS) of the indices is $\sigma \leq 3.0 \cdot 10^{-4}$. Figure 4.5 shows the distribution of the refractive indices of 1040 selected aerogel tiles. The standard deviation of the distribution is 4.1×10^{-4}, which does not satisfy the above condition. It is, however, possible to divide the tiles into two groups of which one half of tiles is with lower index and the other is with higher index for the top and bottom modules of RICH. Figure 4.6 shows the distributions of the refractive index for the two groups. The standard deviations of the distributions are 2.5×10^{-4} and 2.6×10^{-4}, which satisfy the above condition.

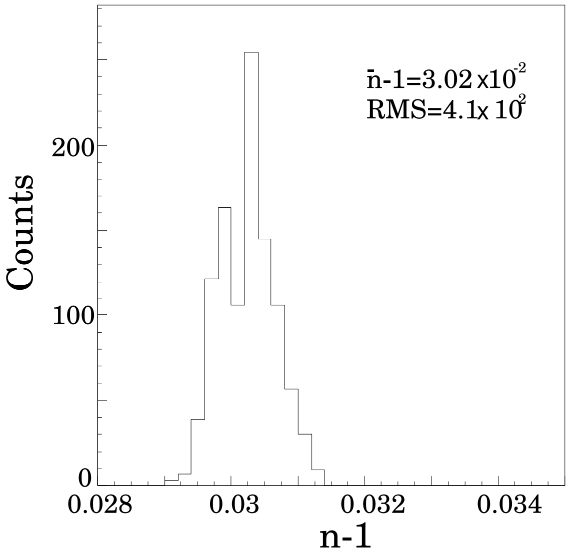

Figure 4.5: Distribution of the refractive indices of the 1040 selected aerogel tiles. The x-axis shows the value of $(n-1)$, where n is the refractive index of the aerogel.

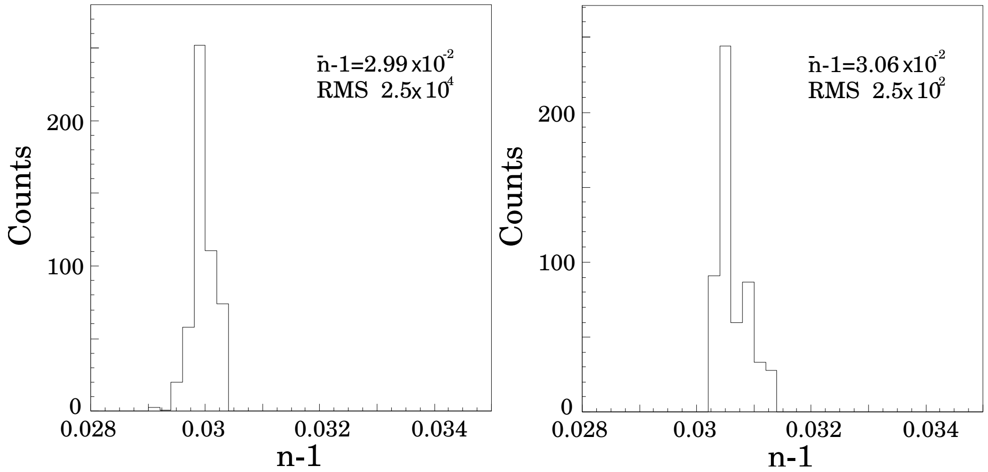

Figure 4.6: Distribution of refractive indices of aerogels for the two groups.

The transmission of light with wavelength λ in aerogel is given by

$$T = A \cdot \exp \frac{-C \cdot t}{\lambda^4}, \tag{4.6}$$

where A and C are Hunt parameters which characterize the aerogel properties and t represents the thickness of the material. For the HERMES RICH detector $C \cdot t = 0.0094$ μm^4 and $A = 0.964$ [68]. The term of λ^{-4} expresses the effect of the Rayleigh scattering. Photons with low wavelength can be easily scattered due to the effect. A lucite is installed at the back of the aerogel tiles to suppress the backgrounds. The lucite can cut off the photons with wavelength less than 280 nm. The schematic view of the shape of the edge of an aerogel tile and the wall of the aerogel tiles are shown in Figure 4.7 and Figure 4.8, respectively.

4.1.2 Mirrors

The mirror array which consists of eight segments is located at the back of $\mathrm{C_4F_{10}}$ gas. Čerenkov photons which passed through the radiators are reflected by the mirrors and detected by the photon detectors described in the next section. The dimension of each mirror is 252.4 cm by 79.4 cm. Measurements of the mirror reflectivity were performed before the RICH installation. The result is shown in Figure 4.9. As can be seen in the figure, a photon with wavelength of 300 - 600 nm has a reflectivity above 85 % [71].

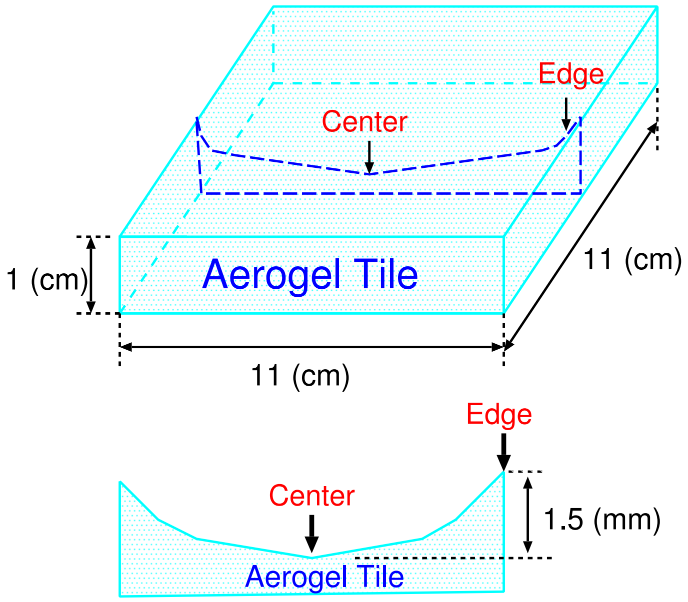

Figure 4.7: The shape of the edge of an aerogel tile.

4.1.3 Photon Detector

The photo-multipliers (PMTs) detect the reflected Čerenkov photons by the mirror. 1934 Philips XP1911 PMTs are used in each RICH detector half. The diameter of the PMT is 18.6 mm. The elementary cell of the PMT is a hexagon with the distance between opposite sides 23.3 mm. The PMTs are arranged as shown in Figure 4.10. The PMT photo-cathodes can cover approximately 40% of the PMT plane. Aluminized plastic foil funnels surround the PMT photo-cathodes, which increases the coverage of PMT to 91%.

4.2 Identification Method

4.2.1 Determination of the Čerenkov angle

In this section, an identification method of hadron type which is called Indirect Ray Tracing (IRT) is introduced. Since the momentum vector of the particle $\vec{p}$ is known, it is only required to determine the Čerenkov angle θ for identifying hadron (See Eq. (4.2)). A schematic diagram of an event in which charged par-

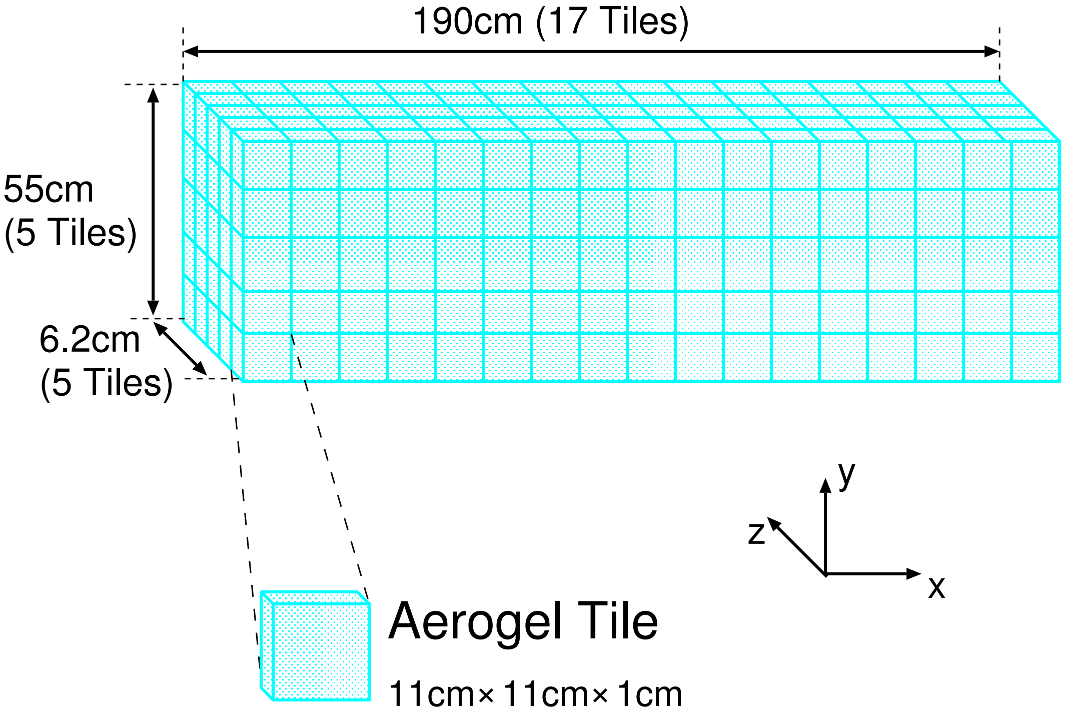

Figure 4.8: The schematic view of the wall of the aerogel tiles.

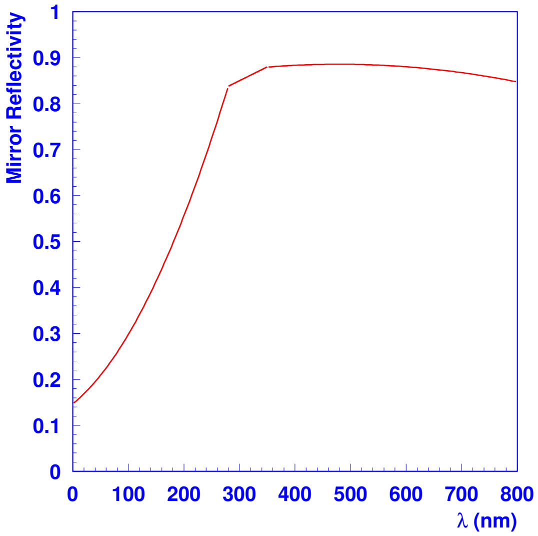

Figure 4.9: The mirror reflectivity as a function of the wavelength of the Čerenkov photon.

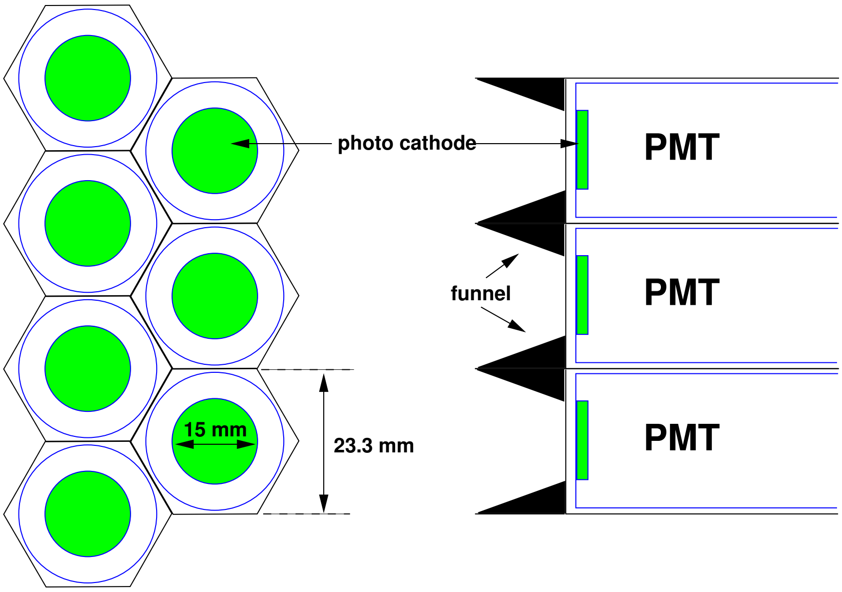

Figure 4.10: The schematic view of PMTs

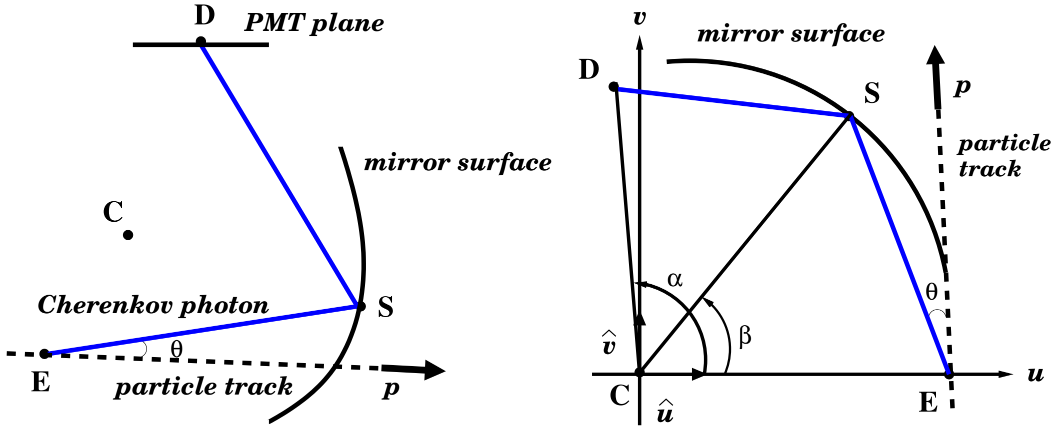

Figure 4.11: Definition of angles, vertices and vectors used in the IRT method.

ticles pass through the RICH detector is shown in Figure 4.11. The reflection point $\boldsymbol{S}$ is determined from the detected point $\boldsymbol{D}$ and the emission point $\boldsymbol{E}$ of the Čerenkov radiation which is assumed to be the middle of track inside the radiator. The Čerenkov angle is calculated from the inner product of $\overrightarrow{SE}$ and $\vec{\boldsymbol{p}}$. The Euclid base system with C as the origin is chosen as shown in the right panel of Figure 4.11. The vector $\hat{u}$ represents the unit vector along $\overrightarrow{CE}$ and $\hat{v}$ is the orthogonal unit vector to the vector $\hat{u}$. From the known lengths and angles ($|\overrightarrow{CD}| \equiv d, |\overrightarrow{CE}| \equiv a, |\overrightarrow{CS}| \equiv R, \alpha$ and $\vec{\boldsymbol{p}}$), the components of the vectors are written as follows

$$\begin{aligned} \overrightarrow{CE} &= (a, 0, 0), \\ \overrightarrow{CD} &= (d\cos\alpha, d\sin\alpha, 0), \\ \overrightarrow{CS} &= (R\cos\beta, R\sin\beta, 0). \end{aligned} \tag{4.7}$$

The vectors $\overrightarrow{SC}, \overrightarrow{SD}$, and $\overrightarrow{SE}$ can be expressed by linear combinations of the vectors as

$$\begin{aligned} \overrightarrow{SC} &= -\overrightarrow{CS} &&= (-R\cos\beta, -R\sin\beta, 0), \\ \overrightarrow{SD} &= \overrightarrow{CE} - \overrightarrow{CS} &&= (a - R\cos\beta, -R\sin\beta, 0), \\ \overrightarrow{SE} &= \overrightarrow{CD} - \overrightarrow{CS} &&= (d\cos\alpha - R\cos\beta, d\sin\alpha - R\sin\beta, 0). \end{aligned} \tag{4.8}$$

Because the incident angle of the Čerenkov photon to the mirror should be the same as its reflection angle, the outer product of the unit vectors $\hat{\boldsymbol{SC}}$ and $\hat{\boldsymbol{SE}}$

should satisfy the following equation:

$$\begin{aligned} \hat{\boldsymbol{SC}} \times \hat{\boldsymbol{SE}} &= \hat{\boldsymbol{SD}} \times \hat{\boldsymbol{SC}}, \qquad (4.9) \\ \hat{\boldsymbol{SC}} \cdot \hat{\boldsymbol{SE}} &= \hat{\boldsymbol{SD}} \cdot \hat{\boldsymbol{SC}}. \qquad (4.10) \end{aligned}$$

Eq. (4.9) and Eq. (4.10) can be expressed from Eq. (4.8) as follows

$$\begin{aligned} a\sin\beta|\overrightarrow{SD}| &= d(-\cos\alpha\sin\beta + \sin\alpha\cos\beta)|\overrightarrow{SE}|, \qquad (4.11) \\ (a\cos\beta - R)|\overrightarrow{SD}| &= \left(d\left(\cos\alpha\cos\beta + \sin\alpha\sin\beta\right) - R\right)|\overrightarrow{SE}|. \qquad (4.12) \end{aligned}$$

The ratio of each side of Eq. (4.12) to those of Eq. (4.11) is

$$\frac{a\cos\beta - R}{a\sin\beta} = \frac{d(\cos\alpha + \sin\alpha\sin\beta) - R}{d(\sin\alpha\cos\beta - \cos\alpha\sin\beta)}. \qquad (4.13)$$

Eq. (4.13) can be simply written as

$$ad\sin(\alpha - 2\beta) + R(a\sin\beta - d\sin(\alpha - \beta)) = 0. \qquad (4.14)$$

β can be calculated from the equation by using Newton-Raphson iterations with numerical calculations. The vector of the track of Čerenkov photon $\overrightarrow{ES}$ can be obtained and Čerenkov angle can be determined as

$$\theta = \frac{\cos^{-1}\overrightarrow{ES} \cdot \vec{\boldsymbol{p}}}{|\overrightarrow{ES}| \cdot |\vec{\boldsymbol{p}}|}. \qquad (4.15)$$

4.2.2 Likelihood Technique

The Čerenkov angle is experimentally determined for each radiator and compared with the theoretically calculated Čerenkov angles θ_{th} assuming a particle type. From Eq. (4.1) θ_{th} can be related to the momentum p and the mass m of the particle h as

$$\theta_{th} = \cos^{-1}\left(\frac{1}{n} \cdot \sqrt{1 + \left(\frac{m_h}{p_h}\right)^2}\right). \qquad (4.16)$$

For each hypothesis (h = π, K, p), a likelihood is calculated as

$$L(\langle\theta_i\rangle) = \exp\left\{-\frac{(\theta_i^{th} - \langle\theta_i\rangle)^2}{2\sigma_{\langle\theta\rangle}^2}\right\}, \qquad (4.17)$$

where $\langle\theta\rangle$ is the average value of Čerenkov angle θ determined experimentally and $\sigma_{\langle\theta\rangle}$ represents the average angle resolution. It can be related to the single photon resolution σ_γ as follow

$$\sigma_{\langle\theta\rangle} = \frac{\sigma_\gamma}{\sqrt{\langle N_{PMT}\rangle - 1}}, \tag{4.18}$$

where N_{PMT} represents the number of fired PMTs. When the RICH detector performs as the threshold Čerenkov detector, the likelihood is set to $L_{s.th.} = 0.5$. Furthermore if the number of fired PMTs is below the background level, the likelihood L_{min} is calculated as

$$L_{min} = L(\theta^{th} + 2\sigma_\gamma) = \exp(-2 \cdot (\langle N_{PMT}\rangle - 1)) = \begin{cases} 0.5 \cdot 10^{-5} \text{ for aerogel} \\ 0.2 \cdot 10^{-8} \text{ for C}_4\text{F}_{10} \text{ gas} \end{cases} \tag{4.19}$$

Figure 4.12 shows the algorithm of the likelihood calculation.

4.3 PID Efficiency

In this section, a correction of the identified hadron yield is discussed. The likelihood is calculated for each hadron type as described in the previous section. A hypothesis with the largest likelihood is adopted. The number of particles is represented as N_t^i, where a superscript i and a subscript t are identified particle type and true particle type respectively. For instance N_K^π represents the number of kaon identified as pion; true particle type is kaon but is misidentified as pion.

A matrix $\boldsymbol{N}$ is expressed as

$$\boldsymbol{N} = \begin{pmatrix} N_\pi^\pi & N_K^\pi & N_p^\pi \\ N_\pi^K & N_K^K & N_p^K \\ N_\pi^p & N_K^p & N_p^p \end{pmatrix}. \tag{4.20}$$

The summation of the elements of a column and a row are the number of identified particle and the number of true particle respectively:

$$\sum_i N_t^i \equiv N_t, \tag{4.21}$$

$$\sum_t N_t^i \equiv I^i. \tag{4.22}$$

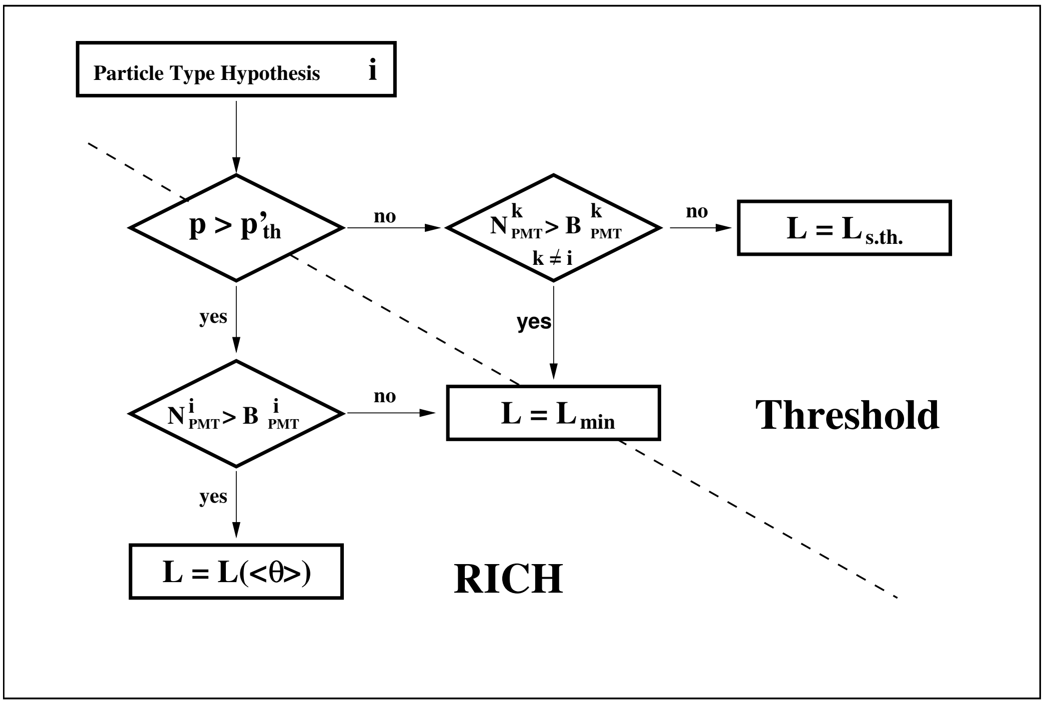

Figure 4.12: The algorithm of the likelihood calculation. p'_{th} is the momentum threshold, B_{PMT} represents the number of the fired PMTs due to background.

They form vectors $\vec{\boldsymbol{I}}$ and $\vec{\boldsymbol{N}}$:

$$\vec{\boldsymbol{N}} = (N_\pi, N_K, N_p), \tag{4.23}$$
$$\vec{\boldsymbol{I}} = (I^\pi, I^K, I^p). \tag{4.24}$$

The vector $\vec{\boldsymbol{N}}$ corresponds to true hadron yield, while the vector $\vec{\boldsymbol{I}}$ represents measured hadron yield. The identification probability P_t^i is defined as the ratio of N_t^i to N_t:

$$P_t^i = \frac{N_t^i}{N_t}. \tag{4.25}$$

A matrix $\boldsymbol{P}$ (P-matrix) is written as

$$\boldsymbol{P} = \begin{pmatrix} P_\pi^\pi & P_K^\pi & P_p^\pi \\ P_\pi^K & P_K^K & P_p^K \\ P_\pi^p & P_K^p & P_p^p \end{pmatrix}. \tag{4.26}$$

The columns of the matrix are normalized to 1 due to the definition of the probabilities:

$$\sum_i P_t^i = 1. \tag{4.27}$$

The P-matrix is related to the vector $\vec{\boldsymbol{I}}$ and $\vec{\boldsymbol{N}}$ as

$$\vec{\boldsymbol{I}} = \boldsymbol{P} \cdot \vec{\boldsymbol{N}}. \tag{4.28}$$

If the P-matrix is nonsingular, the following equation can be obtained:

$$\vec{\boldsymbol{N}} = \boldsymbol{P}^{-1} \cdot \vec{\boldsymbol{I}}. \tag{4.29}$$

The P-matrix is a function of the momentum of the particle since the precision of the determination of the Čerenkov angle depends on the momentum. In case of non single track, the precision decreases due to the overlapping of the Čerenkov rings. Hence the P-matrix is prepared for one track, two tracks and more than two tracks separately. Figure 4.13 shows normalized track number per a detector half. As can be seen, one track events ($\simeq$ 88%) are dominating in the experiment.

The P-matrix is determined using a Monte Carlo (MC) simulations. Parameters for the RICH description in MC such as the mirror roughness and dispersion relation of aerogel and $\mathrm{C_4F_{10}}$ gas were tuned to reproduce the experimental data

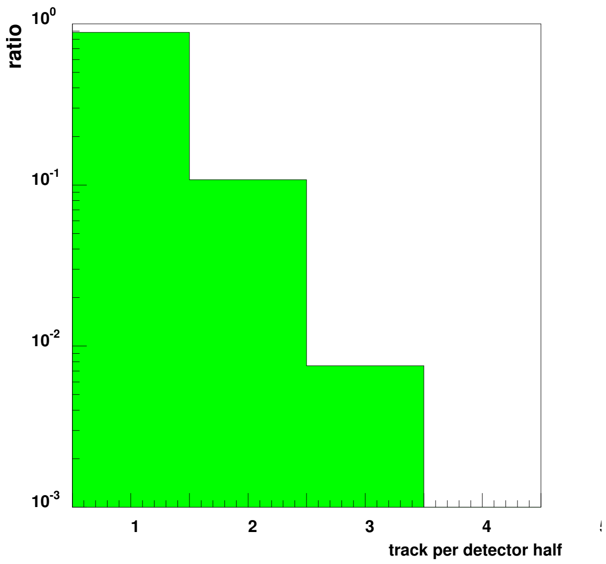

Figure 4.13: Normalized Track number per a detector half measured in the experiment.

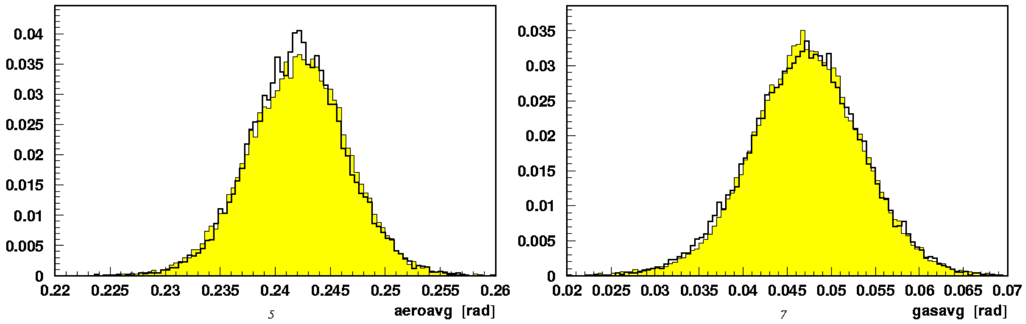

Figure 4.14: Čerenkov angles for aerogel (left plot) and C_4F_{10} gas (right plot). The yellow and black histograms correspond to the experimental data and the MC data, respectively.

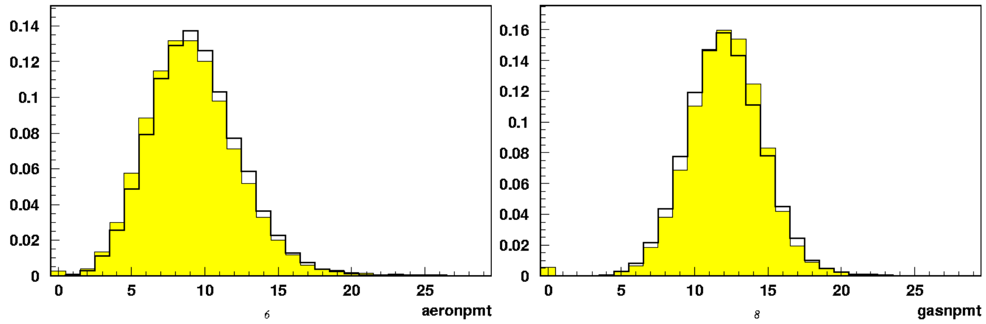

Figure 4.15: Photon yields for aerogel (left plot))and C_4F_{10} gas (right plot)). The yellow and black histograms correspond to the experimental data and the MC data, respectively.

of the Čerenkov angle and photon yield. Figure 4.14 and 4.15 show the comparison of the measured and the simulated Čerenkov angles and the photon yield, respectively.

The P-matrix for 1, 2 and 3 tracks was extracted using the MC simulation and is shown as a function of the particle momentum in Figure 4.16 - 4.18 . The values of the P-matrices are listed in Table A.1 - A.3. There is a sudden dip for kaon efficiency around p =10 GeV/c. It corresponds to the threshold momentum of kaon for C_4F_{10} gas.

4.3.1 Systematic Uncertainties of P-Matrix

There are several different contributions to systematic uncertainties on the P-matrix.

Finite Pixel Size of PMTs:

The Čerenkov angle was calculated based on assumption that the Čerenkov photon hits at the center of a PMT. The systematic uncertainties arising from this assumption can be evaluated shifting the Čerenkov photon detection point randomly within a PMT pixel surface (Figure 4.19).

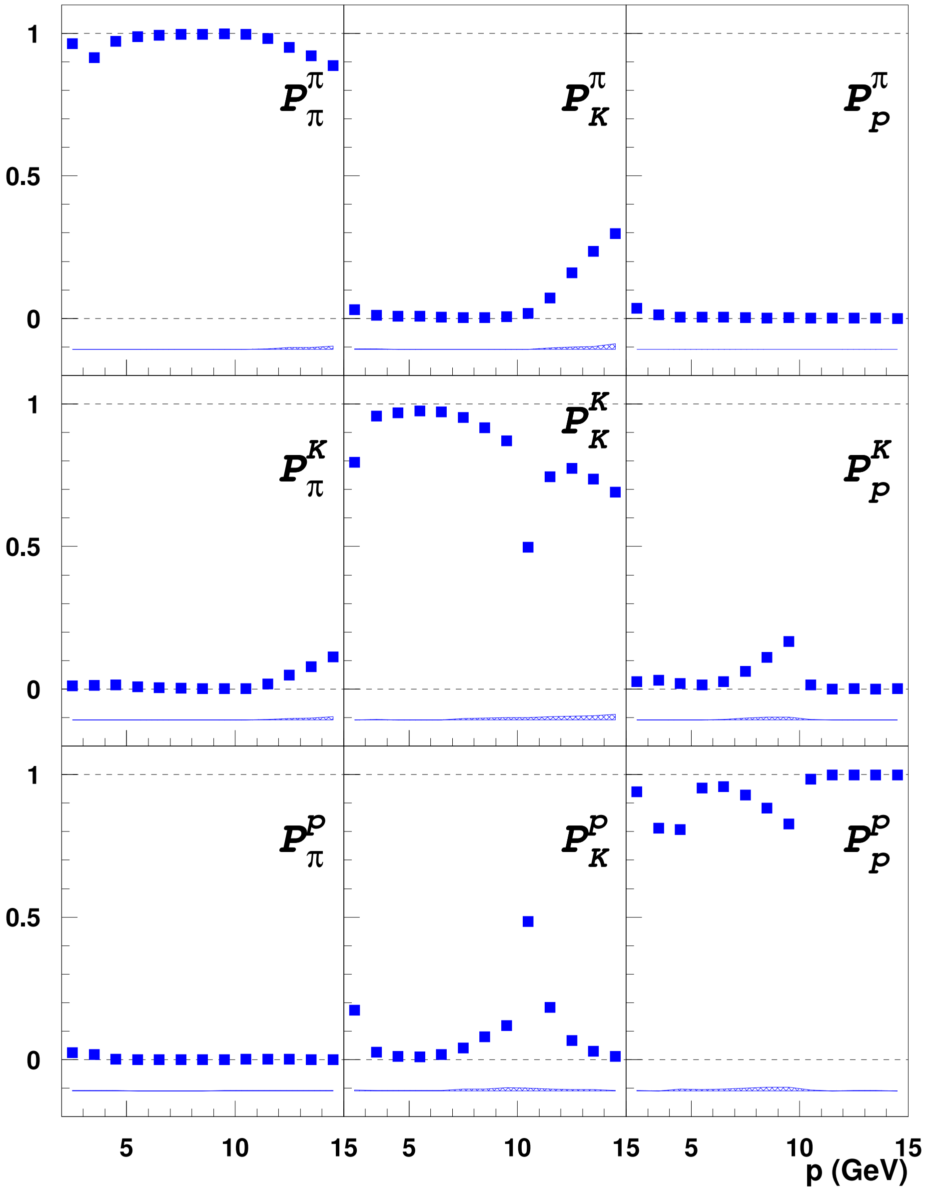

Figure 4.16: P-matrix for 1 track extracted by the Monte Carlo simulation.

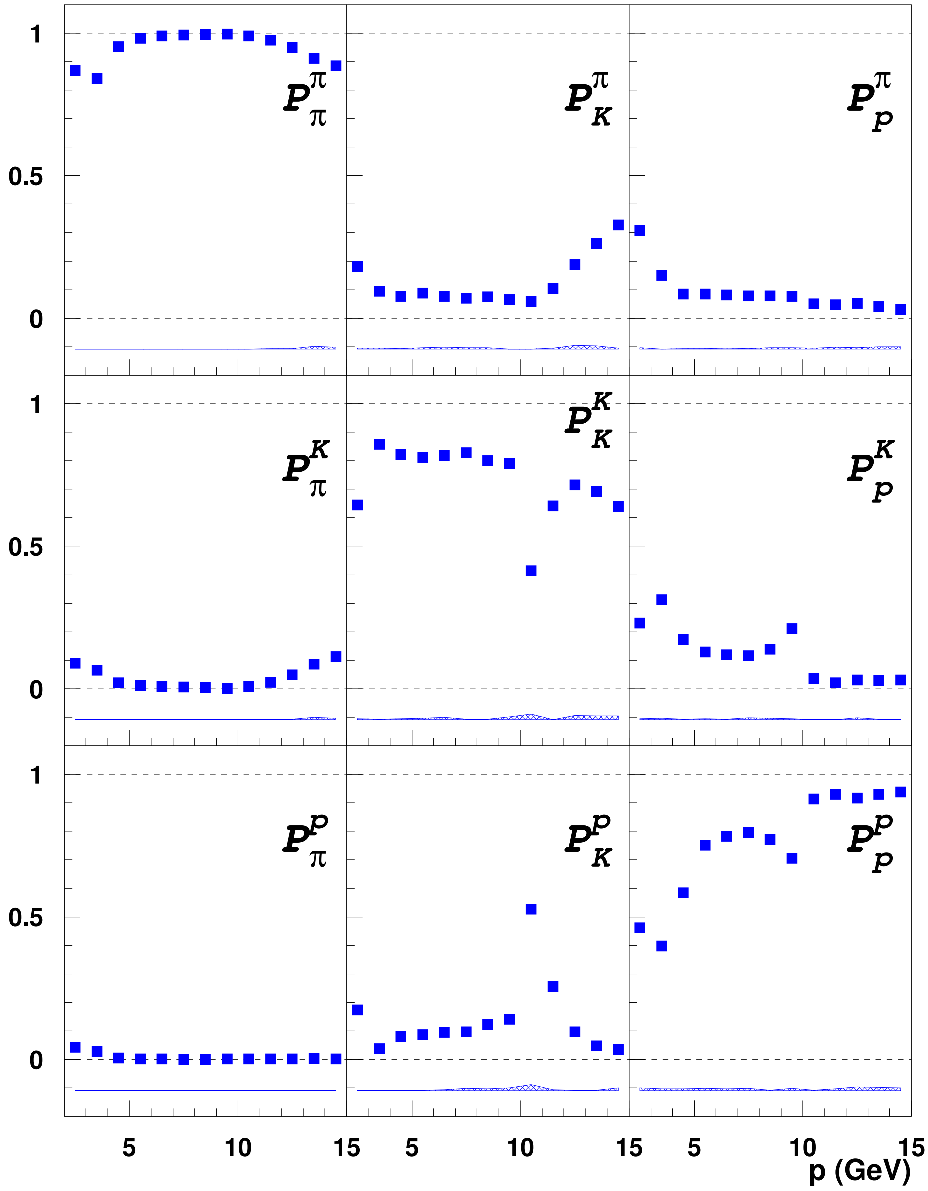

Figure 4.17: P-matrix for 2 track extracted by the Monte Carlo simulation.

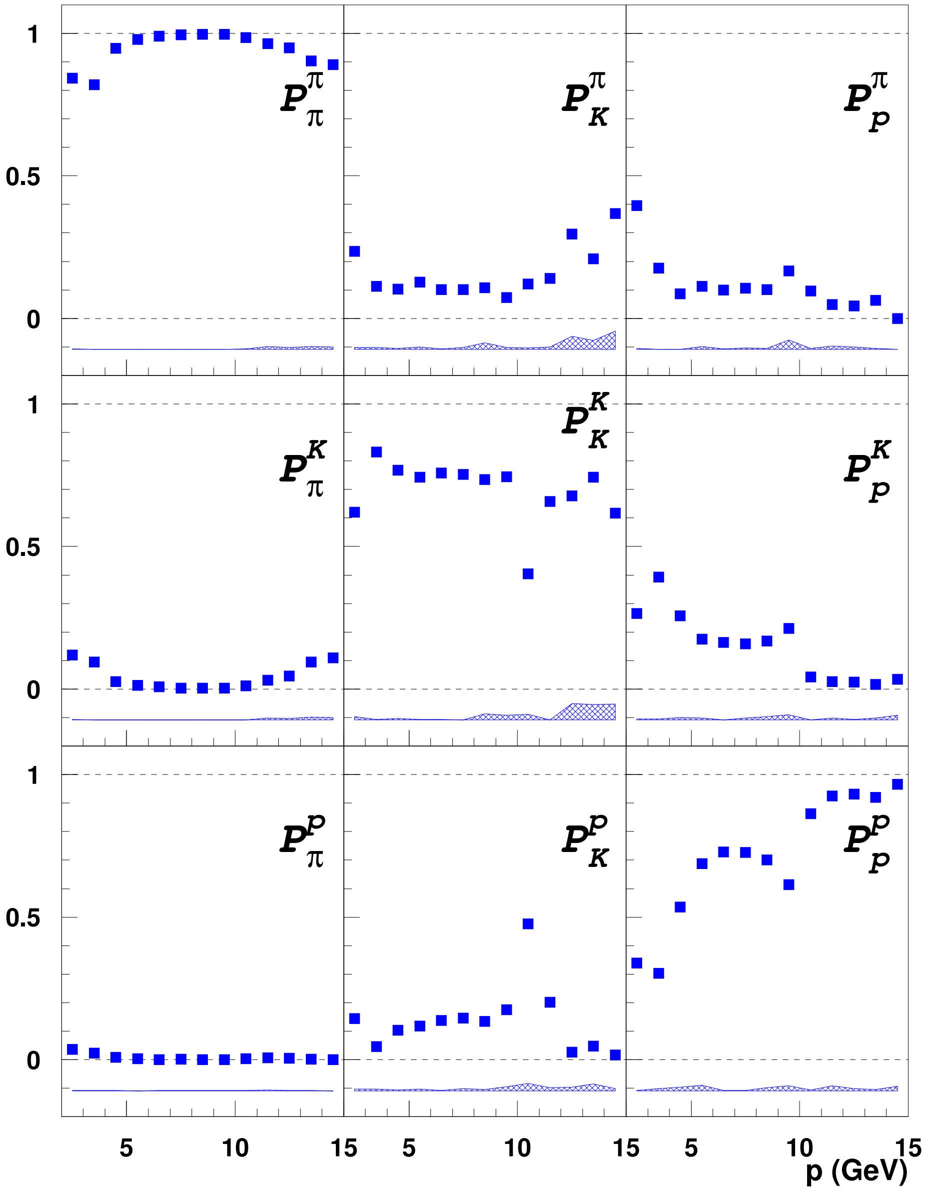

Figure 4.18: P-matrix for 3 track extracted by the Monte Carlo simulation.

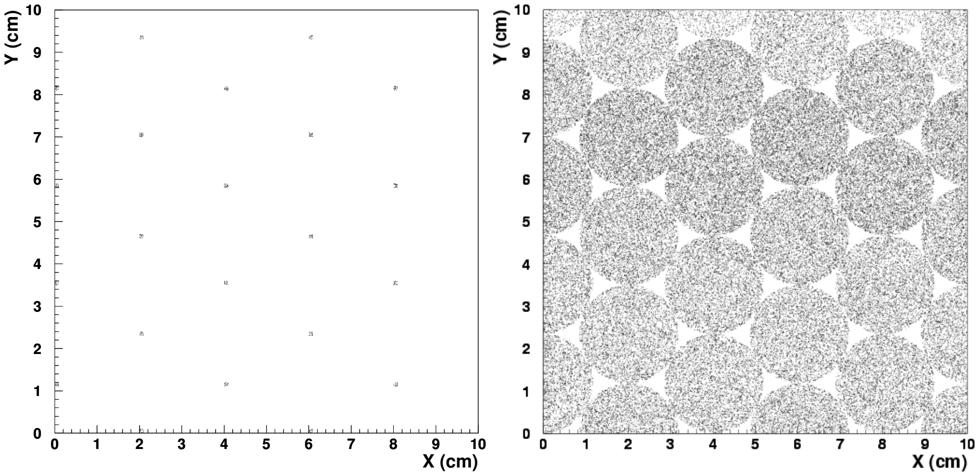

Figure 4.19: Distribution of Čerenkov photon detection vertex on a PMT surface. The right panel shows the positions of the center of PMTs. In the left panel, the position is randomly moved within the PMT surface to calculate the Čerenkov angle.

Edge Effect of Aerogel Tiles:

The aerogel tiles were produced with the typical dimensions $11 \times 11 \times 1\mathrm{cm}^3$. However, it was found that the aerogel tiles have the sharply curved surface (Figure 4.20). The contribution of the effect is discussed in detail in [72]

Chromatic Aberration:

The refractive index for aerogel $n_{aerogel} = 1.0304$ was measured at a wavelength $\lambda = 400$ nm. However, it varies with the wavelength of Čerenkov light. The contribution from this was estimated by varying the refractive indices using the following equation:

$$\begin{aligned} n_{aerogel} &= 1.02804 + 0.789308 \times 10^{-3} \times \exp\left(0.368298 \times E_\gamma\right), \quad (4.30) \\ n_{\mathrm{C_4F_{10}}} &= 1.001287 + 1.723 \times 10^{-7} \times E_\gamma + 5.495 \times 10^{-6} \times E_\gamma^2, \quad (4.31) \end{aligned}$$

where E_γ represents the energy of the Čerenkov light.

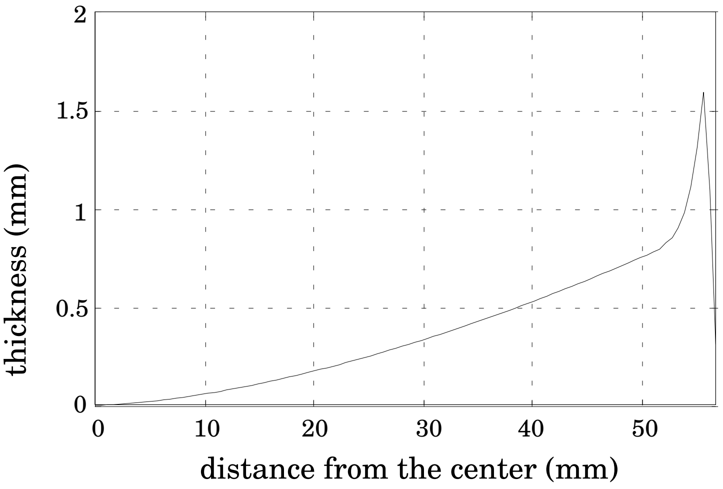

Figure 4.20: The surface of an aerogel tile

Time Variation of the Refractive Index:

The refractive indices of the aerogel tiles could vary with times over years. The time variation of the other radiator C_4F_{10} gas arises from the pressure of the atmosphere. The effect was estimated from the difference between actually measured refractive indices and values used at the beginning of 1998 when the RICH detector was installed.

Emission Vertex of Čerenkov Photon:

The emission point of Čerenkov photon in the radiator can be not determined in the experiment. Therefore Čerenkov angles are evaluated assuming that the photon is emitted at the center of a track inside the radiator. In the same way as the finite PMT size, the emission vertex was moved randomly along the particle track in the radiator to evaluate the effect of the assumption.

Angular resolutions for single photon from these sources are listed in Table 4.3.1.

An emphasis should be put on that P-matrix is extracted using the HEMRES Monte Carlo (HMC) simulation. Therefore these contributions from imperfection of RICH description in the HMC simulation could be included.

Source	Aerogel (mrad)	C_4F_{10} gas (mrad)
Pixel Size	5.6	5.2
Edge Effect	3.0	-
Chromatic Aberration	2.5	-
Refractive Index	1.1	-
Emission Point	1.8	2.2

Table 4.3: Contributions to angular resolutions for single photon.

Imperfection of RICH description

The systematic uncertainty of the P-matrix from imperfection of RICH description in HMC was evaluated comparing the discrepancy between the P-matrices from experimental data and HMC. To determine the P-matrix from experimental data, the events containing a decaying particle such as $\rho, \phi, \Lambda, K_s^0$ are used. The decaying particle has the information on the particle types of the tracks. Here the details are given taking (the decay mode) $\phi \rightarrow K^+K^-$. Events are selected containing two tracks beside the positron track. The event selection included constraints on the event topology: the two reconstructed tracks must be close enough to the target. The invariant mass of the two hadrons is calculated assuming that the two tracks are kaons. If the tracks come from the ϕ decay, the peak should be found around 1020 MeV corresponding to ϕ meson mass. The efficiency for kaons can be evaluated from Eq. (4.25). Figure 4.21 shows the invariant mass distribution of the two particles. In this case, kaons were not misidentified as pions but as protons. The misidentification of kaons as pions is sensitive in the low momentum region, while the misidentification as proton is sensitive to high momentum region.

4.4 RICH Error Propagation to Hadron Yield

As mentioned in Section 4.3, true hadron yield $\vec{\boldsymbol{N}}$ is related to measured hadron yield $\vec{\boldsymbol{I}}$ via

$$\vec{\boldsymbol{N}} = P^{-1} \cdot \vec{\boldsymbol{I}}. \tag{4.32}$$

The P-matrix has the systematic uncertainties ΔP described in the previous section. The propagation of the systematic uncertainties to hadron yield can be evaluated by replacing P with $(P + \Delta P)$ in the above equation.

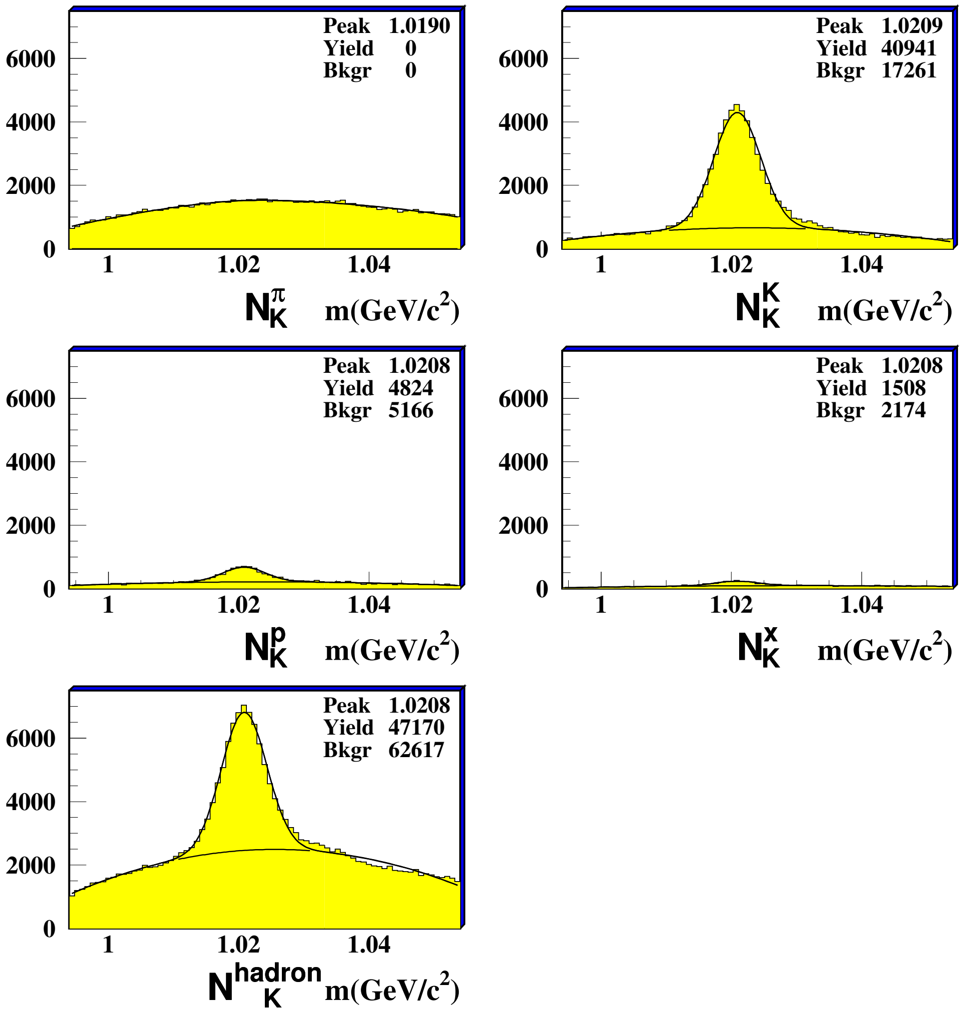

Figure 4.21: Invariant mass distributions of the two particles. Assuming that the particles are both kaons, the kaon mass is used in the calculation. X represents not identified hadrons with the RICH detector.

The resulting fractional uncertainties on hadron yield due to the RICH systematic uncertainties are shown in Figure 4.22. The numerical values are presented in Table A.5. The fractional uncertainties of the both positive and negative pion yield due to the RICH systematic uncertainties are less than 1.5%, while those of kaon strongly depend on the charge of the particle: The corresponding values for positive kaon are less than 6 % while 12 % for negative kaon. The reason is that the ratio of the positive kaon flux to the positive pion flux is different from the same ratio for the negatively charged particle. Figure 4.23 presents the kaon and proton flux normalized by the pion flux. The numerical values are shown in Table A.4. As can be seen, the negative kaon yield amounts 10 % of negative pion, while the positive kaon yield amounts 20 % of positive pion. It indicates that the same systematic uncertainty on the P-matrix yields two times large contribution to the negative kaon yield than the positive, due to the hadron population in the data sample.

The fractional uncertainties monotonously decrease with x. It could be understood as follows. From Eq. (2.2) and Eq. (2.3), the Bjørken scaling variable x is re-written as

$$x \overset{\text{lab}}{=} \frac{2EE'}{M(E-E')}\sin^2\frac{\theta}{2} = \frac{2E}{M}\sin^2\frac{\theta}{2}\left(\frac{E}{\nu}-1\right). \tag{4.33}$$

Thus x effectively determines the energy of the virtual photon. At small x, the energy of the virtual photon ν is large, while at high x, ν is small. The virtual photon with high (low) energy yields a hadron with high (low) momentum. The systematic uncertainty in the hadron identification with RICH increases with the momentum of the particle (see Figure 4.16 - 4.17). Hence the fractional uncertainties on hadron yield decrease with x.

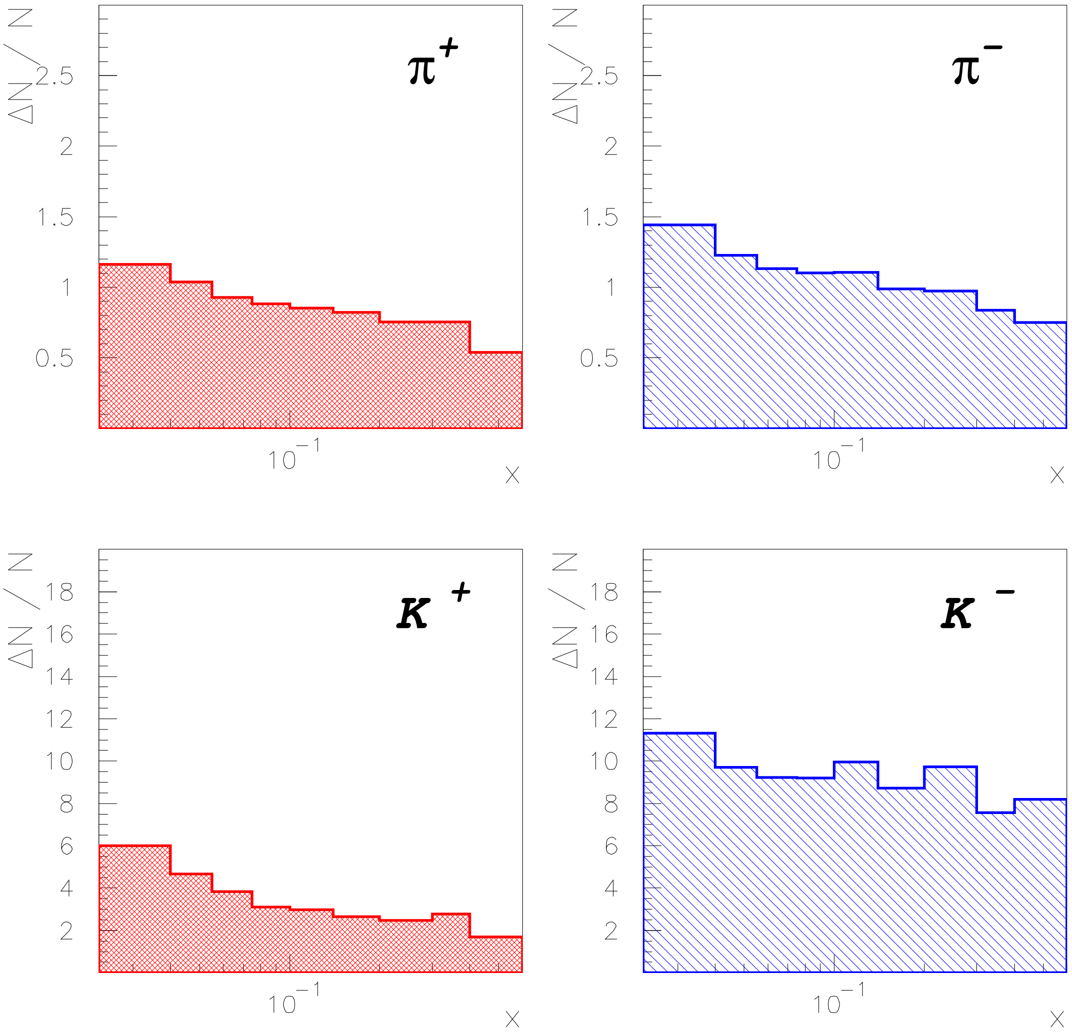

Figure 4.22: Fractional uncertainties on hadron yield arising from the RICH systematic uncertainties as a percentage.

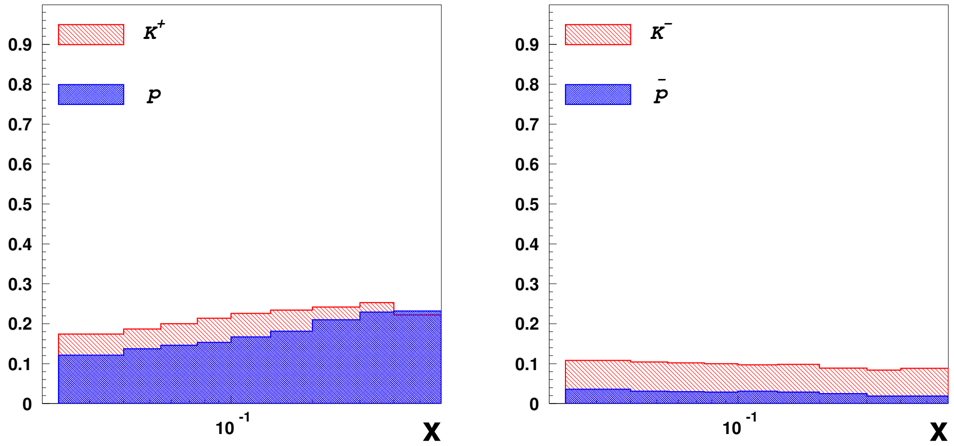

Figure 4.23: kaon and proton flux normalized by pion flux. The left plot is for positively charged particle and the right one for negatively. The lightly shaded region is the distribution for kaon. The proton distribution indicated as the darkly shaded region is overwritten in the corresponding panel.

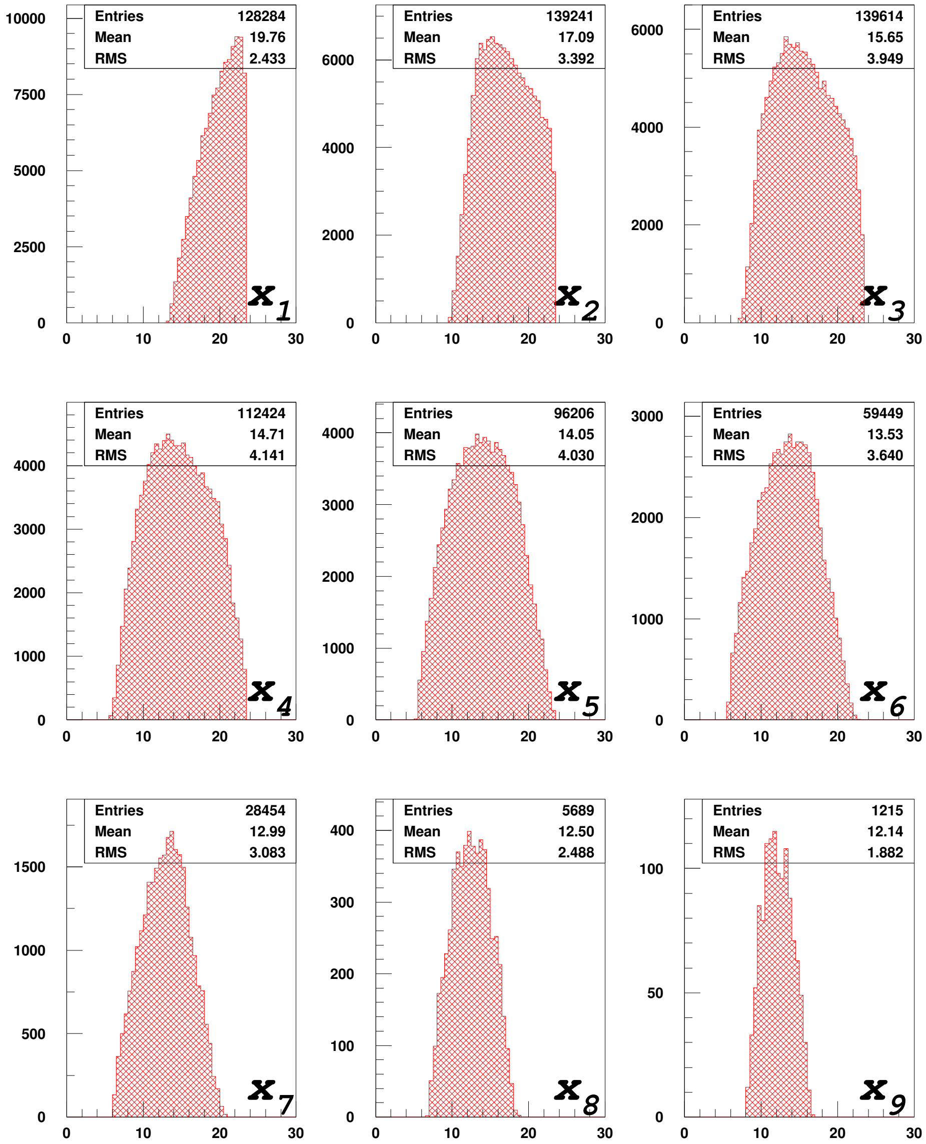

Figure 4.24: ν distributions for pion. The top three panels show the distribution at $x = 0.033, 0.047, 0.065$, the middle three panels at $x = 0.087, 0.119, 0.168$, and the bottom three panels at $x = 0.245, 0.342, 0.466$.

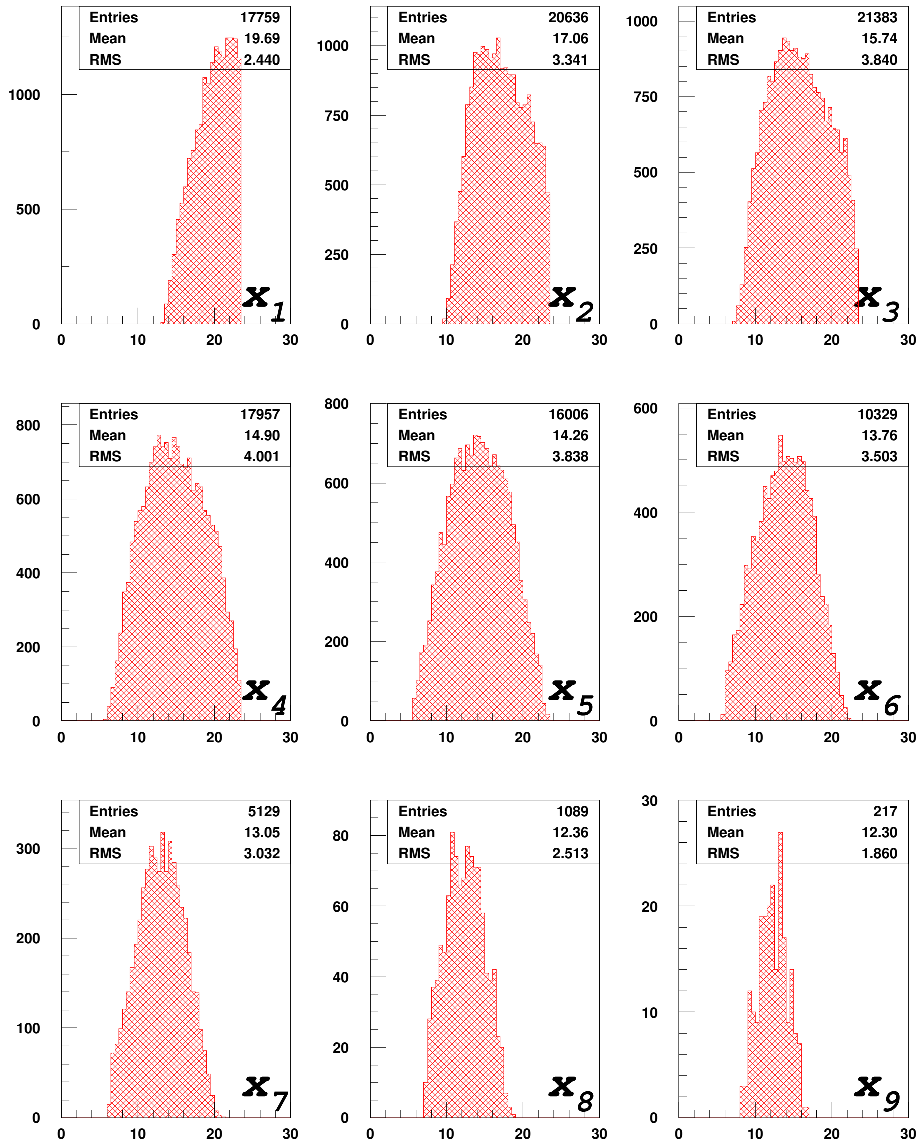

Figure 4.25: ν distributions for kaon. The top three panels show the distribution at $x = 0.033, 0.047, 0.065$, the middle three panels at $x = 0.087, 0.119, 0.168$, and the bottom three panels at $x = 0.245, 0.342, 0.466$.

Chapter 5

Double Spin Asymmetries

In this chapter, the photo absorption asymmetries A_1 are determined. For this purpose, the DIS and SIDIS (semi-inclusive DIS) events are selected from the collected data at the HERMES experiment. Then the cross section asymmetries $A_{||}$ are calculated and finally A_1 are determined from the Eq. (2.42).

5.1 Data Production

In this section, a stream of data production is described. The HERMES raw data which contain the detector readout are stored on disk and on tape in EPIO [73] format. The other informations such as beam and target status, the high voltage of the detectors, and so on, are also stored every 10 sec. These are called slow control data. The time interval is called $burst$. The HERMES decoder (HDC) allows to convert the raw data in EPIO format into ADAMO [74] format. Then the decoded data are reconstructed based on existing detector calibrations by the HERMES reconstruction program (HRC) [75]. They are synchronized with the slow control data and produce inputs for the so-called μDST (micro-Data Summary Tape). The data are summarized in $runs$ corresponding to about 450 Mbyte of recorded data. The typical time length of a run is 2 - 10 minutes which depends on the current of the positron beam. Another important time length is $fill$ defined as the lifetime of the positron beam in HERA which is typically 7 hours.

5.2 Data Selection

The data stored in the μDSTs are selected following the beam, target and detector conditions for the analysis.

5.2.1 Beam and Target Qualities

The current of the positron beam is about 35 mA at the beginning of a fill. The experimental data for the polarized target are collected until the current goes down to about 20 mA. Then HERMES performs the second experiment with high density unpolarized target (D, Kr and Xe) for an hour. As mentioned in Section 3.1, the beam polarization is about 60 % during data taking with the polarized targets. The requirements for the beam conditions for the analysis are

$$5 \text{ mA} \leq I_B \leq 50 \text{ mA},$$

$$30\% \leq P_B.$$

Concerning the target condition, the data which are taken during flipping the direction of the target polarization were removed for the analysis. The target polarization is flipped every 45 seconds.

5.3 Event Selection

To select inclusive DIS events as well as semi-inclusive DIS events, geometrical and kinematic cuts are applied to every track which passed the data quality selection described above. They are summarized in Table 5.3.

5.3.1 Geometrical Cuts

To ensure that the events are originated from interactions of the positron beam and the target, the geometrical cuts are applied. As described in Section 3.3, the acceptance cuts of $|\theta_x| \leq$ 170 mrad and 40 mrad $\leq |\theta_y| \leq$ 140 mrad are applied. Cuts of $d_{vert} \leq 0.75$ cm and $z_{vert} \leq 18$ cm require that tracks are originated in the target cell. Cuts on the position of the calorimeter ($|x_{calo}| \leq 175$ cm and $30 \text{ cm} \leq |y_{calo}| \leq 100 \text{ cm}$) are used to ensure that an electromagnetic shower due to the scattered positron is created in the calorimeter and the center of a cluster must not be too close to the edge of the calorimeter wall.

Geometrical cuts	
Horizontal scattering angle	$\|\theta_x\| \leq$ 170 mrad
Vertical scattering angle	40 mrad $\leq \|\theta_y\| \leq$ 140 mrad
x position of calorimeter	$\|x_{calo}\| \leq$ 175 cm
y position of calorimeter	30 cm $\leq \|y_{calo}\| \leq$ 175 cm
Longitudinal vertex position	$\|z_{vert}\| \leq$ 18 cm
Transverse vertex position	$d_{vert} \leq$ 0.75 cm
Kinematic cuts for inclusive DIS	
Squared invariant mass of the virtual photon	1.0 $\mathrm{GeV}^2 \leq Q^2$
Invariant mass of the final hadron state	10.0 $\mathrm{GeV}^2 \leq W^2$
Separation from hadrons	$\mathrm{PID} > 1$
Energy deposit in the calorimeter	3.5 GeV $\leq E_{calo}$
Fractional energy transfer	$y \leq$ 0.85
Kinematical cuts for semi-inclusive DIS	
Separation from hadrons	$\mathrm{PID} < 0$
Feynman variable	0.1 $\leq x_F \leq$ 1.0
Fractional energy of the hadron	0.2 $\leq z \leq$ 0.8
Momentum of pions and kaons	4.0 GeV $\leq p \leq$ 13.8 GeV

Table 5.1: Geometrical and kinematic cuts for the selection of DIS and SIDIS events.

5.3.2 Kinematic cuts for DIS events

Cuts on inclusive DIS events

To select DIS events, a cut on of 1.0 $\mathrm{GeV}^2 \leq Q^2$ is used as well as a cut on the squared invariant mass of the final hadronic state of 10.0 $\mathrm{GeV}^2 \leq W^2$. A cut on energy deposit in the calorimeter is required to be 3.5 GeV $\leq E_{calo}$ in order to select the scattered positron. The criterion on the fractional energy transfer $y \leq$ 0.85 selects the DIS events for first order QED process. The distribution of the selected DIS events is shown in Figure 5.1 in the kinematic $x - Q^2$ plane.

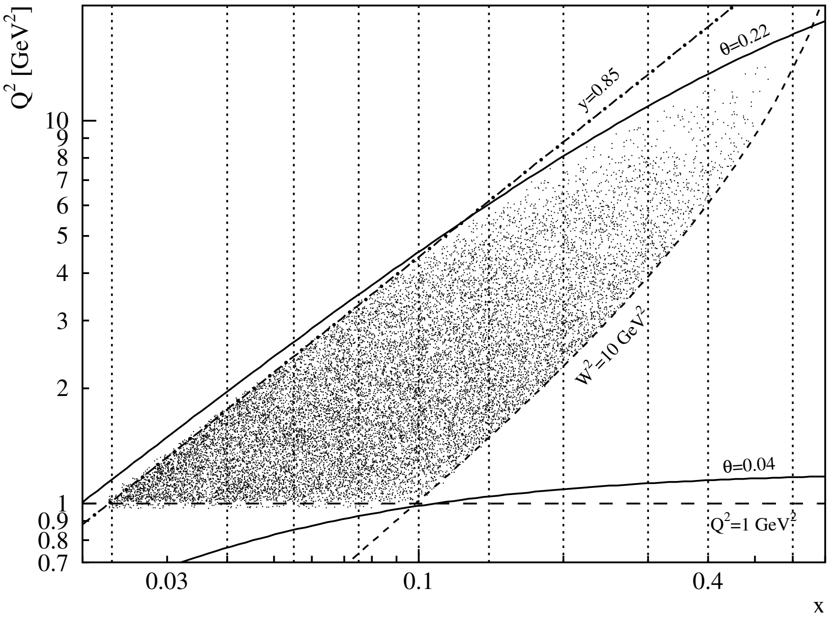

Figure 5.1: The distribution of the selected DIS events

Positron-Hadron Separation

The positron-hadron separation is performed based on the combined information from the calorimeter, the hodoscopes and the TRD as well as the RICH detector. For this purpose, a likelihood called $\mathrm{PID}_{\mathrm{det}}$ is defined for each detector as

$$\mathrm{PID}_{\mathrm{det}} = \log_{10} \frac{\mathcal{P}_{det}^{e^+}}{\mathcal{P}_{det}^{h}}, \tag{5.1}$$

where $\mathcal{P}_{det}^{e^+(h)}$ represents the conditional probability that a signal from the detector is due to positron (hadron). The quantity can be related to the particle flux ϕ:

$$\mathcal{P}_{det}^{e^+(h)} = \frac{\phi^{e^+(h)} \cdot \mathcal{L}_{det}^{e^+(h)}}{\phi^{e^+} \cdot \mathcal{L}_{det}^{e^+} + \phi^h \cdot \mathcal{L}_{det}^h}, \tag{5.2}$$

where $\mathcal{L}_{det}^{e^+(h)}$ is the probability that the positron (hadron) gives a signal in the detector. Then Eq. (5.1) is rewritten as

$$\mathrm{PID}_{\mathrm{det}} = \log_{10} \frac{\mathcal{L}_{det}^{e^+}}{\mathcal{L}_{det}^h} + \log_{10} \frac{\phi^{e^+}}{\phi^h}. \tag{5.3}$$

Various combinations of the PID_{det} are defined as

$$\begin{aligned}
\mathrm{PID}_3 &= \mathrm{PID}_{cal} + \mathrm{PID}_{Pre} + \mathrm{PID}_{RICH} && (5.4)\\
&= \log_{10} \frac{\mathcal{L}_{RICH}^{e^+} \cdot \mathcal{L}_{Cal}^{e^+} \cdot \mathcal{L}_{Pre}^{e^+}}{\mathcal{L}_{RICH}^h \cdot \mathcal{L}_{Cal}^h \cdot \mathcal{L}_{Pre}^h} + \log_{10} \frac{\phi_{RICH}^{e^+} \cdot \mathcal{L}_{Cal}^{e^+} \cdot \phi_{Pre}^{e^+}}{\phi_{RICH}^h \cdot \mathcal{L}_{Cal}^h \cdot \phi_{Pre}^h}, && (5.5)\\
\mathrm{PID}_5 &= \mathrm{PID}_{TRD} && (5.6)\\
&= \log_{10} \frac{\prod_{m=1}^6 \mathcal{L}_{TRD_m}^{e^+}}{\prod_{m=1}^6 \mathcal{L}_{TRD_m}^h} + \log_{10} \frac{\prod_{m=1}^6 \phi_{TRD_m}^{e^+}}{\prod_{m=1}^6 \phi_{TRD_m}^h}, && (5.7)
\end{aligned}$$

where the sum for the TRD runs over the six modules. A quantity PID is defined by subtracting the flux ratio Φ from the sum of PID_3 and PID_5:

$$\mathrm{PID} = \mathrm{PID}_3 + \mathrm{PID}_5 - \log_{10} \Phi. \tag{5.8}$$

The distribution of the PID is shown in Figure 5.2. As can be seen in the plot, positrons and hadrons are clearly separated. Positrons are identified with efficiencies larger than 98 % and contaminations below 1.0 %. Hadrons with efficiencies larger than 99 % and contaminations below 0.1 % by using the following requirements:

$$\begin{array}{ll} \mathrm{PID} > 1 & \text{for positron,} \\ \mathrm{PID} < 0 & \text{for hadron.} \end{array} \tag{5.9}$$

Cuts on Semi-inclusive DIS Events

The HERMES RICH can identify pions, kaons and protons in the momentum range of 2 - 15 GeV/c. To select hadrons in coincidence with the DIS positron,

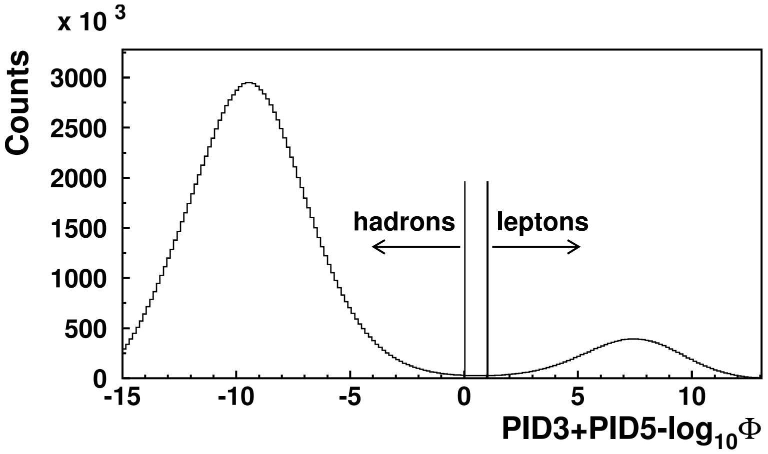

Figure 5.2: The distribution of the PID. The left and right peaks are due to hadrons and positrons, respectively.

cuts on the Feynman variable of $0.1 \le x_F \le 1.0$ and the fractional energy of the hadron of $0.2 \le z \le 0.8$ were applied. Hadrons produced from the target remnant are suppressed by the lower limits of theses cuts. The upper limit on z allows to reject backgrounds from events such as exclusive processes.

The numbers of the DIS events and the SIDIS hadrons are summarized in Table 5.2 after applying all the inclusive and semi-inclusive DIS cuts.

5.4 The Measured Asymmetries

The most interesting asymmetry is the double spin asymmetry A_1 which is the cross section asymmetry for parallel and anti-parallel alignment of the virtual photon and target spin:

$$A_1^h(x,Q^2) \overset{g_2=0}{\simeq} \frac{g_1(x,Q^2)}{F_1(x,Q^2)} = \frac{\sum_f e_f^2 \Delta q_f(x,Q^2) \int dz D_f^h(z,Q^2)}{\sum_f e_f^2 q_f(x,Q^2) \int dz D_f^h(z,Q^2)}. \tag{5.10}$$

However experimentally accessible asymmetry is the longitudinal double spin asymmetry $A_{||}$ defined as the cross section asymmetry for parallel and anti-parallel alignment of the beam and target spin. The asymmetry $A_{||}$ can be related to A_1 as

$$A_1^h(x,Q^2) = \frac{A_{||}^h(x,Q^2)}{D(1+\eta\gamma)}. \tag{5.11}$$

Proton Target						
	1996		1997			
	$N^{\overset{\rightarrow}{\Rightarrow}}$	$N^{\overset{\rightarrow}{\Leftarrow}}$	$N^{\overset{\rightarrow}{\Rightarrow}}$	$N^{\overset{\rightarrow}{\Leftarrow}}$		
DIS $e^{\pm}$	239506	256799	621752	673590		
h^{+}	37938	41249	97807	107679		
h^{-}	22165	23740	57272	60666		
π^{+}	15370	16712	41081	45200		
π^{-}	10969	11653	29374	30883		
K^{+}						
K^{-}						

Deuterium Target						
	1998		1999		2000	
	$N^{\overset{\rightarrow}{\Rightarrow}}$	$N^{\overset{\rightarrow}{\Leftarrow}}$	$N^{\overset{\rightarrow}{\Rightarrow}}$	$N^{\overset{\rightarrow}{\Leftarrow}}$	$N^{\overset{\rightarrow}{\Rightarrow}}$	$N^{\overset{\rightarrow}{\Leftarrow}}$
DIS $e^{\pm}$	420841	422793	456418	469372	2439348	2521873
h^{+}	61314	61751	66100	67438	372849	385427
h^{-}	40669	39730	43924	44756	246931	253671
π^{+}	30393	30207	32350	33018	179264	184678
π^{-}	24546	24055	26283	26531	144685	148092
K^{+}	5938	6186	6617	6897	36514	38371
K^{-}	2471	2350	2755	2753	15224	15442

Table 5.2: Summary of the number of the DIS events and the SIDIS hadrons. The data are shown for each spin state ($N^{\overset{\rightarrow}{\Rightarrow}}$: The beam and the target spins are parallel. $N^{\overset{\rightarrow}{\Leftarrow}}$: The beam and the target spins are anti-parallel).

The parameterization of the ratio of the photo-absorption cross section $R = \frac{\sigma_L}{\sigma_T}$ to the world data [29] was used to calculate D (see Figure 2.39). $A_{||}$ is related to the measured experimental asymmetry $A_{||}^{\mathrm{exp}}$ which accounts for the beam (P_B) and target polarization (P_T) and the target dilution factor f_D:

$$A_{||}^h(x, Q^2) = \frac{1}{P_B P_T f_D} \cdot A_{||}^{\mathrm{exp}(h)}(x, Q^2). \tag{5.12}$$

The dilution factor f_D represents the fraction of nucleons in the target which are polarized. It depends on the target type: 1 for proton and 0.925 for deuterium as will be described in Section 6.1. In addition to the dilution factor, the asymmetry is reduced by the incompletion of beam and target polarization. For instance, when the beam polarization is 50 % in both measurements of the cross section $\sigma^{\overset{\rightarrow}{\Leftarrow}}$ and $\sigma^{\overset{\rightarrow}{\Rightarrow}}$, the asymmetry is observed with a half size of the real value. The reason is following. The polarization of $P_B = 50\%$ represents that 75% of the beam is polarized in the correct direction and the rest of the beam is polarized in the opposite direction. Therefore the measured cross section $\sigma_{exp}^{\overset{\rightarrow}{\Leftarrow}}$ is contributed from both the cross section $\sigma^{\overset{\rightarrow}{\Leftarrow}}$ and $\sigma^{\overset{\rightarrow}{\Rightarrow}}$ at shares of 75 and 25 percents. Similarly in the case of parallel alignments of the beam and target polarization, the equation $\sigma_{exp}^{\overset{\rightarrow}{\Rightarrow}} = 0.75\sigma^{\overset{\rightarrow}{\Rightarrow}} + 0.25\sigma^{\overset{\rightarrow}{\Leftarrow}}$ can be made. Hence the cross section difference (numerator of the asymmetry) is reduced to 50 %, while the sum of the cross section (denominator of the asymmetry) is not affected.

The asymmetry $A_{||}^h$ can be obtained by

$$\begin{aligned} A_{||}^h &= \frac{1}{P_B P_T f_D} \cdot \frac{\frac{N_h^{\overset{\rightarrow}{\Leftarrow}}}{L^{\overset{\rightarrow}{\Leftarrow}}} - \frac{N_h^{\overset{\rightarrow}{\Rightarrow}}}{L^{\overset{\rightarrow}{\Rightarrow}}}}{\frac{N_h^{\overset{\rightarrow}{\Leftarrow}}}{L^{\overset{\rightarrow}{\Leftarrow}}} + \frac{N_h^{\overset{\rightarrow}{\Rightarrow}}}{L^{\overset{\rightarrow}{\Rightarrow}}}}, & (5.13) \\ &\equiv \frac{1}{f_D} \cdot \frac{N_h^{\overset{\rightarrow}{\Leftarrow}} L^{\overset{\rightarrow}{\Rightarrow}} - N_h^{\overset{\rightarrow}{\Rightarrow}} L^{\overset{\rightarrow}{\Leftarrow}}}{N_h^{\overset{\rightarrow}{\Leftarrow}} L_{PB}^{\overset{\rightarrow}{\Rightarrow}} + N_h^{\overset{\rightarrow}{\Rightarrow}} L_{PB}^{\overset{\rightarrow}{\Leftarrow}}}, & (5.14) \end{aligned}$$

where

$$\begin{aligned} N_h^{\overset{\rightarrow}{\Leftarrow}(\overset{\rightarrow}{\Rightarrow})} &\equiv \sum_i (n_i^h)^{\overset{\rightarrow}{\Leftarrow}(\overset{\rightarrow}{\Rightarrow})}, & (5.15) \\ L^{\overset{\rightarrow}{\Leftarrow}(\overset{\rightarrow}{\Rightarrow})} &\equiv \sum_i L_i^{\overset{\rightarrow}{\Leftarrow}(\overset{\rightarrow}{\Rightarrow})}, & (5.16) \\ L_{PB}^{\overset{\rightarrow}{\Leftarrow}(\overset{\rightarrow}{\Rightarrow})} &\equiv \sum_i (L_{PB})_i^{\overset{\rightarrow}{\Leftarrow}(\overset{\rightarrow}{\Rightarrow})}. & (5.17) \end{aligned}$$

Here the sum loops over all the good usable bursts, n_i^h is the number of events for the production of hadron h, and L_i and L_{PB} represent the integrating luminosity and the $P_B P_T$ weighted integrating luminosity respectively:

$$
\begin{aligned}
L_i^{\overset{\rightarrow}{\Leftarrow}(\overset{\rightarrow}{\Rightarrow})} &= \int dt \mathcal{L}^{\overset{\rightarrow}{\Leftarrow}(\overset{\rightarrow}{\Rightarrow})}(t), && (5.18)\\
(L_{PB})_i^{\overset{\rightarrow}{\Leftarrow}(\overset{\rightarrow}{\Rightarrow})} &= \int dt \mathcal{L}^{\overset{\rightarrow}{\Leftarrow}(\overset{\rightarrow}{\Rightarrow})}(t) P_B(t) P_T(t), && (5.19)
\end{aligned}
$$

where the integral goes over the time length of a burst i, and $\mathcal{L}$, $P_B(t)$ and $P_T(t)$ are the time dependent luminosity, beam and target polarization respectively. In the Bjørken limit, the photo-absorption asymmetry A_1 depends only on x. In the HERMES kinematic region of $0.03 < x < 0.6$ and $1.0 < Q^2 < 15.0$, the polarized structure function (Figure 2.6) is independent of Q^2 or has weak dependence of Q^2 as well as the unpolarized structure function F_1 (Figure 2.2). Therefore the measurements of the asymmetry $A_{||}$ were performed in each x bin defined in Table 5.3:

$$
A_1^h(x, Q^2) \overset{g_2=0}{\simeq} \frac{g_1(x, Q^2)}{F_1(x, Q^2)} \longrightarrow A_1^h(x). \qquad (5.20)
$$

Bin number	Range	average value of x
1	0.023 - 0.040	0.033
2	0.040 - 0.055	0.047
3	0.055 - 0.075	0.065
4	0.075 - 0.100	0.087
5	0.100 - 0.140	0.119
6	0.140 - 0.200	0.168
7	0.200 - 0.300	0.245
8	0.300 - 0.400	0.342
9	0.400 - 0.600	0.466

Table 5.3: Definition of the binning in x.

The HERMES experiment has been operated with the polarized proton target for 1996 and 1997 data taking periods. In the periods, the threshold Čerenkov detector was used for the hadron-positron separation and the identification of pions. From the year 1998 to 2000, deuterium target has been used. In the Spring of 1998, the threshold Čerenkov detector was replaced by the RICH detector. It enables us to identify kaons in addition to pions.

5.4.1 Correction of Yields

Before calculating the asymmetry $A_{||}$, the count rate N was corrected. The purpose is to remove the background such as e^+e^- pair production which could be misidentified as the DIS events and take into account the RICH misidentification.

Background Correction

The count rate for the DIS events was corrected for background processes such as e^+e^- pair production. Generally the e^+e^- pair is generated via a decay mode of $\pi^0 \to 2\gamma, \gamma \to e^+e^-$. Another contribution comes from high energy bremsstrahlung photons. Similarly the photon is converted an e^+e^- pair. If the leading lepton is a positron, it is not possible to identify the background process. However, under the assumption that detection efficiencies is equal for both charges, twice the number of events, where the leading lepton is an electron, were subtracted from the sample of DIS events. The count rate for hadrons were also corrected in the same manner.

Hadron Yield Unfolding

The hadron yield was corrected by inverse P-matrix which accounts for the identification efficiency of the RICH detector. The inverse P-matrix is a function of the particle momentum and the number of tracks in the event. The measured hadron yield $N_{meas}(x, p)$ can be unfolded with the inverse P-matrix to hadron yield $N^h(x)$:

$$N^h(x) = \sum_{k=\pi,K,p} \sum_{n=1}^{3} \sum_{i} \left[(P_n^{-1})_k^h \right]_i \left[N_{meas}^k(x, p_i) \right]_n \tag{5.21}$$

where $(P_n^{-1})_k^h$ represents the element of the inverse P-matrix for n track event and the second and last sum run over the number of tracks and all the momentum bin defined in Table 5.4. The inverse P-matrices for one, two and three tracks are shown in Figure 5.3 - 5.5.

5.5 Extraction of Born Asymmetries

The measured asymmetries $A_{||}^h$ were corrected for higher order QED effects and acceptance effects. The corrected asymmetries can be used to determine the asymmetries A_1, Born asymmetries.

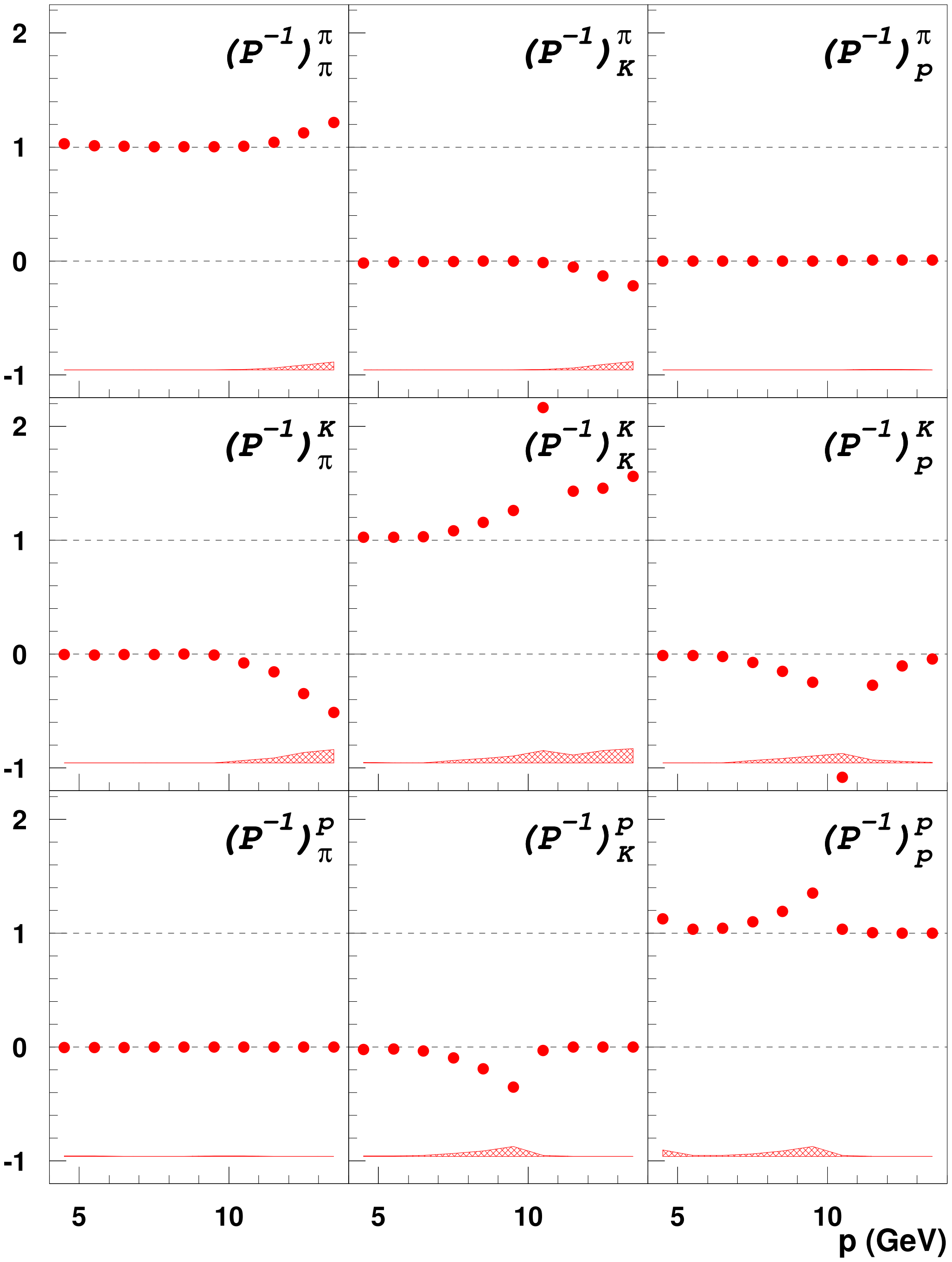

Figure 5.3: Inverse P-matrix for 1 track per a detector half.

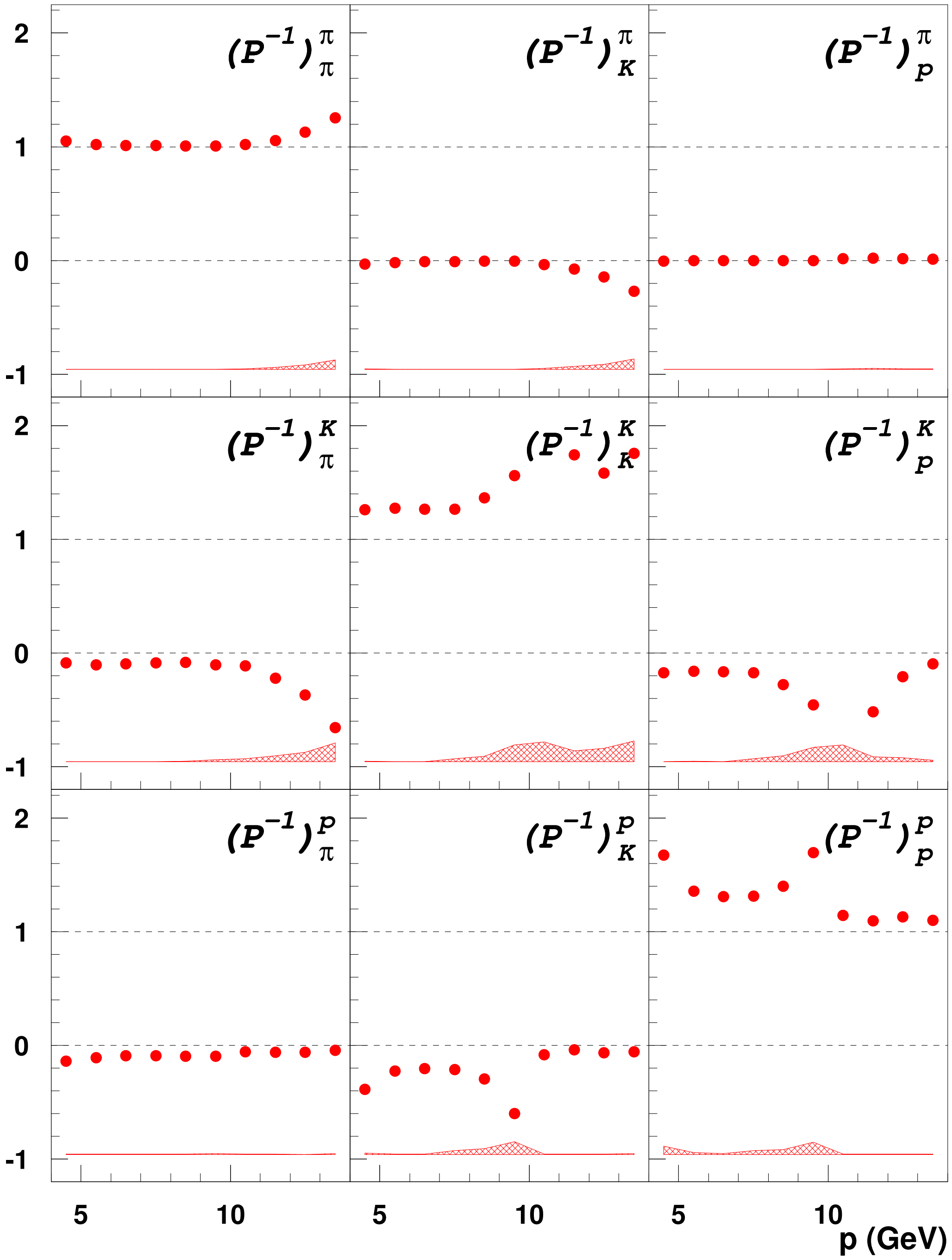

Figure 5.4: Inverse P-matrix for 2 track per a detector half.

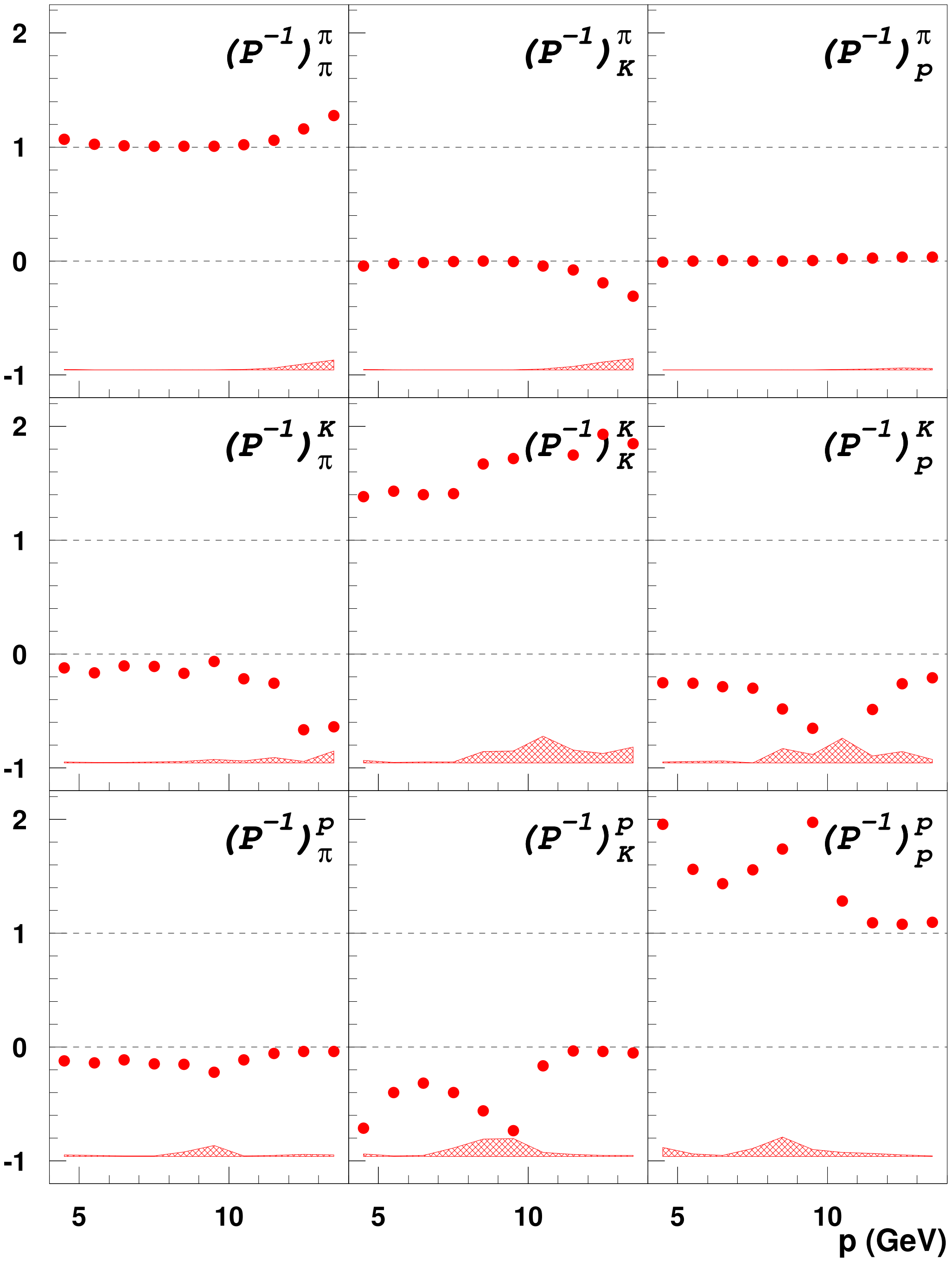

Figure 5.5: Inverse P-matrix for 3 track per a detector half.

Bin	1	2	3	4	5	6	7	8	9	10
p_{low} [GeV]	4.0	5.0	6.0	7.0	8.0	9.0	10.0	11.0	12.0	13.0
p_{up} [GeV]	5.0	6.0	7.0	8.0	9.0	10.0	11.0	12.0	13.0	14.0

Table 5.4: Definition of the binning in momentum p.

5.5.1 Azimuthal Acceptance Correction

The measurements of the asymmetry $A_{||}$ was performed by integrating over the azimuthal angle ϕ. However the polarized and unpolarized semi-inclusive cross section depends on the azimuthal acceptance since partons have non-zero intrinsic transverse momenta. Hence the asymmetry $A_{||}$ was corrected for the azimuthal acceptance effect as [76, 77]:

$$A_{||}^h = C_\phi^h (A_{||}^h)_{meas}, \tag{5.22}$$

where

$$C_\phi^h(x) = 1 + \Big(\log_{10}(x) - \log_{10}(x_0^h)\Big) \left[a_0^h + \sum_{i=1}^{3} a_i^h \log_{10}^i(x) \right]. \tag{5.23}$$

The values of the coefficients used in the above equation are given in Table 5.5.

5.5.2 Smearing Correction and QED Radiative Correction

The interaction between the particles and the detector materials such as multiple-scattering in the detector may affect the kinematic quantities of the particles. Additionally the misalignment of the detector and imperfection of calibrations lead to systematic bias to true kinematics of the particles. These detector effects were simulated by using HERMES Monte Carlo (HMC) based on GEANT program [78] which takes the HERMES detector acceptance into account.

As mentioned in Section 2.3, the DIS process is described by one photon exchange. However contributions from higher order processes are included in the sample of the DIS events. For example, Bremsstrahlung photons can be emitted by the incoming and the scattered positron in Next-to-Leading Order (NLO). To correct for these radiative effects, the Monte Carlo generator RADGEN [79] based on POLARD [80, 81] which allows to calculate the radiative corrections to the polarized DIS cross section was used in the HMC.

Azimuthal acceptance correction for the proton asymmetries

	x_0^h	a_0^h	a_1^h	a_2^h	a_3^h
h^+	-1.65	-0.052	-0.180	-0.580	-0.500
h^-	-1.65	-0.041	-0.246	-0.662	-0.486
π^+	-1.65	-0.048	-0.233	-0.617	-0.464
π^-	-1.65	-0.038	-0.212	-0.559	-0.408

Azimuthal acceptance correction for the deuteron asymmetries

	x_0^h	a_0^h	a_1^h	a_2^h	a_3^h
h^+	-1.65	-0.080	-0.318	-0.879	-0.667
h^-	-1.65	-0.064	-0.358	-0.889	-0.634
π^+	-1.65	-0.091	-0.466	-1.145	-0.785
π^-	-1.65	-0.075	-0.440	-1.055	-0.718
K^+	-1.65	-0.041	-0.042	-0.282	-0.317
K^-	-1.65	-0.034	-0.083	-0.322	-0.312

Table 5.5: Coefficients of the parameterization of the azimuthal acceptance correction.

5.6 Uncertainty on the Asymmetries

5.6.1 Statistical Uncertainties

Under the assumption that the number of events follows a Poisson distribution for both spin states, the statistical uncertainty on the semi-inclusive asymmetry A_1^h can be given by

$$\begin{aligned}\delta A_1^h &= \sqrt{\left(\frac{\partial A_1}{\partial N_h^{\overset{\rightarrow}{\Leftarrow}}}\delta N_h^{\overset{\rightarrow}{\Leftarrow}}\right)^2 + \left(\frac{\partial A_1}{\partial N_h^{\overset{\rightarrow}{\Rightarrow}}}\delta N_h^{\overset{\rightarrow}{\Rightarrow}}\right)^2} \\ &= \frac{1}{1+\eta\gamma}\frac{L^{\overset{\rightarrow}{\Leftarrow}}L_{PB}^{\overset{\rightarrow}{\Rightarrow}}D^{\overset{\rightarrow}{\Rightarrow}} + L^{\overset{\rightarrow}{\Rightarrow}}L_{PB}^{\overset{\rightarrow}{\Leftarrow}}D^{\overset{\rightarrow}{\Leftarrow}}}{(N^{\overset{\rightarrow}{\Leftarrow}}L_{PB}^{\overset{\rightarrow}{\Rightarrow}}D^{\overset{\rightarrow}{\Rightarrow}} + N^{\overset{\rightarrow}{\Rightarrow}}L_{PB}^{\overset{\rightarrow}{\Leftarrow}}D^{\overset{\rightarrow}{\Leftarrow}})^2}\sqrt{(N^{\overset{\rightarrow}{\Rightarrow}})^2N^{\overset{\rightarrow}{\Leftarrow}} + (N^{\overset{\rightarrow}{\Leftarrow}})^2N^{\overset{\rightarrow}{\Rightarrow}}}.\end{aligned} \tag{5.24}$$

5.6.2 Systematic Uncertainties on the Asymmetries

The systematic uncertainties on the asymmetries are contributed from the uncertainty on the beam and target polarization, assuming $g_2 = 0$, the uncertainty on R

and the RICH systematic uncertainties.

Beam and Target Polarization Uncertainties

The measurements of the beam polarization was performed by Transverse Polarimeter during the 1996 to 1998 data taking periods, while the Longitudinal Polarimeter is mainly used for the measurements since 1999. The fractional uncertainties $\left[\frac{\delta P_B}{P_B}\right]_{1996-1998}$ for 1996 to 1998 data taking periods, $\left[\frac{\delta P_B}{P_B}\right]_{1999}$ for the year 1999 and $\left[\frac{\delta P_B}{P_B}\right]_{2000}$ for the year 2000 are 3.4 %, 1.8 % and 1.9 % respectively. The systematic uncertainty on A_1 due to the uncertainty of the beam polarization is calculated as

$$[\delta A_1]_{P_B} = |A_1 \cdot \frac{\delta P_B}{P_B}|. \tag{5.25}$$

The contribution of the uncertainty on the target polarization to the asymmetry can be evaluated as

$$[\delta A_1]_{P_T} = |A_1 \cdot \frac{\delta P_T}{P_T}|. \tag{5.26}$$

The target polarization for the 1997 and 2000 data sets are known with better precision with respect to the other data taking periods for the same target. In order to reduce the systematic uncertainty for the 1996, 1998 and 1999 data taking periods, normalizations of the inclusive asymmetry were performed. The procedure is following. In the first step, the inclusive asymmetry $\tilde{A}_1$is calculated with the fixed valued of $P_T = 1$. In the second step, the asymmetry is normalized by a factor $\frac{1}{P_T^{new}}$ and calculated χ^2 defined as

$$\chi^2 = \sum_i \frac{\left[\frac{1}{P_T^{new} \cdot \tilde{A}_1(x_i) - A_1^{ref}(x_i)}\right]^2}{\left[\frac{1}{P_T^{new} \cdot \delta\tilde{A}_1(x_i)}\right]^2 + (\delta A_1^{ref}(x_i))^2}, \tag{5.27}$$

where A_1^{ref} is the corresponding asymmetry from a reference data set (When $\tilde{A}_1(x)$ is the asymmetry for the year 1996, A_1^{ref} is the asymmetry for the year 1997. When $\tilde{A}_1(x)$ is the asymmetry for 1998 or 1999 data taking periods, A_1^{ref} is the asymmetry for the year 2000), $\delta\tilde{A}_1$ and δA_1^{ref} are the statistical uncertainties on $\tilde{A}_1$ and A_1^{ref} respectively and the sum loops over all the x bins. P_T^{new} for the smallest value of χ^2 is taken as the target polarization for the data taking period. The resulting systematic uncertainty on the target polarization can be obtained by

$$\delta P_T^{new} = \sqrt{(\delta P_T)^2 + (\delta P_T^{ref})}, \tag{5.28}$$

where δP_T is determined as a difference of polarization between the χ^2 minimum and where χ^2 increases by 1 and δP_T^{ref} is the systematic uncertainty of the target polarization for the reference asymmetry. Thus the systematic uncertainties of the target polarization were reduced from 7.6 % to 5.5 %, 8.0 % to 7.5 % and 8.0 % to 7.0 % for the 1996, 1998 and 1999 data sets respectively. The fractional uncertainty of the beam and target polarizations are listed in the Table 3.1.

Assumption related to g_2

The systematic uncertainty on A_1 due to the assumption of $g_2 = 0$ was estimated. A parameterization of the experimental data g_2 from the fixed target experiments at SLAC, CERN and DESY is available (see Figure 2.5):

$$g_2^p = \pm 0.035 x^{-1}(1-x)^{0.7}, \tag{5.29}$$

$$g_2^d = \pm 0.015 x^{-1}(1-x)^{0.9}. \tag{5.30}$$

The systematic uncertainty due to the assumption $g_2 = 0$ is given by

$$[\delta A_1]_{g_2} = \frac{\eta\gamma(1+\gamma^2)}{1+\eta\gamma} \cdot \left|\frac{g_2}{F_1}\right|. \tag{5.31}$$

The Cross Section Ratio R

The systematic uncertainty δR contributes to the systematic uncertainty on the asymmetry A_1 as

$$[\delta A_1]_R = |A_1 \cdot \frac{\varepsilon}{1+\varepsilon R} \cdot \delta R|. \tag{5.32}$$

Azimuthal acceptance correction

The contribution from the azimuthal acceptance correction to the systematic uncertainties on A_1 is calculated by

$$[\delta A_1]_{acc} = |A_1 \cdot \delta C_\phi^h|, \tag{5.33}$$

where the uncertainty of the correction factor C_ϕ^h is estimated to be 2 % [77].

Contributions related to RICH Systematic Uncertainties

The systematic uncertainty due to the RICH systematic uncertainties described in Section 4.3.1 was estimated. The systematic uncertainties on the P-matrix arise from imperfection of RICH description in HMC. The systematic uncertainty on A_1 from this contribution was calculated as

$$[\delta A_1]_{RICH} = \frac{1}{\sqrt{3}} \left| \frac{1}{2} \left(A_1(P + [\Delta P]_{MC}) - A_1(P) \right) \right|, \tag{5.34}$$

where P and $[\Delta P]_{MC}$ represent the P-matrix and the systematic uncertainty due to the imperfection in HMC and $A_1(P)$ shows the asymmetry obtained by using the P-matrix P. It is assumed that the asymmetry A_1 could be biased in the region from $A_1(P)$ to $A_1(P + [\Delta P]_{MC})$ with the same probability. The factor $\frac{1}{\sqrt{3}}$ is due to the standard deviation of the uniform distribution.

Total Systematic Uncertainty on the asymmetries

The total systematic uncertainty on the asymmetries is calculated by adding in quadrature all the contributions described above

$$\delta A_1^{tot} = \sqrt{\sum_i [\delta A]_i^2}. \tag{5.35}$$

The fractional systematic uncertainties on A_1 are summarized in Table 5.6

Contribution	Proton Target	Deuterium Target
Beam polarization	4.2%	2.3%
Target polarization	5.1%	5.2%
Azimuthal acceptance (SIDIS)	3.0%	3.1%
Radiative correction (DIS)	2.0%	2.0%
Radiative correction (SIDIS)	1.0%	1.0%
Smearing correction	2.0%	2.0%
R	1.1%	1.1%
g_2	0.6%	1.4%

Table 5.6: The fractional systematic uncertainties on A_1 averaged over x.

5.7 Results

The double spin asymmetries for the proton and deuteron target are shown in Figure 5.6 and Figure 5.7. The values are listed in Table A.12 and A.13. The results are compared with ones measured by SMC [49]. One can see that they are in good agreement within the errors. Since the asymmetries by both the experiment were measured in different Q^2 region ($\sim$2.5 GeV^2 for HERMES, $\sim$10 GeV^2 for SMC), one can confirm the asymmetries are independent of Q^2.

For the proton target all the asymmetries monotonously increase with x. The positive values of the positive pion asymmetry imply that the contribution from u quark to the nucleon spin is also positive since the positive pion is generated by u quark with high probability.

The systematic uncertainties from the RICH contribution are not small enough to neglect. However the RICH study is still ongoing, and an effort has been devoted to describe the RICH performance in HMC with better precision. Furthermore LUND parameters which account for the fragmentation process of quarks into hadrons, is being tuned to match the hadron multiplicities measured at the HERMES experiment. Hence it could be expected to have the systematic errors on P-matrix smaller, as the result, the systematic uncertainty on A_1 due to the RICH systematic uncertainty will be improved.

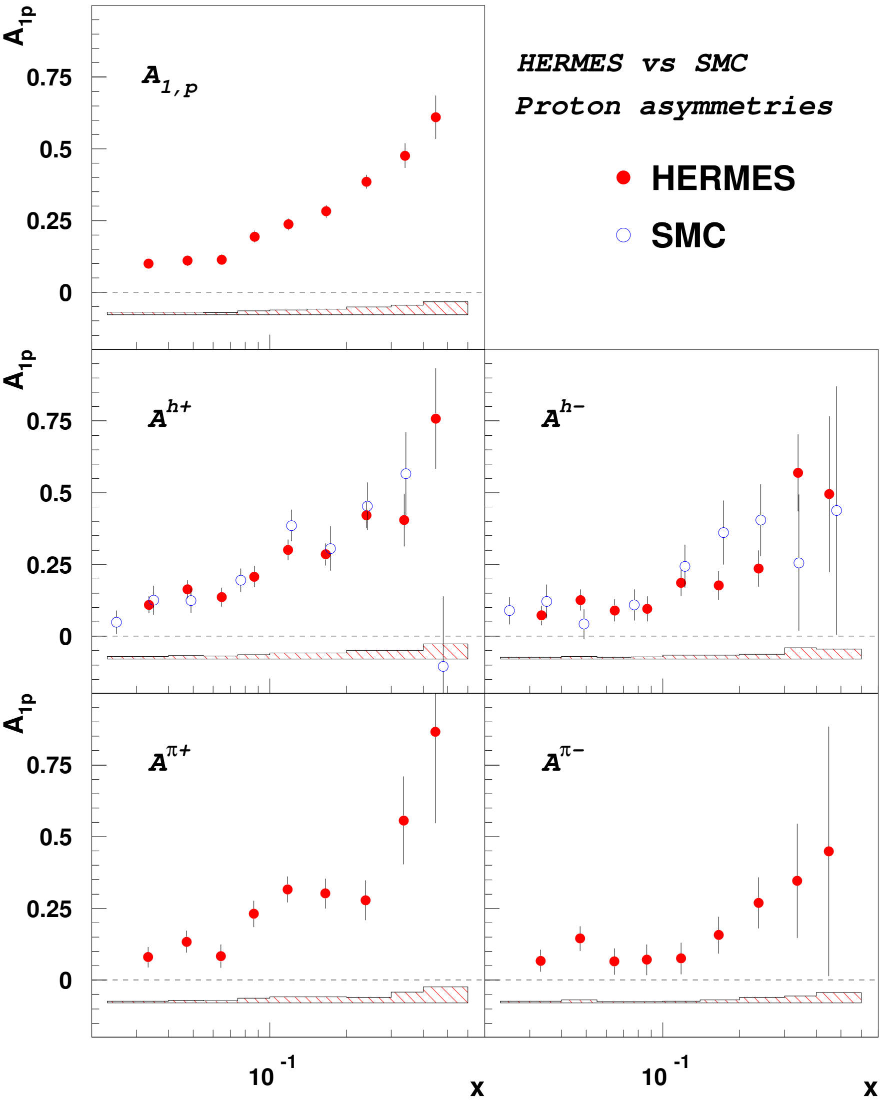

Figure 5.6: The inclusive and semi-inclusive asymmetries for the proton target. The HERMES results are compared with the SMC ones which are indicated as the closed and open circle respectively. The error bars show the statistical uncertainties and the error bands are the total systematic uncertainty for the HERMES data.

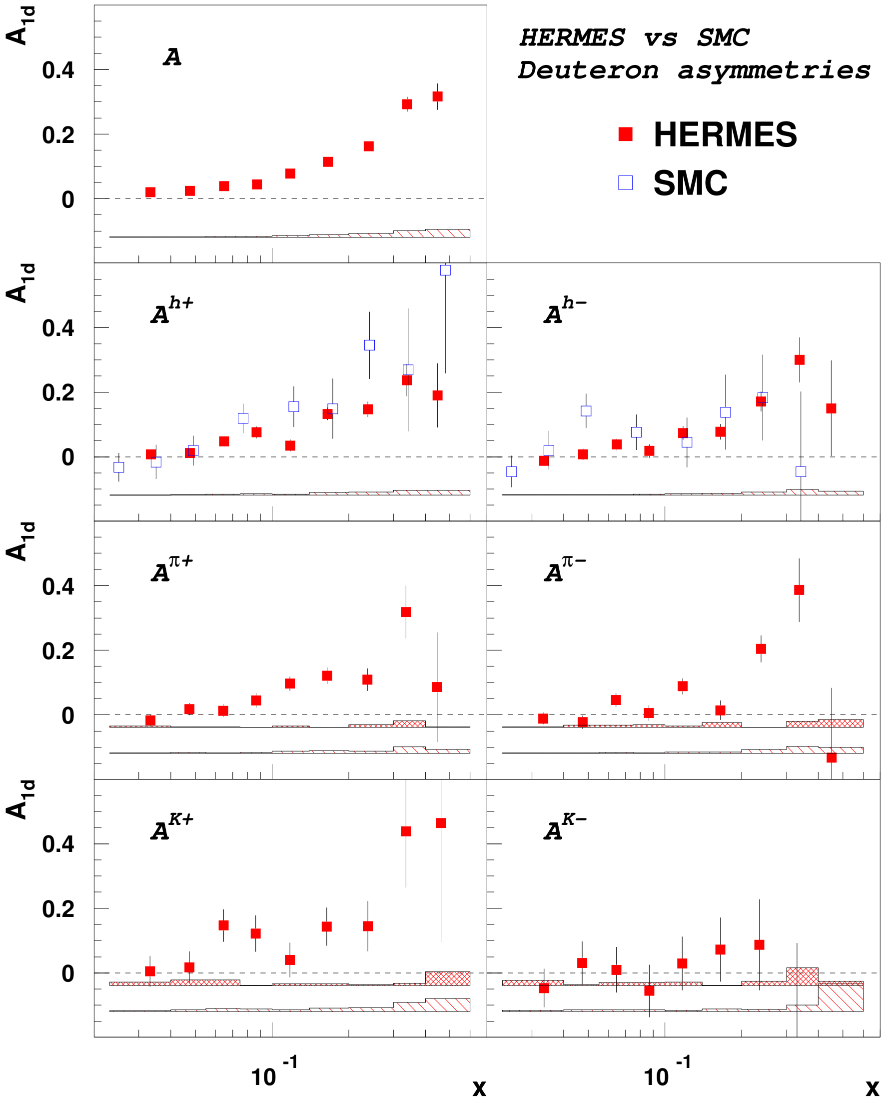

Figure 5.7: The inclusive and semi-inclusive asymmetries for the deuteron target. The closed and open squares are the results from HERMES and SMC. The upper error bands show the systematic uncertainties due to the RICH systematic uncertainties. The lower ones correspond to the total systematic uncertainties except the RICH contribution.

Chapter 6

Quark Helicity Distributions

In this chapter the quark helicity distributions are determined by using the asymmetries A_1 described in the previous chapter. Effects of the systematic uncertainty on the unpolarized PDF are estimated. Finally the results are compared with ones by the other experiments.

6.1 Formalism of Helicity Distribution Extraction

The measured double spin asymmetry is related to the polarized parton distributions as

$$A_1^h(x) = \frac{\int\int dQ^2 dz g_1^h}{\int\int dQ^2 dz F_1^h} = \frac{\sum_f e_f^2 \int dQ^2 \Delta q_f(x,Q^2) \int dz \tilde{D}_f^h(x,Q^2,z)}{\sum_{f'} e_{f'}^2 \int dQ^2 q_{f'}(x,Q^2) \int dz \tilde{D}_{f'}^h(x,Q^2,z)}, \tag{6.1}$$

where $\tilde{D}$ represents effective fragmentation functions which take the HERMES acceptance into account. This equation can be rewritten as

$$\begin{aligned} A_1^h(x) &= \sum_f \frac{e_f^2 \int dQ^2 q_f(x,Q^2) \int dz \tilde{D}_f^h(x,Q^2,z)}{\sum_{f'} e_{f'}^2 \int dQ^2 q_{f'}(x,Q^2) \int dz \tilde{D}_{f'}^h(x,Q^2,z)} \cdot \frac{\int dQ^2 \Delta q(x,Q^2)}{\int dQ^2 q(x,Q^2)} \\ &\equiv P_f^h(x) \cdot \frac{\Delta q_f}{q_f}(x), \end{aligned} \tag{6.2}$$

where $P_f^h(x)$ can be interpreted as the probability that the hadron originated from scattering off a quark of flavor f, when a hadron h is detected in the DIS event:

$$P_f^h(x) = \sum_f \frac{\int dQ^2 e_f^2 q_f(x,Q^2) \int dz \tilde{D}_f^h(x,Q^2,z)}{\sum_{f'} \int dQ^2 e_{f'}^2 q_{f'}(x,Q^2) \int dz \tilde{D}_{f'}^h(x,Q^2,z)}. \tag{6.3}$$

This quantity is called 'purity'. All the measured inclusive and semi-inclusive asymmetries form the vector as

$$\vec{\boldsymbol{A}}(x) = \mathcal{P}(x) \cdot \vec{\boldsymbol{Q}}(x), \tag{6.4}$$

where

$$\vec{\boldsymbol{A}} = \begin{pmatrix} A_1^{h_1}(x_i) \\ \vdots \\ A_1^{h_m}(x_i) \end{pmatrix}, \quad \vec{\boldsymbol{Q}} = \begin{pmatrix} \Delta q_{f_1}/q_{f_1}(x_i) \\ \vdots \\ \Delta q_{f_n}/q_{f_n}(x_i) \end{pmatrix}, \tag{6.5}$$

$$\mathcal{P} = \begin{pmatrix} P_{f_1}^{h_1}(x_i) & \dots & P_{f_m}^{h_1}(x_i) \\ \vdots & \ddots & \vdots \\ P_{f_1}^{h_m}(x_i) & \dots & P_{f_n}^{h_m}(x_i) \end{pmatrix}. \tag{6.6}$$

It must be noted that the above equation holds for the proton. For the neutron, the corresponding equation can be derived using isospin rotation between proton and neutron.

$$\begin{aligned} \vec{\boldsymbol{A}}_n(x) &= \mathcal{P}_n(x) \cdot \vec{\boldsymbol{Q}}_n(x), && (6.7) \\ &= \mathcal{P}'_n(x) \cdot \vec{\boldsymbol{Q}}(x), && (6.8) \end{aligned}$$

where the subscripts n stands for the quantity for the neutron, $\mathcal{P}'_n$ represents isospin rotated purities for the neutron and the isospin rotated vector of $\vec{\boldsymbol{Q}}_n$ corresponds $\vec{\boldsymbol{Q}}$. Under the assumption that Fermi motion and shadowing effects are negligible, the spin asymmetries for the deuteron can be related to that for proton and neutron as

$$\vec{\boldsymbol{A}}_d(x) = f_{pd}(x) p_{pd} \vec{\boldsymbol{A}}_p(x) + f_{nd}(x) p_{nd} \vec{\boldsymbol{A}}_n(x), \tag{6.9}$$

where f_{pd} and f_{nd} are dilution factors which take account for the probability that the incoming positron is scattered off a proton and a neutron inside a deuteron respectively. The dilution factors is given by

$$\begin{aligned} f_{pd} = \frac{\sigma_p}{\sigma_d} = \frac{n_p}{n_d} \cdot \frac{F_{2,p}}{2F_{2,d}}, && (6.10) \\ f_{nd} = 1 - f_{pd}, && (6.11) \end{aligned}$$

where σ_p (σ_d) is the unpolarized DIS cross sections for the proton (deuteron) target and n_p (n_d) represents the hadron multiplicities on the proton (deuteron). The factors p_{pd} and p_{nd} represent effective polarizations of the proton and the neutron in the deuteron, respectively. They are reduced by the effect of the deuteron D-state as

$$p_{pd} = p_{nd} = 1 - \frac{3}{2}\omega_D = 0.925, \tag{6.12}$$

where ω_D represents the deuteron D-state probability and the value of $\omega_D = 0.05 \pm 0.01$ [82, 83] was used in the analysis. The factor of $\frac{3}{2}$ is the Clebsh-Gordan coefficient of the sub-states [84]. The P-states are forbidden by parity conservation.

Eq. (6.4) can be extended for both the proton and deuteron targets introducing a mixing matrix $\mathcal{N}$ as

$$\vec{\boldsymbol{A}} = \mathcal{N} \cdot \mathcal{P} \cdot \vec{\boldsymbol{Q}}, \tag{6.13}$$

$$\mathcal{N} = \begin{pmatrix} 1 & & & & & \\ & \ddots & & & & \\ & & 1 & & & \\ a_D^{h_1} & & & b_D^{h_1} & & \\ & \ddots & & & \ddots & \\ & & a_D^{h_m} & & & b_D^{h_m} \end{pmatrix}, \tag{6.14}$$

where

$$a_D^{h_i} = f_{pd} p_{pd}, \qquad b_D^{h_i} = f_{nd} p_{nd}. \tag{6.15}$$

Eq. (6.13) can be solved by minimizing

$$\chi^2 = (\vec{\boldsymbol{A}}_{meas} - \mathcal{N} \cdot \mathcal{P} \cdot \vec{\boldsymbol{Q}})^T \mathcal{C}_A^{-1} (\vec{\boldsymbol{A}}_{meas} - \mathcal{N} \cdot \mathcal{P} \cdot \vec{\boldsymbol{Q}}), \tag{6.16}$$

where $\vec{\boldsymbol{A}}_{meas}$ is the measured asymmetries and $\mathcal{C}_A$ is covariance matrix of the measured asymmetries which accounts for the correlation of the various asymmetries.

6.1.1 Covariance Matrix

The components C_A^{ij} of covariance matrix for the asymmetries A_i and A_j are given by

$$C_A^{ij} = \mathrm{cov}(A_i, A_j)$$

$$\begin{aligned}
&= \sum_{\mu,\nu} \frac{\partial A_i}{\partial N_\mu} \frac{\partial A_j}{\partial N_\nu} \mathrm{cov}(N_\mu N_\nu) && (6.17)\\
&= \frac{\partial A_i}{\partial N_{i^+}} \frac{\partial A_j}{\partial N_{j^+}} \mathrm{cov}(N_{i^+}, N_{j^+}) + \frac{\partial A_i}{\partial N_{i^-}} \frac{\partial A_j}{\partial N_{j^-}} \mathrm{cov}(N_{i^-}, N_{j^-}) \\
&\simeq \frac{1}{2} \left[\frac{\partial A_i}{\partial N_{i^+}} \frac{\partial A_j}{\partial N_{j^+}} + \frac{\partial A_i}{\partial N_{i^-}} \frac{\partial A_j}{\partial N_{j^-}} \right] \mathrm{cov}(N_i, N_j) \\
&\simeq \frac{\partial A_i}{\partial N_{i^\pm}} \frac{\partial A_j}{\partial N_{j^\pm}} \mathrm{cov}(N_i, N_j), && (6.18)
\end{aligned}$$

where the sum runs over both spin states (indicated $N^{\overset{\rightarrow}{\Leftarrow}(\overset{\rightarrow}{\Rightarrow})}$ as $N_{+(-)}$). The covariance of hadron yield is assumed to be independent of the spin configuration. Additionally, it is assumed to be $N_i\pm \simeq \frac{1}{2}N_i$ and $|\frac{\partial A_i}{\partial N_{i^+}}| \simeq |\frac{\partial A_i}{\partial N_{i^-}}|$. The assumptions lead to $(\delta A_i)^2 = \frac{\partial A_i}{\partial N_{i\pm}} \cdot (\delta N_i)^2$. Hence C_A^{ij} is given by

$$C_A^{ij} = \frac{\delta A_i \delta A_j}{\delta N_i \delta N_j} \mathrm{cov}(N_i, N_j) = \delta A_i \delta A_j \mathrm{corr}(N_i, N_j). \tag{6.19}$$

6.2 Extraction of the Purities

Extraction of the purities were performed using HMC (HERMES Monte Carlo). A scheme of HMC is shown in Figure 6.1.

In the first step, LEPTO program [85] provides unpolarized DIS events at a given kinematic point of (x, Q^2). The CTEQ5L parameterization was used as input unpolarized parton distribution functions (PDFs). In the second step, JETSET program [86] processes hadronization and generates hadrons in its final states. In the hadronization process, the LUND string fragmentation model was used which will be described in Section 6.2.1. The model is the most suitable to simulate the HERMES experiment in the kinematic region [87]. The LUND parameters were chosen to reproduce the hadron multiplicities measured at the HERMES experiment [87]. Figure 6.2 shows a comparison of the hadron multiplicities of the experimental data with MC data. The acceptance due to the HERMES spectrometer and detector response are taken into account in HMC.

Using the HMC simulation, the purities are calculated as

$$P_f^h(x) = \frac{N_f^h(x)}{\sum_f N_f^h(x)}, \tag{6.20}$$

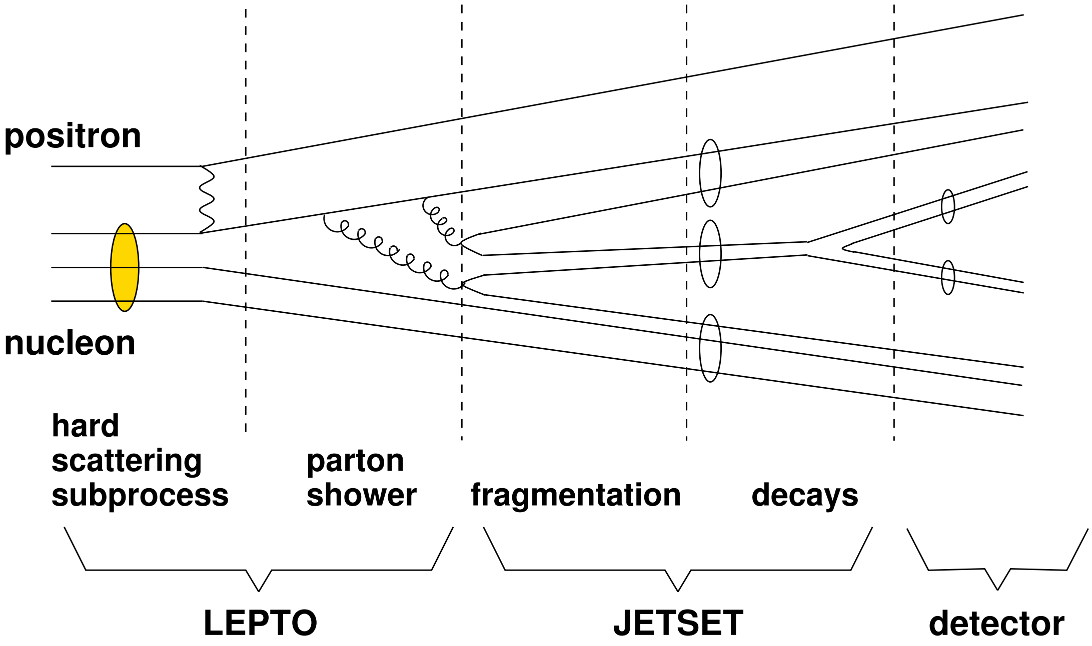

Figure 6.1: Scheme of the parts implemented in HMC

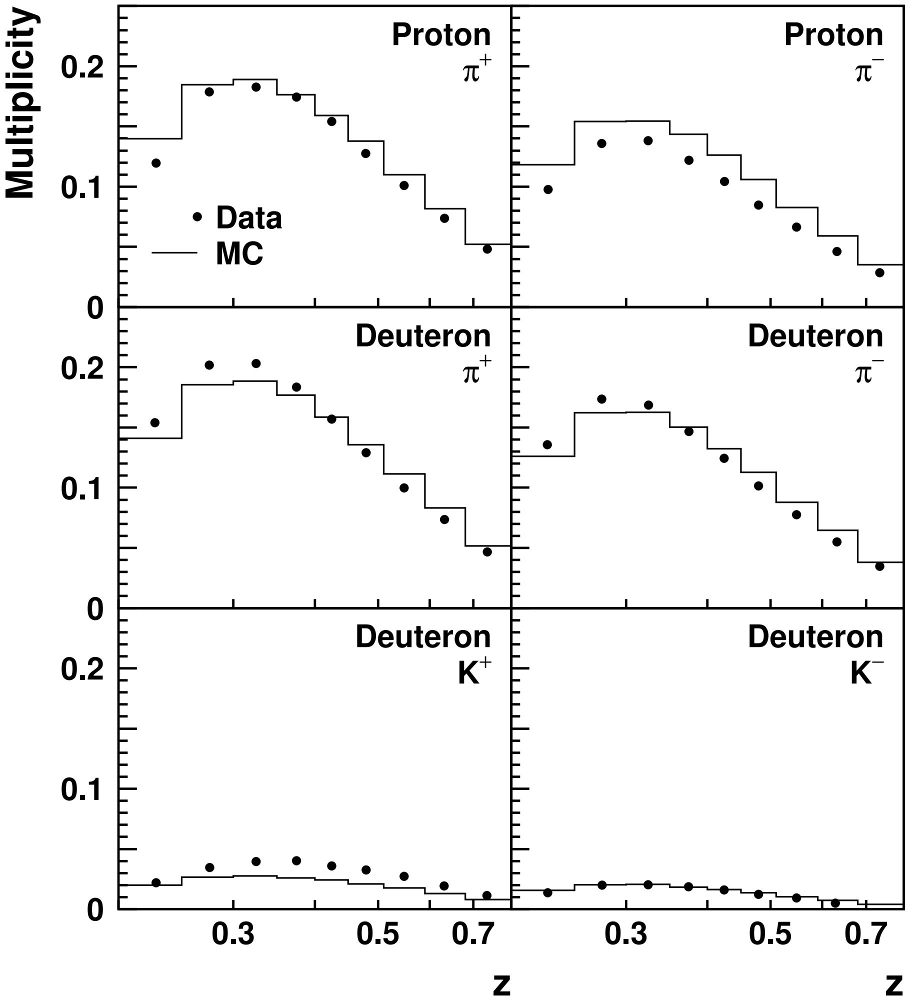

Figure 6.2: Comparison of hadron multiplicities of the experimental data (closed circles) with MC data (histograms) with proton or deuteron target. The multiplicities are shown as a function of z.

where N_f^h represents the number of detected hadron h originated from the quark with flavor f. The purities for inclusive DIS events are related to the unpolarized PDFs:

$$P_f^{inc}(x) = \frac{e_f^2 q_f(x)}{\sum_f e_f^2 q_f(x)} \tag{6.21}$$

6.2.1 Fragmentation Models

The fragmentation function which describes the hadronization processes is the probability that a quark of flavor f produces a final state hadron h which carries the momentum fraction z of the parent quark. This probabilistic interpretation of the fragmentation functions is valid for current fragments defined as processes in which hadrons are produced from the struck quark. Another processes in which hadrons are produced from the target remnant are called target fragments. The fragmentation functions $D(z)$ satisfy

$$\sum_h \int_0^1 z \cdot D_f^h(Q^2, z)dz = 1, \tag{6.22}$$

$$\sum_f \int_0^1 D_f^h(Q^2, z)dz = n_h(Q^2) \tag{6.23}$$

where n_h is hadron multiplicity. The fragmentation function is defined as favored fragmentation function D when one of the quarks in the final state hadron is the struck quark, while unfavored fragmentation function $\bar{D}$ when the struck quark is not contained in the hadron.

LUND String Model

The LUND string model describes the linear confinement of quarks at large distances [88] and is implemented in the JETSET. In the model, a quark is linked to an anti-quark by color field, so-called a string. When the energy due to the field exceeds the invariant mass of the $q\bar{q}$-pair, a new $q\bar{q}$ pair is produced. This process continues until the energy of the pair is close to the mass of the lightest colorless hadron. The $q\bar{q}$ pair forms a color singlet hadron.

Independent Fragmentation Model

The Independent Fragmentation model [89] is the first model of hadronization process by R. D. Field and R. P. Feynman. The model is based on a simple assumption that the struck quark is hadronized independently, that is, without the effect from the color field. One of the important parameters is γ_f which represents the probability that a $q\bar{q}$ pair is formed from quarks with the same flavor. From isospin symmetry, $\gamma_u = \gamma_d \equiv \gamma$ and from the definition of the probability, $\gamma_u + \gamma_d + \gamma_s = 1$. The ratio of the favored to unfavored fragmentation functions is given by

$$\frac{\bar{D}(z)}{D(z)} = \frac{\gamma(1-z)}{z + \gamma(1-z)}. \tag{6.24}$$

6.2.2 Unpolarized Parton Distributions

Parameterizations for the unpolarized parton distributions (PDFs) available are produced by CTEQ [90], GRV [91] and MRST [92]. As mentioned above, the CTEQ5L parameterization was used for the extraction of the purities. Recently the CTEQ6.1M parameterization is provided with the inclusion of 40 eigenvector basis PDF sets [93], while the CTEQ5L parameterization, which is a LO fit, does not include their uncertainties.

CTEQ6 Parameterization of unpolarized PDFs

The CTEQ6.1M parameterization of unpolarized PDFs is based on a fit to the world data which are the measurement of the structure function with high energy muon and electron beams and the measurement of the Drell-Yan deuteron/proton ratio, as well as information from the inclusive jet cross section in $\mathrm{p}\bar{\mathrm{p}}$ collision. The following functional form was used for the fit:

$$f(x, Q_0^2) = A_0^f x^{(A_1^f - 1)} (1-x)^{A_2^f} e^{A_3^f x} (1 + e^{A_4^f} x)^{A_5^f}, \tag{6.25}$$

where Q_0^2 = 1.3 GeV^2 and A_i^f is a free parameter for the parton flavor $f = u - \bar{u}, d - \bar{d}, g, \bar{u} + \bar{d}$. An additional parameterization allows to discriminate between the $\bar{u}$ and $\bar{d}$ distributions:

$$\frac{\bar{d}(x, Q_0^2)}{\bar{u}(x, Q_0^2)} = B_0 x^{B_1} (1-x)^{B_2} + (1 + B_3 x)(1-x)^{B_4}. \tag{6.26}$$

The s and $\bar{s}$ distributions were determined by a linear combination of the $\bar{u}$ and $\bar{d}$ distributions as

$$s(x, Q_0^2) = \bar{s}(x, Q_0^2) = 0.2(\bar{u}(x, Q_0^2) + \bar{d}(x, Q_0^2)). \tag{6.27}$$

Uncertainty analysis based on the Hessian method

In this section, how to determine the uncertainties of a physical quantity X which depends on the unpolarized PDFs is introduced. The quantity X is characterized by the 29 parameters (6 parameters for the 4 parton flavors and 5 parameters for $\bar{u}$ and $\bar{d}$ separation) described in the previous subsection. However 9 parameters are held fixed for lack of freedom of data samples. Hence remaining 20 parameters (defined as $a_1, \ldots, a_{20}$) are free parameters.

The best estimate of the 20 parameters was extracted using effective χ^2_{global} function defined as

$$\chi^2_{global} = \sum_n \omega_n \left(\frac{X_{data} - X_{theory}}{\sigma_{data}} \right)^2, \tag{6.28}$$

where X_{exp} and X_{theory} represent the quantity X measured at an experiment and calculated from a theoretical prediction with the 20 parameters, respectively. For simplicity, we denote χ^2 instead of χ^2_{global}. χ^2 can be expanded around its minimum χ^2_0 as

$$\chi^2 = \chi^2_0 + \sum_{i=1}^{20} \frac{\partial \chi^2}{\partial a_i} y_i + \frac{1}{2} \sum_{i=1}^{20} \sum_{j=1}^{20} H_{ij} y_i y_j + \ldots, \tag{6.29}$$

$$H_{ij} = \frac{\partial^2 \chi^2}{\partial a_i \partial a_j}, \tag{6.30}$$

where $y_i = a_i - a_i^0$, a_i^0 is the value at minimum and H_{ij} is called Hessian matrix. Assuming that the first derivatives of χ^2 are equal to zero at χ^2_0 (the second term vanishes) and the terms with more than third derivatives of χ^2 can be negligible, Eq. (6.29) is rewritten as

$$\chi^2 = \chi^2_0 + \frac{1}{2} \sum_{i=1}^{20} \sum_{j=1}^{20} H_{ij} y_i y_j. \tag{6.31}$$

Since the Hessian matrix is symmetrical ($H_{ij} = H_{ji}$), it has 20 eigenvectors v_i^k:

$$\sum_j^{20} H_{ij} v_j^k = \epsilon_k v_i^k. \tag{6.32}$$

By replacing y_i with $z_i = \sqrt{\epsilon_i} \sum_j^{20} y_i v_j^i$ and from Eq. (6.31), the following equation is obtained:

$$\Delta \chi^2 = \sum_i^{20} z_i^2. \tag{6.33}$$

This equation indicates that χ^2 increases uniformly in all the direction in z_i parameter space. This parameter sets are called eigenvector PDF sets and have two displacements from best fit in the plus and minus directions along the vector indicated as S_i^+ and S_i^-. Totally 40 PDF bases sets were evaluated to represent the uncertainties on the input data for the fit.

The uncertainty of the quantity X from the uncertainty on the unpolarized PDF is calculated as follows: Assuming that more than second terms of the Taylor-series expansion of X are sufficiently small, the uncertainty of X can be given by

$$\Delta X = \sum_{i=1}^{20} \frac{\partial X}{\partial z_i} z_i. \tag{6.34}$$

The square of ΔX can be obtained by

$$(\Delta X)^2 = \sum_{i}^{20} z_i^2 \sum_{j}^{20} \left(\frac{\partial X}{\partial z_j} \right)^2 = \Delta\chi^2 \sum_{j} \left(\frac{\partial X}{\partial z_j} \right)^2 . \tag{6.35}$$

Using $\frac{\partial X}{\partial z_i} = \sum_j \frac{\partial X}{\partial y_j} \partial y_j \partial z_i$, $(H^{-1})_{ij} = \sum_k \frac{1}{\epsilon_k} v_{ik} v_{jk}$ and $y_i = \sum_j v_{ij} \sqrt{\frac{1}{\epsilon_j}} z_j$, Eq. (6.35) can be re-written as

$$(\Delta X)^2 = \Delta\chi^2 \sum_{i,j} \frac{\partial X}{\partial y_i} (H^{-1})_{i,j} \frac{\partial X}{\partial y_j}. \tag{6.36}$$

Furthermore $(\Delta X)^2$ is expressed in terms of 40 PDF basis sets [93, 94]:

$$(\Delta X)^2 = \frac{1}{4} \left(\sum_{i=1}^{20} [X(S_i^+) - X(S_i^-)]^2 \right)^2 . \tag{6.37}$$

Figure 6.3 shows the comparison between CTEQ5L and CTEQ6.1M which are evaluated at a fix value of $Q^2 = 2.5\mathrm{GeV}^2$. There is no big difference between the PDFs. Therefore we assumed that the error on LO is approximately the same as on NLO.

6.2.3 Sources of Systematic Uncertainty on the Purity

The systematic uncertainties on the purities are described in this section. The difference from two LUND parameter sets is assigned as the error from the fragmentation model. Another contribution is due to the error on the unpolarized parton distributions. These errors in turn contribute to the quark polarization which will be described in Section 6.2.4.

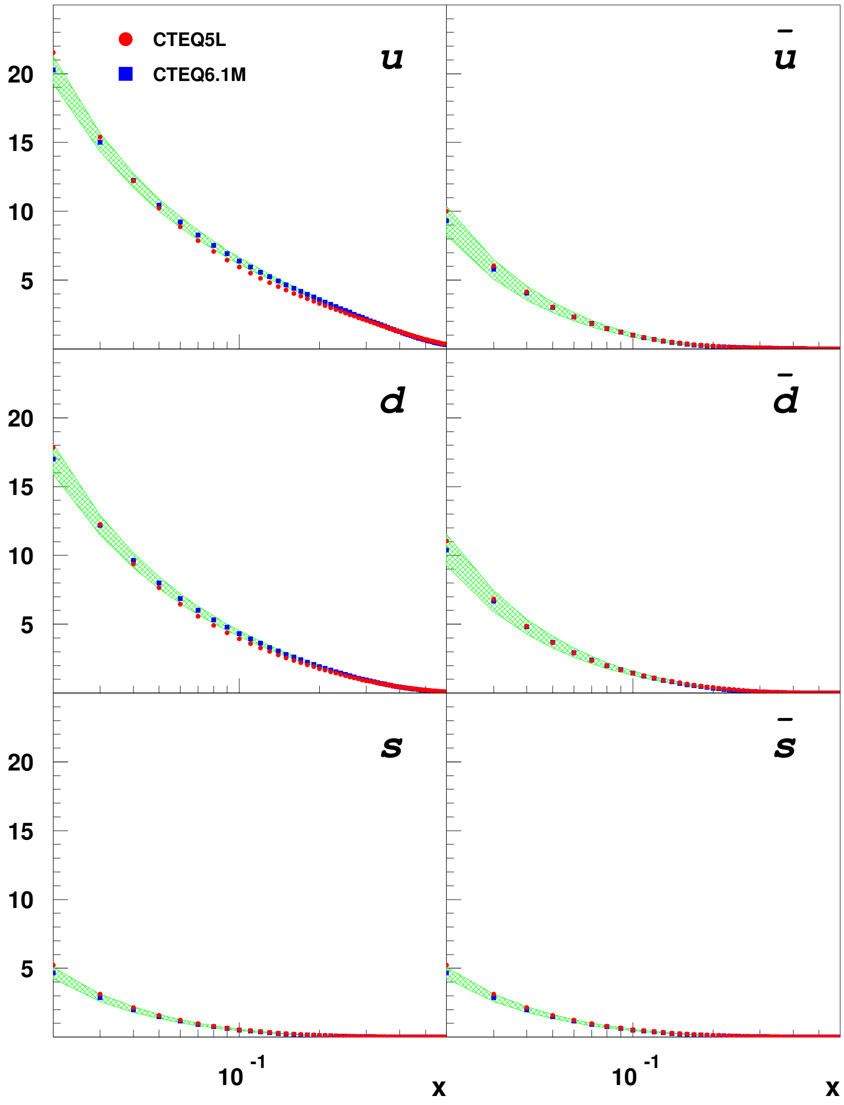

Figure 6.3: CTEQ5L(LO) vs CTEQ6.1M(NLO) as a function of x. The PDFs are evaluated at a fixed value of $Q^2 = 2.5\mathrm{GeV}^2$. The bands represent the systematic uncertainties for the CTEQ6.1M parameterization.

JETSET parameter	Current Setting	Old Setting
PARJ(1)	0.02	0.10
PARJ(2)	0.20	0.16
PARJ(5-7)	0.00	0.50
PARJ(21)	0.37	0.01
PARJ(23)	0.03	0.01
PARJ(24)	2.50	2.00
PARJ(33)	0.80	0.80
PARJ(41)	1.74	0.82
PARJ(42)	0.23	0.24
PARL(3)	0.44	0.44

Table 6.1: JETSET parameters for the current and old setting.

Fragmentation Model

The systematic uncertainties due to the fragmentation model are estimated by comparing the results from the two JETSET parameters of the current and old setting. The two parameter sets are listed in Table 6.2.3 [50].

Unpolarized Parton Distributions

The systematic uncertainties due to the error on the unpolarized PDFs are estimated by using the 40 eigenvector sets as described in Section 6.2.2. In the extraction of the hadron yield, additional Q^2 bins are introduced. The binning in Q^2 is listed in Table 6.2. New hadron yields $(N_q^h)_i^{new}$ are calculated as

Bin	1	2	3	4	5	6	7	8
Q^2_{low} [GeV^2]	1.0	1.5	2.0	2.5	3.0	3.5	4.0	4.5
Q^2_{up} [GeV^2]	1.5	2.0	2.5	3.0	3.5	4.0	4.5	5.0
Bin	9	10	11	12	13	14	15	
Q^2_{low} [GeV^2]	5.0	6.0	7.0	8.0	9.0	10.0	15.0	
Q^2_{up} [GeV^2]	6.0	7.0	8.0	9.0	10.5	15.0	-	

Table 6.2: Definition of binning in Q^2.

$$(N_q^h)_i^{new}(x) = \sum_k N_q^h(x, Q_k^2) + N_q^h(x, Q_k^2) \cdot \frac{\Delta q^i_{CTEQ6.1M}(x, Q_k^2)}{q_{CTEQ5L}(x, Q_k^2)}, \tag{6.38}$$

where the sum loops over all the Q^2 bins and $\Delta q^i_{CTEQ6.1M}$ represents the error on the PDF for the i-th eigenvector. Thus the 40 purities are obtained following the Eq. (6.20).

RICH Particle Identification

The contribution from the RICH systematic error should be taken into account since the JETSET parameters were tuned to the experimental multiplicities measured with the RICH detector. The contribution was not considered in this analysis. However the systematic uncertainty due to RICH can be canceled in the quark polarization extraction because the uncertainties on the asymmetry and purity are strongly correlated each other. At this moment it has not been established yet how to extract the RICH uncertainty on the purity. So in the following analyses the RICH uncertainty will not be taken into account.

6.2.4 Resulting purities

The resulting purities are shown in Figure 6.4 for the proton target and in Figure 6.5 for the neutron target as a function of x. The solid and hatched bands represent the systematic uncertainties due to the fragmentation model and due to the error on the unpolarized PDFs. The purities for s and $\bar{s}$ quarks are increased by a factor of 4. The u quark contributions for the purities are enhanced due to the squared fractional charge of the quark by a factor of 4 and the purities of u quark increase with x. For $x < 0.1$, where sea quarks dominate, $\bar{u}$ quark contribution becomes sensitive to the purities. The contributions of s and $\bar{s}$ quarks are sensitive to K^- and K^+ purities. However these quark contributions for all the purities are small in the full range of x.

6.3 Extraction of the Quark Polarization and the Helicity Distributions

As described in Section 6.1, the quark polarizations can be obtained by minimizing

$$\chi^2 = (\vec{\boldsymbol{A}}_{meas} - \mathcal{N} \cdot \mathcal{P} \cdot \vec{\boldsymbol{Q}})^T \mathcal{C}_A^{-1} (\vec{\boldsymbol{A}}_{meas} - \mathcal{N} \cdot \mathcal{P} \cdot \vec{\boldsymbol{Q}}). \tag{6.39}$$

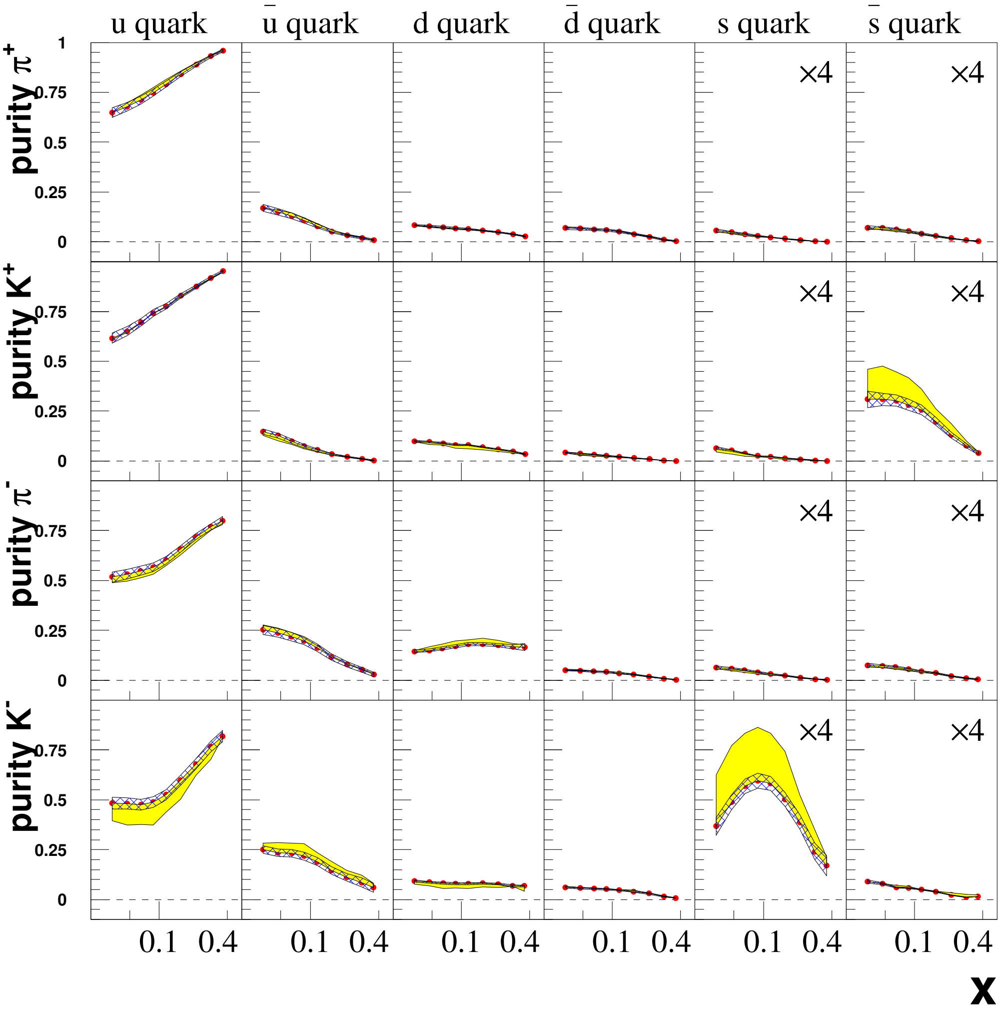

Figure 6.4: The generated purities for the proton target. The solid and hatched bands represent the systematic uncertainties from the fragmentation model and the error on the unpolarized PDFs.

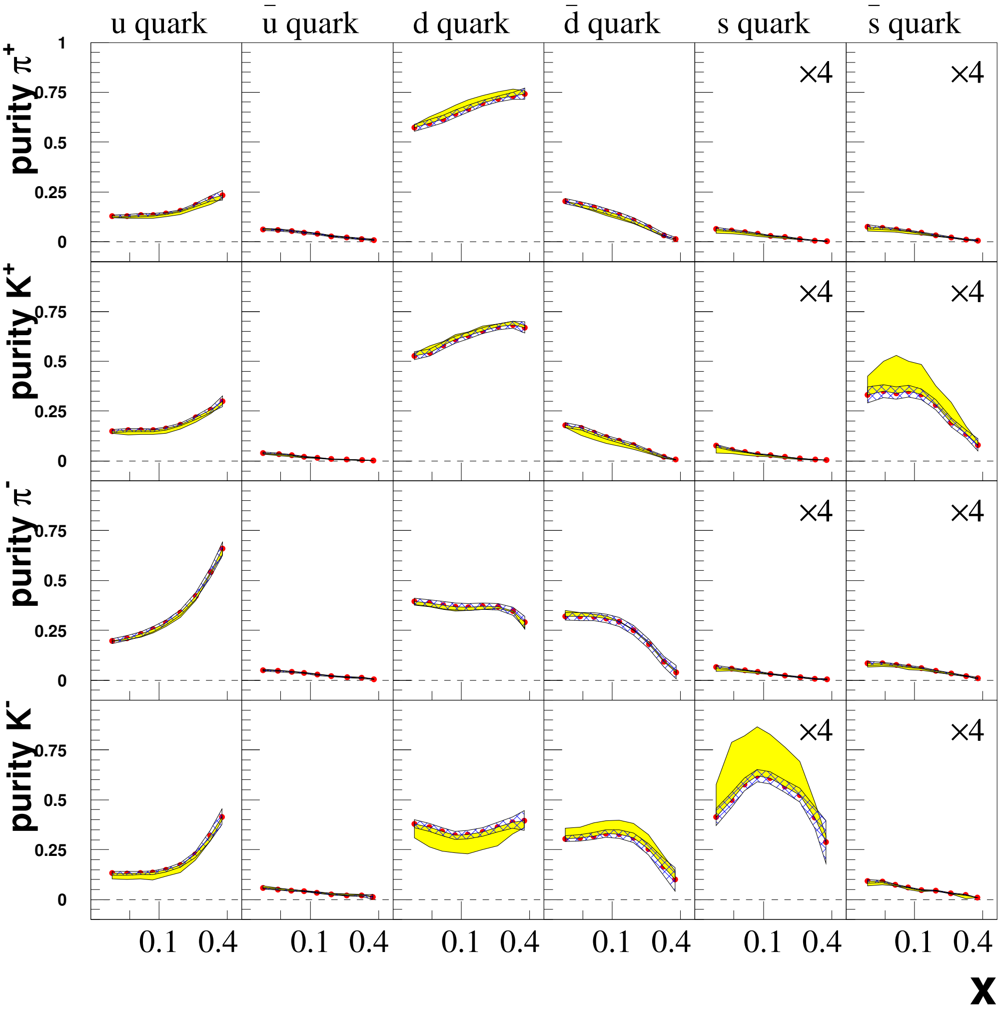

Figure 6.5: The generated purities for the neutron target. The purities are isospin rotated, that is, for example u quark corresponds to d quark in neutron. The error bands are the same as for the proton purities.

In the calculation of χ^2, the systematic covariances are excluded since it was found to bias the result of the fit [95]. To solve the above equation, two semi-inclusive asymmetries for the proton and four for the deuteron were used together with the inclusive asymmetries for the both targets:

$$\vec{\boldsymbol{A}}_{meas} = (A_p, A_p^{\pi^+}, A_p^{\pi^-}, A_d, A_d^{\pi^+}, A_d^{\pi^-}, A_d^{K^+}, A_d^{K^-}). \tag{6.40}$$

We assumed

$$\Delta\bar{s} = 0. \tag{6.41}$$

The assumption on s quark will be described in Section 6.4.1. Furthermore, the contribution from all the sea flavors for $x > 0.3$ is assumed to be zero:

$$\Delta\bar{u}(x) = \Delta\bar{d}(x) = \Delta s(x) = \Delta\bar{s}(x) = 0 \ \text{ for } \ x > 0.3. \tag{6.42}$$

Under these assumptions, the vector of the quark polarizations is given by

$$\vec{\boldsymbol{Q}}(x) = \left(\frac{\Delta u}{u}(x), \frac{\Delta d}{d}(x), \frac{\Delta\bar{u}}{\bar{u}}(x), \frac{\Delta\bar{d}}{\bar{d}}(x), \frac{\Delta s}{s}(x)\right). \tag{6.43}$$

Then the solution of Eq. (6.13) can be obtained by using a linear regression [96].

$$\vec{\boldsymbol{Q}} = \left((\mathcal{NP})^T\mathcal{C}_A^{-1}(\mathcal{NP})\right)^{-1}(\mathcal{NP})^T\mathcal{C}_A^{-1}(\vec{\boldsymbol{A}}_{meas} - \mathcal{PN}\vec{\boldsymbol{Q}}_{fix}), \tag{6.44}$$

where $\vec{\boldsymbol{Q}}_{fix}$ is the constrained polarizations by Eq. (6.41) and Eq. (6.42). The covariance matrix of the quark polarizations can be given by

$$\mathcal{C}(\vec{\boldsymbol{Q}}) = \left[\left((\mathcal{NP})^T(\mathcal{C}_A)^{-1}\mathcal{NP}\right)^{-1}(\mathcal{NP})^T(\mathcal{C}_A)^{-1}\right]\mathcal{C}_A^{tot}\left[(\mathcal{C}_A)^{-1}\mathcal{NP}\left((\mathcal{NP})^T\mathcal{C}_A^{-1}\mathcal{NP}\right)^{-1}\right], \tag{6.45}$$

where $\mathcal{C}_A^{tot}$ represents the sum of the statistical and systematic covariance matrix of the asymmetries ($\mathcal{C}_A^{tot} = \mathcal{C}_A^{stat} + \mathcal{C}_A^{sys}$).

The helicity distributions $\Delta q(x)$ are evaluated at a fixed value of Q_0^2:

$$\Delta q(x) = \frac{\Delta q}{q}(x) \cdot q(x, Q_0^2 = 2.5\mathrm{GeV}^2). \tag{6.46}$$

6.3.1 Systematic Uncertainties of the Quark Polarizations

The systematic uncertainties of the quark polarizations due to the error on the unpolarized PDFs were estimated according to Eq. (6.37) using the 40 purities described in Section 6.2.3. The contribution due to the fragmentation model was determined to calculate the difference of the quark polarizations using the two parameter sets described in Section 6.2.3.

The total systematic uncertainties of the quark polarization are the sum of all the contributions.

6.4 Resulting Quark Polarizations and Quark Helicity Distributions

The resulting quark polarizations are shown in Figure 6.6. The polarizations of u and d quarks were determined with high precision. The polarization of u quark is positive and increases with x. On the other hand, the polarization of d quark is negative. The polarizations of sea quarks $\bar{u}$, $\bar{d}$ and s quarks, are consistent with zero within the errors. The x weighted helicity distributions are presented in Figure 6.7. The results are compared with two theoretical predictions from the GRSV parameterization (LO, “valence” scenario) [51] and the Blümleing-Böttcher parameterization [52]. The GRSV result was extracted using the spin asymmetries A_1 of inclusive measurements for the proton, neutron and deuteron from HERMES [35], EMC [7], SMC [33] and SLAC [32]. In the extraction, they set the ratio of the photo absorption cross section $R(x, Q^2)$ zero. For the comparison with our results, their results are scaled with $\frac{1}{1+R}$. The another parameterization was performed by Blümlein and Böttcher. They performed QCD fits on the polarized structure function g_1 evaluated from the spin asymmetries. Then the helicity distributions were extracted from the parameterization under an assumption of SU(3) flavor symmetry and a flavor symmetric sea. The HERMES results are in good agreement with the two fits. It should be stressed that HERMES decomposed the separate spin contributions of quarks and anti-quarks to the nucleon spin x bin by bin, thanks to the asymmetries data from semi-inclusive hadron measurement. On the other hand, the theoretical predictions are constrained by the assumption of the functional form. Strong assumptions on the sea quark are also made in the fits. The values of the quark polarizations and x weighted helicity distributions are listed with the statistical and the systematic uncertainties in Table A.14.

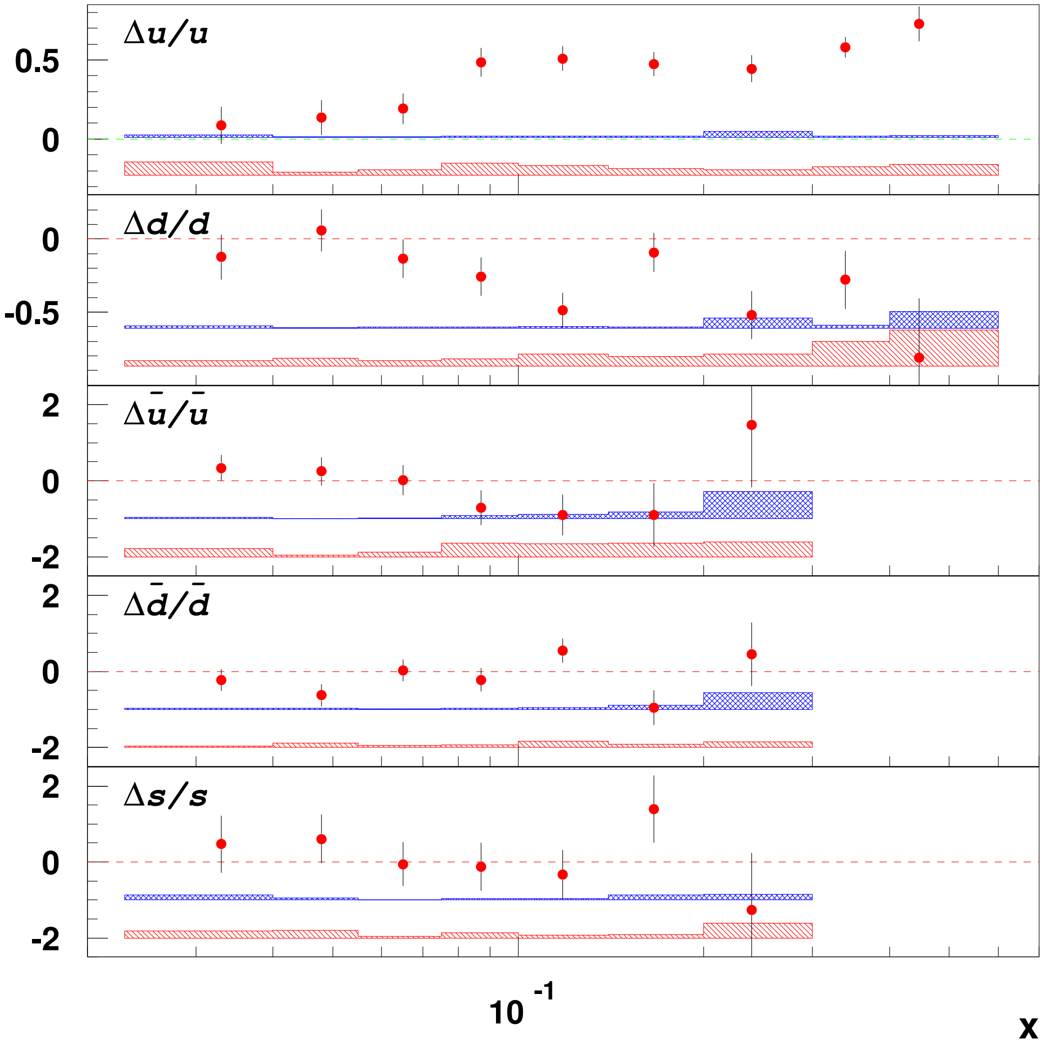

Figure 6.6: The quark polarizations as a function of x. The error bars show the statistical uncertainties. The upper and lower bands represent the systematic uncertainties due to the error on the unpolarized PDFs, and the uncertainties on the fragmentation model and the asymmetries respectively.

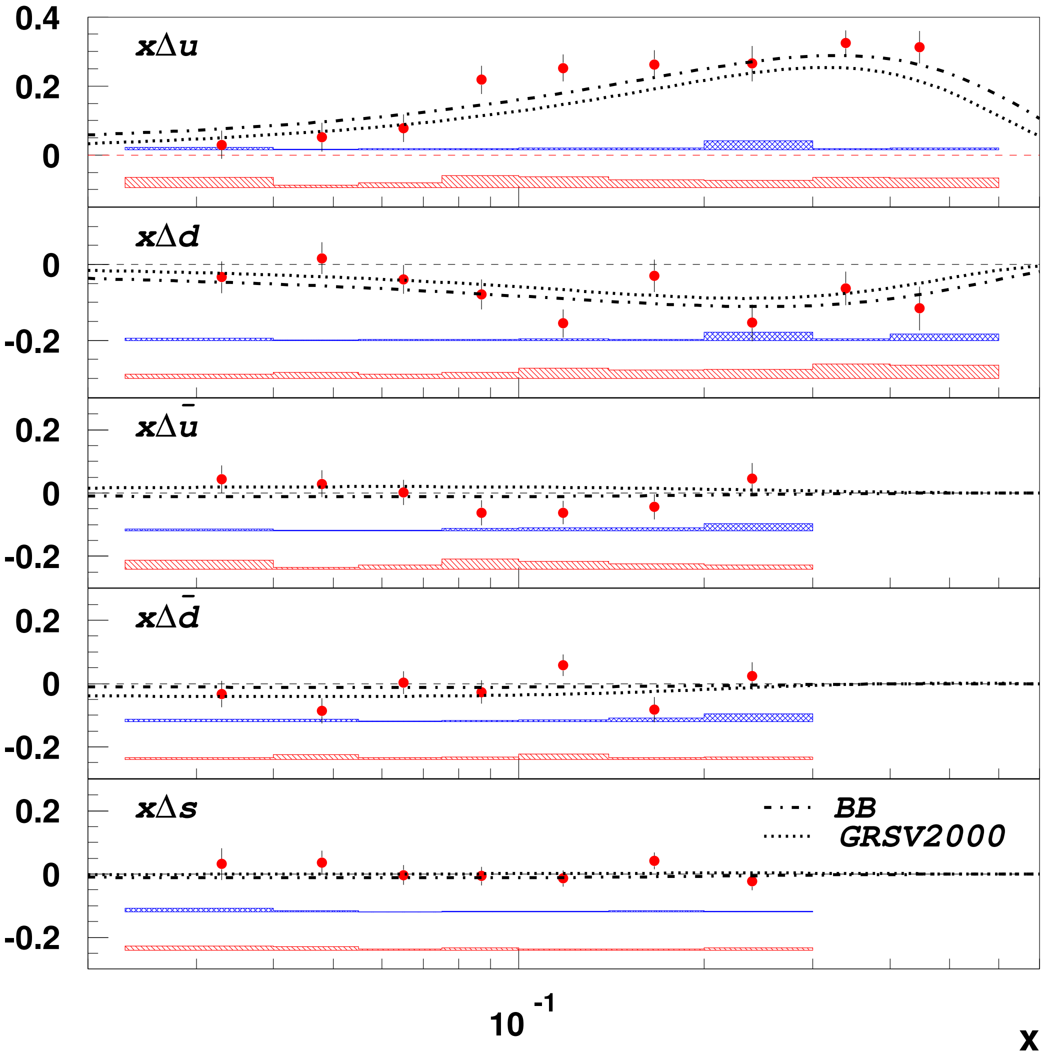

Figure 6.7: The x weighted helicity distributions evaluated at a fixed value of $Q_0^2 = 2.5\mathrm{GeV}^2$. The error bars and bands are shown in the same manner as Figure 6.6. The data are shown together with two theoretical prediction from the GRSV2000 parameterization [51] scaled with $\frac{1}{1+R}$and the Blümlein-Böttcher (BB) parameterization [52]

6.4.1 Assumption on the strange quark polarization

To conserve the strangeness,

$$\int_0^1 dx\,(s(x) - \bar{s}(x)) = 0 \tag{6.47}$$

is only required. It is not necessary to be $s(x) = \bar{s}(x)$. Furthermore there are no constrains on $\Delta s(x)$ and $\Delta\bar{s}(x)$. Though $\bar{s}$ quark is the valence quark in the positive kaon, the production of the positive kaon dominantly occurs in events where a u quark was struck. The evidence is shown in the positive kaon purity (see Figure6.4). On the other hand, sensitivity to the production of the negative kaon asymmetry in events where s quark was struck is better since the negative kaon is constructed from both sea quarks ($\bar{u}, s$). The assumption of $\Delta\bar{s} = 0$ is further motivated by the chiral quark soliton model [97].

The extraction of the quark polarization under the different assumptions on the polarized PDF for the strange quark was performed. Figure 6.8 [95] shows the resulting quark polarization. One can see that there is no big discrepancy due to the different assumptions on the polarized PDF for the strange quark.

6.4.2 z-dependence of the Asymmetries

To check whether the sample of semi-inclusive DIS events are pure DIS events for the extraction of the Born asymmetries, z-dependence of the asymmetries were studied. The identified DIS events could originate from target fragmentation and non-partonic processes such as diffractive interactions especially at high z [90]. These contributions cause z-dependence of the asymmetries. The z-dependence was calculated using the unpolarized (CTEQ5L) and polarized (HERMES) PDFs and the fragmentation functions as

$$\begin{aligned} A^h(z_i) &= \frac{\int\int dx dQ^2 g_1(x, Q^2, z_i)}{\int\int dx dQ^2 F_1(x, Q^2, z_i)} \\ &= \frac{\int\int dx dQ^2 \sum_f e_f^2 \delta q_f(x, Q_0^2) D_f^h(Q_0^2, z_i) \mathrm{Acc}(x, z_i)}{\int\int dx dQ^2 \sum_f e_f^2 q_f(x, Q_0^2) D_f^h(Q_0^2, z_i) \mathrm{Acc}(x, z_i)} \end{aligned} \tag{6.48}$$

where the fragmentation functions D_f^h from [98] were used and $\mathrm{Acc}(x, z_i)$ is a x distribution for each z-bin normalized by satisfying $\int dz \mathrm{Acc}(z) = 1$. Here the CTEQ5L parameterization was used as an input of the unpolarized PDFs. The

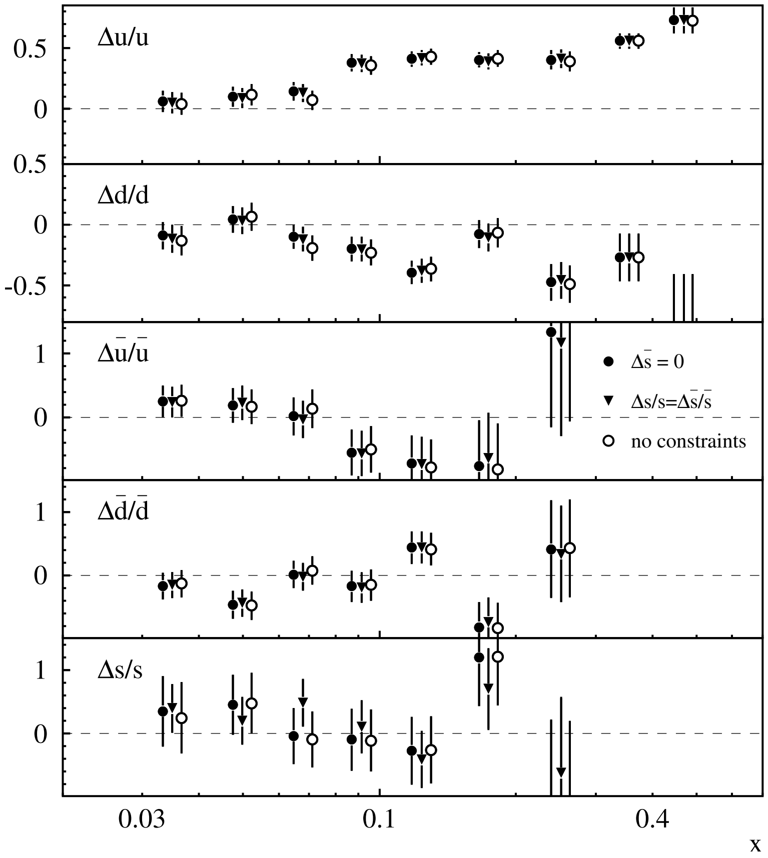

Figure 6.8: Quark polarizations under the different assumptions on the polarized PDF for the strange quark. The results are slightly shifted for better presentation.

asymmetries are evaluated at a fixed $Q_0^2 = 2.5\mathrm{GeV}^2$. Figure 6.9 shows the favored and unfavored fragmentation functions together with the ratio of the two fragmentation functions. As can be seen in the figure, the contribution from unfavored quarks is suppressed compared to favored quarks by a factor of about 2 to 10 at higher z. The x distributions for the positive pion measured in each z_i are shown in Figure 6.10. These distributions are extracted from the experimental data. One can see that the peaks are shifted to higher x as z increases.

The resulting asymmetries as a function of z are shown together with the asymmetries from the HERMES experimental data in Figure 6.11 for the proton and Figure 6.12 for the deuteron. They are in good agreement within the statistical uncertainties. The negative pion asymmetry for the proton decreases with z. This is due to the suppression of the unfavored fragment processes at higher z, for example the positive contribution from u quark. The results show that there is no important z-dependence of the asymmetries. Therefore the contribution from the background processes can be negligible within the present statistical precision.

6.4.3 Comparison with Results from the Other Experiments

In this section, the quark polarizations obtained at the HERMES experiment are compared with other experiments.

Comparison with SMC Results

As mentioned in Section 2.6.1, the SMC results are based on a fit of the valence quark helicity distributions Δu_v, Δd_v and the sea quark helicity distribution $\Delta\bar{q}$. A symmetric sea polarization is assumed. To compare with the results from SMC, the three parameter fit

$$\vec{\boldsymbol{Q}} = (\Delta u_v, \Delta d_v, \Delta\bar{q}) \tag{6.49}$$

was performed with HERMES data incorporating the full covariance of the asymmetries. The quark helicity distributions are evaluated at a fixed value of $Q_0^2 = 2.5\mathrm{GeV}^2$. The comparison plot is shown in Figure 6.13. The HERMES results and SMC ones are in good agreement within the errors. The statistical uncertainties of $\Delta u_v(x)$ for HERMES are smaller than SMC ones.

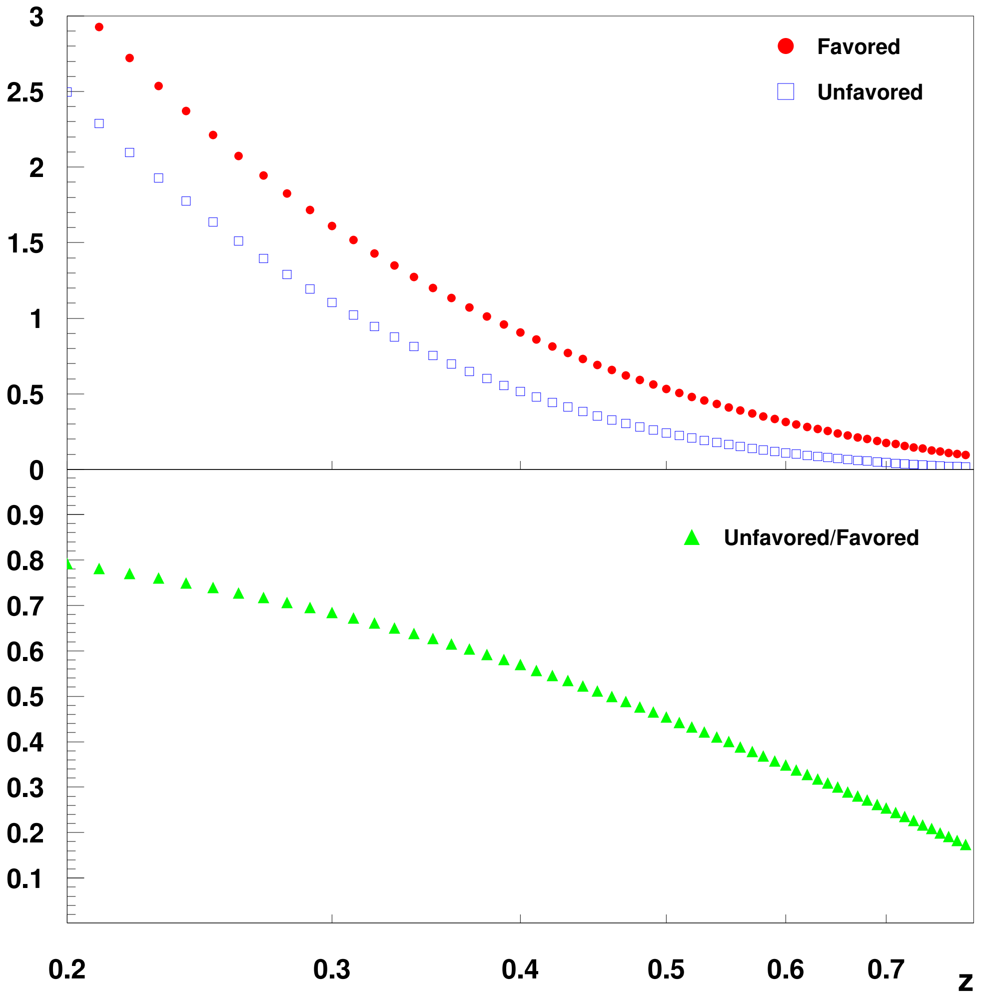

Figure 6.9: The fragmentation functions from e^+e^- collisions [98]. The upper panel shows the favored and unfavored fragmentation functions indicated by the closed circles and the open squares respectively. The lower panel represents the ratio of the two fragmentation functions.

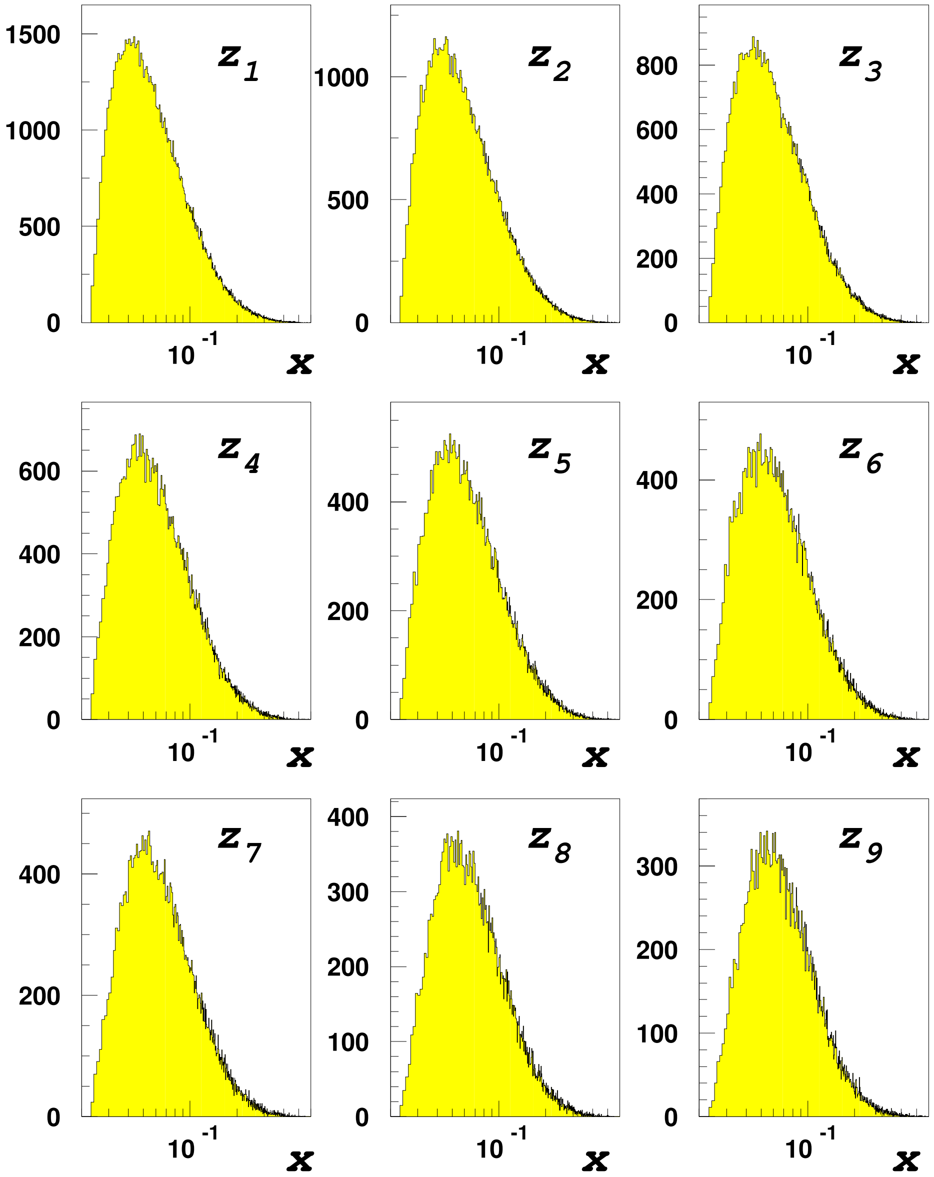

Figure 6.10: The x distributions for positive pion. The top three panels show the distribution at $z = 0.23, 0.28, 0.32$, the middle three panels at $z = 0.37, 0.42, 0.48$, and the bottom three panels at $z = 0.55, 0.63, 0.74$.

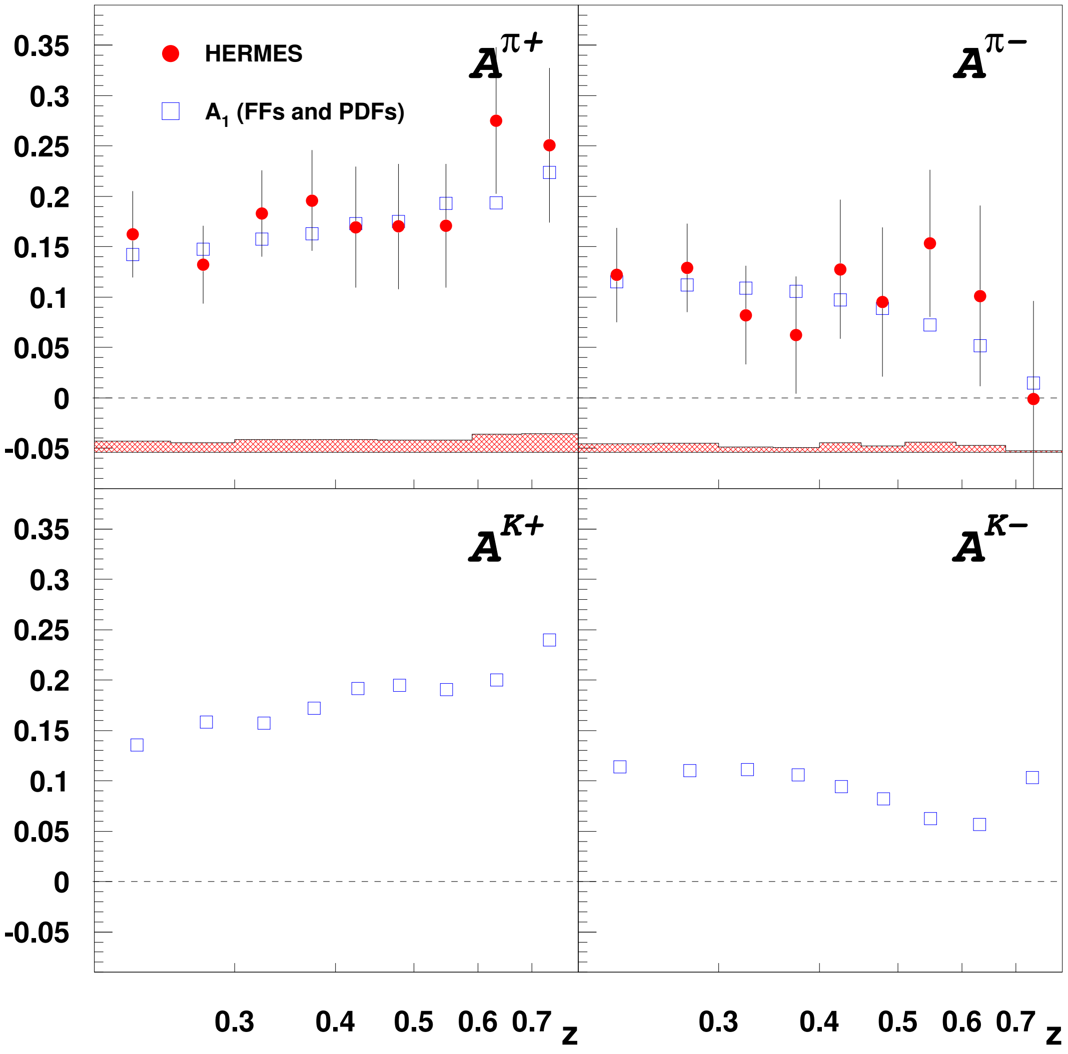

Figure 6.11: The asymmetries as a function of z for the proton target. The closed circles are results from the HERMES experimental data and the open squares are the results from the PDFs and the fragmentation functions as described in the text. The error bars show the statistical uncertainties and the bands the systematic uncertainties for the experimental data.

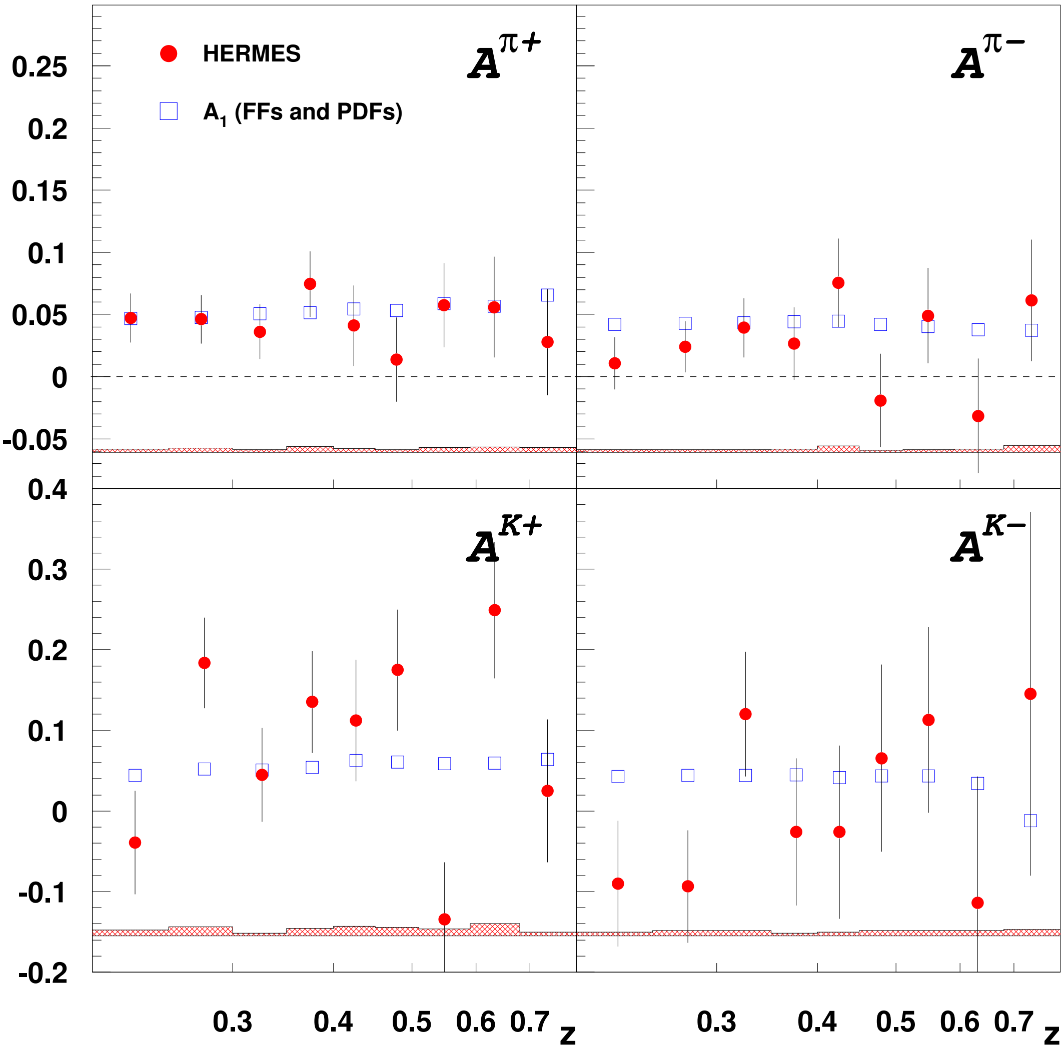

Figure 6.12: The asymmetries as a function of z for the deuteron target. The closed circles are results from the HERMES experimental data and the open squares are the results from the PDFs and the fragmentation functions as described in the text. The error bars show the statistical uncertainties and the bands the systematic uncertainties for the experimental data.

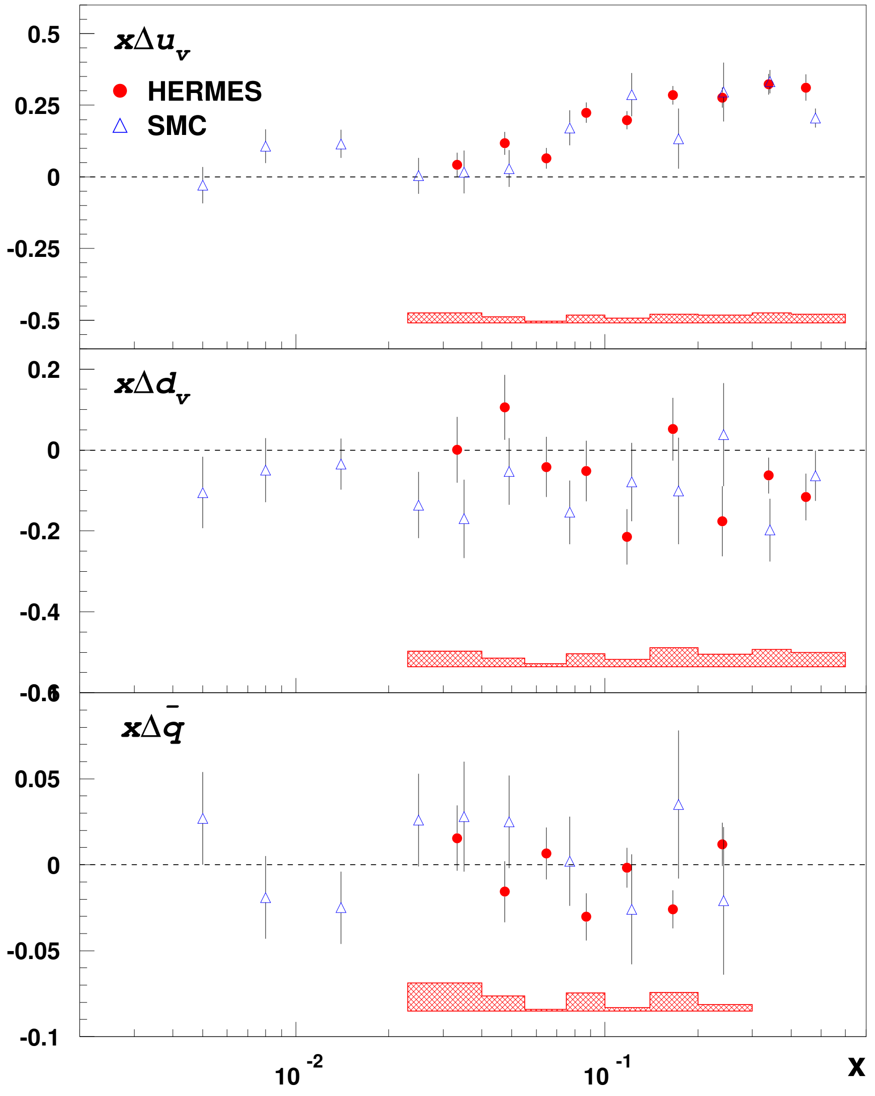

Figure 6.13: Quark helicity distributions for the valence quarks $x\Delta u_v(x), x\Delta d_v(x)$ and the sea quark $x\Delta\bar{q}(x)$. They are compared with results from SMC. The error bars show the statistical uncertainties and the error bands the systematic uncertainties for the HERMES results.

Comparison with JLAB results

The Jefferson Lab Hall A Collaboration (indicated as JLAB in the following) performed measurement of the neutron spin asymmetry A_1^n and quark polarizations of $\frac{\Delta u+\Delta\bar{u}}{u+\bar{u}}$ and $\frac{\Delta d+\Delta\bar{d}}{d+\bar{d}}$ [99]. They measured the inclusive double spin asymmetry for $^3\mathrm{He}$ target in three kinematic region of $(x, Q^2[\mathrm{GeV}^2]) = (0.33, 2.7), (0.47, 3.5)$ and $(0.60, 4.8)$, and extracted A_1^n from $A_1^{^3\mathrm{He}}$ by using the world proton and deuteron fits for the structure function F_2 and the photo absorption cross section ratio R. Assuming the contributions from s and $\bar{s}$ quarks can be negligible, they extracted the quark polarizations by using the world data of $\frac{g_1^p}{F_1^p}$ and, proton and deuteron structure function data. The calculation is based on the quark parton model and the quark polarizations are given by

$$\frac{\Delta u+\Delta\bar{u}}{u+\bar{u}} = \frac{4}{15}\frac{g_1^p}{F_1^p}(4+\frac{d+\bar{d}}{u+\bar{u}}) - \frac{1}{15}\frac{g_1^n}{F_1^n}(1+4\frac{d+\bar{d}}{u+\bar{u}}),$$
$$\frac{\Delta d+\Delta\bar{d}}{d+\bar{d}} = \frac{4}{15}\frac{g_1^n}{F_1^n}(4+\frac{u+\bar{u}}{d+\bar{d}}) - \frac{1}{15}\frac{g_1^p}{F_1^p}(1+4\frac{u+\bar{u}}{d+\bar{d}}).$$

To compare with the results from JLAB, the five parameter fit of

$$\vec{\boldsymbol{Q}} = (\Delta u+\Delta\bar{u}, \Delta d+\Delta\bar{d}, \Delta\bar{u}, \Delta\bar{d}, \Delta s) \tag{6.50}$$

was performed under the assumption of $\Delta\bar{s} = 0$. The fit incorporates the full covariances of the various asymmetries. Figure 6.14 shows the comparison of the HERMES results with JLAB ones. They are consistent within the statistical and systematic uncertainties.

6.5 Moments of Helicity Distributions

The n-th moment $\Delta^{(n)}q(Q^2)$ of the helicity distribution $\Delta q(x, Q^2)$ is calculated as

$$\Delta^{(n)}q(Q^2) = \int_0^1 dx x^{n-1}\Delta q(x, Q^2). \tag{6.51}$$

In the HERMES measured region ($0.023 < x < 0.6$), the moments are evaluated as

$$\Delta^{(n)}q(Q_0^2) = \int_{0.023}^{0.6} dx x^{n-1}\Delta q(x, Q^2) = \Sigma_i\left(\frac{\Delta q}{q}(x_i)\int_{\xi_i}^{\xi_{i+1}} q(x, Q^2)\right), \tag{6.52}$$

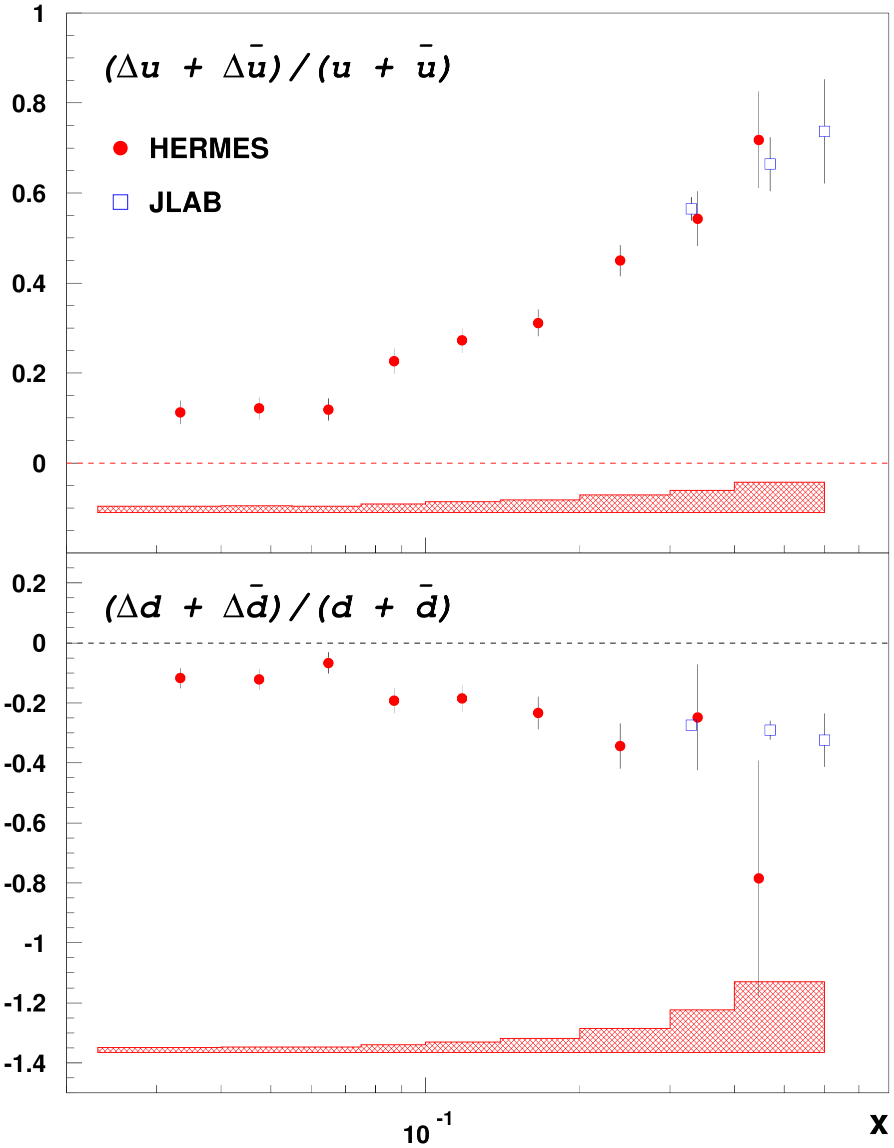

Figure 6.14: Quark polarizations of u and d quarks. They are compared with results from JLAB. The error bars show the statistical uncertainties and the error bands the systematic uncertainties for the HERMES results.

where $Q_0^2 = 2.5\mathrm{GeV}^2$ is the average value of Q^2 determined experimentally, ξ_i and x_{i+1} represent the boundary of i-th x bin and i runs over all x bins. We assumed that the quark polarization is constant in each x bin. The CTEQ5L parameterization was used for the unpolarized PDF. The covariant matrices of the moments are given by

$$\mathcal{C}(\Delta q) = \sum_{i,j} \int_{xi_i}^{\xi_{i+1}} dx x^{n-1} q(x, Q_0^2) \int_{\xi_j}^{\xi_{j+1}} dx x^{n-1} q(x, Q_0^2) \mathcal{C}(\vec{\boldsymbol{Q}}). \tag{6.53}$$

The results for the first moment of the helicity distribution are listed in Table6.3. The positive u quark contribution and the negative d quark contribution with respect to the proton spin are observed with good accuracy. The sea quark polarizations are consistent with zero within the statistical and systematic errors. The effect of the uncertainty on the unpolarized PDFs to the first moments are evaluated in the same way to the analysis procedure employed in the extraction of the helicity distributions. The fractional uncertainty on the first moment for u quark is $\simeq$ 3% and that for d quark is $\simeq$ 7 % . Thus it was found the effect of the uncertainties on the first moment were sufficiently small.

	Δq	σ_{stat}	σ_{syst}	σ_{PDF}	σ_{total}
Δu	0.601	0.039	0.049	0.020	0.066
Δd	-0.226	0.039	0.023	0.016	0.065
$\Delta \bar{u}$	-0.002	0.036	0.023	0.012	0.044
$\Delta \bar{d}$	-0.054	0.033	0.011	0.015	0.038
Δs	0.028	0.033	0.009	0.008	0.035

Table 6.3: The first moment of the helicity distributions. The moments are calculated in the HERMES measured region ($0.023 < x < 0.6$).

Chapter 7

Conclusion

HERMES investigates the spin structure of the nucleon with Deep Inelastic Scattering (DIS) of 27.6 GeV longitudinally polarized positron and longitudinally polarized gas targets. The experiment was motivated to solve the "nucleon spin problem" found by the EMC experiment. About 2 million DIS events for the proton target and 7 million DIS events for the deuteron target were accumulated during the 1996 to 2000 data taking periods and analyzed.

For the year 1996 and 1997, the threshold Čerenkov detector has been operated. It allows to separate pions and non-pion particles. In 1998, HERMES installed a Ring Imaging Čerenkov (RICH) detector. The RICH detector can identify pions, kaons and protons. The RICH detector uses dual radiators, aerogel with the refractive index $n_{\mathrm{aero}} = 1.0303$ and $\mathrm{C_4F_{10}}$ gas with $n_{\mathrm{C_4F_{10}}} = 1.00137$. We employed the semi-inclusive measurements using information from the RICH detector. It enables us to determine semi-inclusive cross section asymmetries between parallel and anti-parallel configuration of the beam and target spins.

Using the asymmetries for the proton target from the 1996 and 1997 data taking period and for the deuteron target from 1998 to 2000, the separate quark contributions to the proton spin $(\Delta u, \Delta d, \Delta s, \Delta \bar{u}, \Delta \bar{d}$ and $\Delta s)$ are extracted. The extraction of the quark helicity distributions is based on Leading Order (LO) QCD which is described as one photon exchange between the positron and the target nucleon. The polarization of u quark in the proton is positive and increases with x. The polarization of d quark in the proton is negative. The polarizations of $\bar{u}, \bar{d}$ and s quarks are consistent with zero within the statistical and systematic uncertainties. The results are compared with ones by other experiments, JLAB and SMC. They are in good agreement within the errors.

The evaluation of efficiency of the hadron identification with RICH was carried out by hadron tagging using decaying particles such as $\rho, \phi, \Lambda, K_s^0$. The method to estimate the uncertainty on the asymmetries from the hadron misidentification with RICH was established. This uncertainty is propagated to the quark helicity distributions.

The effect of the uncertainty on the unpolarized PDFs was evaluated. The CTEQ5L parameterization for LO used in the analysis is provided without the uncertainties, while the CTEQ6.1M parameterization for Next-to-Leading Order (NLO) includes estimates of the uncertainties in 40 eigenvector basis PDF sets. Assuming that the error of the unpolarized PDF on LO is approximately the same as NLO, uncertainty on the CTEQ6.1M parameterization is assigned as uncertainty on the CTEQ5L parameterization. To estimate the uncertainties of the quark helicity distributions due to the error on the unpolarized PDF, 40 purities were produced with 40 eigenvector basis PDF sets. Then 40 times production of the quark helicity distributions were performed. According to the uncertainty calculation provided by CTEQ group, the effect of the uncertainties on the final quark helicity distributions were evaluated.

The first moments of the helicity distribution in the measured region were evaluated at $Q^2 = 2.5\mathrm{GeV}^2$:

$$\begin{array}{rcrcll} \Delta u & = & 0.601 & \pm & 0.066 & (3.3\sigma_{PDF}) \\ \Delta d & = & -0.226 & \pm & 0.065 & (4.1\sigma_{PDF}) \\ \Delta \bar{u} & = & -0.002 & \pm & 0.044 & (3.7\sigma_{PDF}) \\ \Delta \bar{d} & = & -0.054 & \pm & 0.038 & (2.5\sigma_{PDF}) \\ \Delta s & = & 0.028 & \pm & 0.035 & (4.4\sigma_{PDF}) \end{array} \tag{7.1}$$

It was confirmed that the effect of the uncertainties on the first moments were sufficiently small.

To summarize, the hadron identification was carried out in the full momentum range at HERMES for the first time. Using these data, the quark helicity distributions were extracted with much higher precision than earlier experiments. The positive u quark polarization and the negative d quark polarization with respect to the proton spin are observed with good accuracy. It should be stressed that this flavor decomposition was done x bin by bin, thanks to the asymmetries data from semi-inclusive hadron measurement. The five parameter fit $(\Delta u, \Delta d, \Delta s, \Delta \bar{u}, \Delta \bar{d})$ was performed in the present analysis, which is less restrictive than any of earlier experiment.

Acknowledgements

First of all, I would like to thank my supervisor Prof. Toshi-Aki Shibata. He introduced me to the physics of quarks and gluons, and gave me the opportunity to participate the analysis group of the helicity distributions at HERMES. He kindly arranged so that I can stay at DESY for about two years. I appreciate him for giving me detailed advice on my analysis.

I would like to thank Dr. Yoshiyuki Miyachi. He spent so much time to give me the introduction of programming and gave me a lot of ingenious ideas for the analysis. For his tremendous supports I managed to finish my thesis.

I would like to thank all the members in my analysis group for many fruitful discussions and advices. I would especially like to thank Dr. Marc Beckmann who was actually my teacher during my stay in DESY. My analysis codes are based on his ones. He always answered my questions kindly and encouraged me. I would also like to thank Dr. Jürgen Wendland. Mutual cross checking between us was very useful for improvements in the analysis. Discussions with HERMES collaborators during my stay at DESY were very helpful. I would like to thank Mr. Hidekazu Tanaka. Several discussions with him were helpful to me.

I would like to thank all the members in my laboratory. I would like to express my special thanks to Mr. Yoshimitsu Imazu who helped making some plots for my thesis.

At last, I would like to thank Dr. Elke Aschenauer who is spokesperson of HERMES. She devoted great efforts to run the experiment.

Appendix A

Tables

GeV/c	P_{π}^{π}	P_{π}^{K}	P_{π}^{p}	P_{π}^{X}	P_{K}^{π}	$P_{\mathrm{K}}^{\mathrm{K}}$	$P_{\mathrm{K}}^{\mathrm{p}}$	$P_{\mathrm{K}}^{\mathrm{X}}$	P_{p}^{π}	$P_{\mathrm{p}}^{\mathrm{K}}$	$P_{\mathrm{p}}^{\mathrm{p}}$	$P_{\mathrm{p}}^{\mathrm{X}}$
	1track											
2.0 – 3.0	0.964	0.012	0.024	0.000	0.031	0.796	0.174	0.000	0.036	0.025	0.939	0.000
3.0 – 4.0	0.914	0.012	0.018	0.056	0.011	0.958	0.025	0.006	0.012	0.031	0.812	0.145
4.0 – 5.0	0.972	0.015	0.001	0.013	0.008	0.969	0.011	0.013	0.005	0.020	0.807	0.169
5.0 – 6.0	0.988	0.008	0.000	0.003	0.007	0.975	0.009	0.008	0.005	0.015	0.953	0.027
6.0 – 7.0	0.994	0.005	0.000	0.001	0.005	0.973	0.018	0.004	0.004	0.026	0.958	0.012
7.0 – 8.0	0.996	0.003	0.000	0.001	0.004	0.952	0.041	0.003	0.003	0.062	0.928	0.008
8.0 – 9.0	0.997	0.002	0.000	0.001	0.003	0.916	0.080	0.002	0.002	0.111	0.882	0.005
9.0 – 10.0	0.998	0.002	0.000	0.000	0.006	0.871	0.120	0.003	0.002	0.167	0.826	0.004
10.0 – 11.0	0.996	0.002	0.002	0.000	0.018	0.497	0.485	0.000	0.002	0.014	0.984	0.000
11.0 – 12.0	0.982	0.017	0.001	0.000	0.071	0.745	0.183	0.000	0.001	0.000	0.998	0.000
12.0 – 13.0	0.950	0.049	0.001	0.000	0.159	0.774	0.067	0.000	0.001	0.001	0.998	0.000
13.0 – 14.0	0.921	0.078	0.001	0.000	0.235	0.736	0.030	0.000	0.002	0.000	0.998	0.000
14.0 – 15.0	0.887	0.113	0.001	0.000	0.298	0.690	0.012	0.000	0.000	0.001	0.999	0.000

GeV/c	δP_{π}^{π}	$\delta P_{\pi}^{\mathrm{K}}$	$\delta P_{\pi}^{\mathrm{p}}$	$\delta P_{\pi}^{\mathrm{X}}$	$\delta P_{\mathrm{K}}^{\pi}$	$\delta P_{\mathrm{K}}^{\mathrm{K}}$	$\delta P_{\mathrm{K}}^{\mathrm{p}}$	$\delta P_{\mathrm{K}}^{\mathrm{X}}$	$\delta P_{\mathrm{p}}^{\pi}$	$\delta P_{\mathrm{p}}^{\mathrm{K}}$	$\delta P_{\mathrm{p}}^{\mathrm{p}}$	$\delta P_{\mathrm{p}}^{\mathrm{X}}$
	1track											
2.0 – 3.0	0.000	0.001	0.000	0.000	0.002	0.000	0.002	0.000	0.001	0.000	0.000	0.000
3.0 – 4.0	0.001	0.000	0.000	0.000	0.002	0.002	0.000	0.000	0.001	0.000	0.000	0.001
4.0 – 5.0	0.000	0.000	0.000	0.000	0.001	0.001	0.001	0.001	0.001	0.000	0.006	0.005
5.0 – 6.0	0.000	0.000	0.000	0.000	0.001	0.001	0.001	0.000	0.001	0.000	0.004	0.004
6.0 – 7.0	0.000	0.000	0.000	0.000	0.001	0.001	0.000	0.001	0.001	0.003	0.005	0.002
7.0 – 8.0	0.000	0.000	0.000	0.000	0.001	0.006	0.005	0.000	0.001	0.006	0.008	0.001
8.0 – 9.0	0.000	0.000	0.000	0.000	0.000	0.007	0.006	0.001	0.001	0.010	0.012	0.001
9.0 – 10.0	0.000	0.000	0.000	0.000	0.001	0.009	0.010	0.000	0.000	0.010	0.012	0.001
10.0 – 11.0	0.001	0.001	0.000	0.000	0.001	0.009	0.010	0.000	0.001	0.002	0.002	0.000
11.0 – 12.0	0.003	0.003	0.000	0.000	0.006	0.012	0.006	0.000	0.000	0.000	0.000	0.000
12.0 – 13.0	0.007	0.006	0.000	0.000	0.009	0.013	0.004	0.000	0.000	0.000	0.001	0.000
13.0 – 14.0	0.008	0.008	0.000	0.000	0.011	0.015	0.004	0.000	0.001	0.000	0.001	0.000
14.0 – 15.0	0.012	0.012	0.000	0.000	0.020	0.020	0.000	0.000	0.000	0.000	0.000	0.000

Table A.1: P-matrix for 1 track extracted by the Monte Carlo simulation.

GeV/c	P_{π}^{π}	P_{π}^{K}	P_{π}^{p}	P_{π}^{X}	P_{K}^{π}	$P_{\mathrm{K}}^{\mathrm{K}}$	$P_{\mathrm{K}}^{\mathrm{p}}$	$P_{\mathrm{K}}^{\mathrm{X}}$	P_{p}^{π}	$P_{\mathrm{p}}^{\mathrm{K}}$	$P_{\mathrm{p}}^{\mathrm{p}}$	$P_{\mathrm{p}}^{\mathrm{X}}$
	2tracks											
2.0 – 3.0	0.869	0.089	0.042	0.000	0.181	0.645	0.174	0.000	0.308	0.230	0.462	0.000
3.0 – 4.0	0.842	0.064	0.029	0.065	0.094	0.858	0.037	0.010	0.151	0.313	0.398	0.138
4.0 – 5.0	0.953	0.020	0.005	0.022	0.077	0.821	0.081	0.021	0.084	0.173	0.585	0.158
5.0 – 6.0	0.981	0.011	0.002	0.005	0.087	0.812	0.087	0.014	0.085	0.128	0.751	0.035
6.0 – 7.0	0.990	0.007	0.001	0.002	0.077	0.819	0.095	0.009	0.081	0.120	0.782	0.017
7.0 – 8.0	0.993	0.006	0.001	0.001	0.070	0.828	0.097	0.005	0.079	0.116	0.796	0.009
8.0 – 9.0	0.995	0.004	0.001	0.001	0.075	0.800	0.123	0.003	0.079	0.139	0.771	0.011
9.0 – 10.0	0.997	0.002	0.001	0.000	0.066	0.790	0.141	0.003	0.077	0.212	0.706	0.005
10.0 – 11.0	0.990	0.008	0.002	0.000	0.058	0.414	0.528	0.000	0.051	0.036	0.913	0.001
11.0 – 12.0	0.976	0.022	0.002	0.000	0.104	0.641	0.255	0.000	0.048	0.022	0.930	0.000
12.0 – 13.0	0.949	0.050	0.001	0.000	0.188	0.715	0.096	0.000	0.053	0.031	0.916	0.000
13.0 – 14.0	0.911	0.086	0.003	0.000	0.261	0.692	0.048	0.000	0.041	0.029	0.930	0.000
14.0 – 15.0	0.886	0.112	0.002	0.000	0.326	0.640	0.034	0.000	0.030	0.031	0.939	0.000

GeV/c	δP_{π}^{π}	$\delta P_{\pi}^{\mathrm{K}}$	$\delta P_{\pi}^{\mathrm{p}}$	$\delta P_{\pi}^{\mathrm{X}}$	$\delta P_{\mathrm{K}}^{\pi}$	$\delta P_{\mathrm{K}}^{\mathrm{K}}$	$\delta P_{\mathrm{K}}^{\mathrm{p}}$	$\delta P_{\mathrm{K}}^{\mathrm{X}}$	$\delta P_{\mathrm{p}}^{\pi}$	$\delta P_{\mathrm{p}}^{\mathrm{K}}$	$\delta P_{\mathrm{p}}^{\mathrm{p}}$	$\delta P_{\mathrm{p}}^{\mathrm{X}}$
	2tracks											
2.0 – 3.0	0.000	0.000	0.000	0.000	0.003	0.004	0.001	0.000	0.005	0.004	0.009	0.000
3.0 – 4.0	0.001	0.000	0.000	0.000	0.004	0.002	0.001	0.000	0.001	0.005	0.005	0.001
4.0 – 5.0	0.001	0.001	0.000	0.000	0.002	0.004	0.001	0.001	0.003	0.002	0.006	0.005
5.0 – 6.0	0.000	0.000	0.000	0.000	0.005	0.006	0.000	0.001	0.003	0.004	0.007	0.000
6.0 – 7.0	0.000	0.000	0.000	0.000	0.006	0.009	0.003	0.000	0.003	0.002	0.005	0.000
7.0 – 8.0	0.000	0.000	0.000	0.000	0.005	0.002	0.008	0.000	0.002	0.008	0.007	0.001
8.0 – 9.0	0.000	0.000	0.000	0.000	0.005	0.002	0.006	0.000	0.006	0.006	0.000	0.000
9.0 – 10.0	0.000	0.000	0.000	0.000	0.001	0.010	0.010	0.001	0.006	0.003	0.007	0.002
10.0 – 11.0	0.000	0.000	0.000	0.000	0.001	0.020	0.021	0.000	0.003	0.001	0.002	0.000
11.0 – 12.0	0.003	0.003	0.000	0.000	0.003	0.001	0.002	0.000	0.007	0.000	0.006	0.000
12.0 – 13.0	0.002	0.003	0.000	0.000	0.014	0.015	0.001	0.000	0.006	0.007	0.013	0.000
13.0 – 14.0	0.010	0.009	0.001	0.000	0.012	0.013	0.002	0.000	0.009	0.002	0.010	0.000
14.0 – 15.0	0.006	0.005	0.001	0.000	0.005	0.013	0.009	0.000	0.009	0.001	0.008	0.000

Table A.2: P-matrix for 2 tracks extracted by the Monte Carlo simulation.

GeV/c	P_{π}^{π}	P_{π}^{K}	P_{π}^{p}	P_{π}^{X}	P_{K}^{π}	$P_{\mathrm{K}}^{\mathrm{K}}$	$P_{\mathrm{K}}^{\mathrm{p}}$	$P_{\mathrm{K}}^{\mathrm{X}}$	P_{p}^{π}	$P_{\mathrm{p}}^{\mathrm{K}}$	$P_{\mathrm{p}}^{\mathrm{p}}$	$P_{\mathrm{p}}^{\mathrm{X}}$
	more											
2.0 – 3.0	0.844	0.120	0.036	0.000	0.236	0.620	0.144	0.000	0.396	0.265	0.339	0.000
3.0 – 4.0	0.819	0.095	0.024	0.062	0.113	0.832	0.047	0.009	0.177	0.393	0.303	0.128
4.0 – 5.0	0.947	0.026	0.007	0.019	0.103	0.768	0.103	0.026	0.087	0.256	0.535	0.122
5.0 – 6.0	0.979	0.013	0.003	0.005	0.128	0.743	0.118	0.010	0.113	0.175	0.688	0.025
6.0 – 7.0	0.989	0.007	0.001	0.003	0.101	0.757	0.137	0.005	0.100	0.163	0.729	0.009
7.0 – 8.0	0.996	0.003	0.001	0.001	0.101	0.753	0.145	0.001	0.106	0.158	0.726	0.009
8.0 – 9.0	0.996	0.003	0.001	0.000	0.108	0.736	0.134	0.022	0.101	0.168	0.701	0.030
9.0 – 10.0	0.997	0.002	0.000	0.000	0.072	0.745	0.176	0.007	0.167	0.213	0.613	0.006
10.0 – 11.0	0.985	0.012	0.003	0.000	0.120	0.404	0.476	0.000	0.096	0.042	0.863	0.000
11.0 – 12.0	0.963	0.031	0.006	0.000	0.141	0.658	0.201	0.000	0.048	0.026	0.926	0.000
12.0 – 13.0	0.950	0.046	0.004	0.000	0.296	0.678	0.026	0.000	0.044	0.025	0.932	0.000
13.0 – 14.0	0.903	0.095	0.001	0.000	0.209	0.742	0.048	0.000	0.064	0.016	0.921	0.000
14.0 – 15.0	0.891	0.109	0.000	0.000	0.367	0.617	0.016	0.000	0.000	0.034	0.966	0.000

GeV/c	δP_{π}^{π}	$\delta P_{\pi}^{\mathrm{K}}$	$\delta P_{\pi}^{\mathrm{p}}$	$\delta P_{\pi}^{\mathrm{X}}$	$\delta P_{\mathrm{K}}^{\pi}$	$\delta P_{\mathrm{K}}^{\mathrm{K}}$	$\delta P_{\mathrm{K}}^{\mathrm{p}}$	$\delta P_{\mathrm{K}}^{\mathrm{X}}$	$\delta P_{\mathrm{p}}^{\pi}$	$\delta P_{\mathrm{p}}^{\mathrm{K}}$	$\delta P_{\mathrm{p}}^{\mathrm{p}}$	$\delta P_{\mathrm{p}}^{\mathrm{X}}$
	more											
2.0 – 3.0	0.002	0.002	0.001	0.000	0.008	0.013	0.005	0.000	0.003	0.005	0.001	0.000
3.0 – 4.0	0.001	0.000	0.000	0.000	0.007	0.003	0.006	0.001	0.000	0.004	0.008	0.003
4.0 – 5.0	0.000	0.001	0.000	0.001	0.004	0.005	0.002	0.004	0.001	0.009	0.012	0.003
5.0 – 6.0	0.000	0.000	0.000	0.001	0.008	0.002	0.006	0.000	0.010	0.008	0.019	0.001
6.0 – 7.0	0.000	0.000	0.000	0.000	0.002	0.002	0.000	0.000	0.002	0.001	0.001	0.002
7.0 – 8.0	0.001	0.001	0.000	0.000	0.007	0.000	0.007	0.001	0.006	0.007	0.001	0.001
8.0 – 9.0	0.001	0.001	0.000	0.000	0.023	0.023	0.005	0.004	0.004	0.012	0.010	0.006
9.0 – 10.0	0.000	0.000	0.000	0.000	0.007	0.017	0.014	0.004	0.033	0.019	0.017	0.003
10.0 – 11.0	0.002	0.001	0.001	0.000	0.005	0.020	0.025	0.000	0.004	0.001	0.003	0.000
11.0 – 12.0	0.010	0.008	0.002	0.000	0.009	0.001	0.010	0.000	0.011	0.007	0.018	0.000
12.0 – 13.0	0.008	0.006	0.002	0.000	0.046	0.058	0.013	0.000	0.009	0.002	0.007	0.000
13.0 – 14.0	0.010	0.011	0.001	0.000	0.032	0.055	0.023	0.000	0.004	0.007	0.004	0.000
14.0 – 15.0	0.009	0.009	0.000	0.000	0.064	0.056	0.007	0.000	0.000	0.016	0.016	0.000

Table A.3: P-matrix for 3 tracks extracted by the Monte Carlo simulation.

x	N^{π^+}	N^{K^+}	$\frac{N^{K^+}}{N^{\pi^+}}$	N^p	$\frac{N^p}{N^{\pi^+}}$	N^{π^-}	N^{K^-}	$\frac{N^{K^-}}{N^{\pi^-}}$	$N^{\bar{p}}$	$\frac{N^{\bar{p}}}{N^{\pi^-}}$
0.033	60693	10548	17.4%	7335	12.1%	52516	5646	10.8%	1915	3.6%
0.047	70103	13129	18.7%	9572	13.7%	58352	6090	10.4%	1836	3.1%
0.064	70374	14050	20.0%	10257	14.6%	57391	5836	10.2%	1723	3.0%
0.086	56963	12199	21.4%	8689	15.3%	45008	4520	10.0%	1321	2.9%
0.118	49192	11112	22.6%	8208	16.7%	37803	3672	9.7%	1172	3.1%
0.165	31226	7298	23.4%	5643	18.1%	22784	2232	9.8%	650	2.9%
0.237	15394	3729	24.2%	3233	21.0%	10664	943	8.8%	268	2.5%
0.338	3169	801	25.3%	726	22.9%	2096	176	8.4%	40	1.9%
0.447	684	152	22.2%	158	23.1%	442	38	8.6%	8	1.8%

Table A.4: The ratio of kaon and proton fluxes to pion flux.

x	$\left(\frac{\Delta N}{N}\right)^{\overrightarrow{\Leftarrow}}_{\pi^+}$	$\left(\frac{\Delta N}{N}\right)^{\overrightarrow{\Rightarrow}}_{\pi^+}$	$\left(\frac{\Delta N}{N}\right)^{Tot}_{\pi^+}$	$\left(\frac{\Delta N}{N}\right)^{\overrightarrow{\Leftarrow}}_{\pi^-}$	$\left(\frac{\Delta N}{N}\right)^{\overrightarrow{\Rightarrow}}_{\pi^-}$	$\left(\frac{\Delta N}{N}\right)^{Tot}_{\pi^-}$
0.033	1.163	1.160	1.161	1.435	1.452	1.443
0.047	1.049	1.026	1.038	1.232	1.223	1.227
0.064	0.926	0.928	0.927	1.143	1.120	1.132
0.086	0.905	0.860	0.883	1.077	1.123	1.100
0.117	0.847	0.859	0.853	1.102	1.107	1.104
0.165	0.837	0.809	0.823	0.957	1.018	0.988
0.237	0.758	0.754	0.756	0.976	0.975	0.975
0.337	0.688	0.809	0.753	0.843	0.832	0.837
0.449	0.586	0.499	0.540	0.753	0.751	0.752
x	$\left(\frac{\Delta N}{N}\right)^{\overrightarrow{\Leftarrow}}_{K^+}$	$\left(\frac{\Delta N}{N}\right)^{\overrightarrow{\Rightarrow}}_{K^+}$	$\left(\frac{\Delta N}{N}\right)^{Tot}_{K^+}$	$\left(\frac{\Delta N}{N}\right)^{\overrightarrow{\Leftarrow}}_{K^-}$	$\left(\frac{\Delta N}{N}\right)^{\overrightarrow{\Rightarrow}}_{K^-}$	$\left(\frac{\Delta N}{N}\right)^{Tot}_{K^-}$
0.033	6.147	5.852	5.997	11.265	11.352	11.308
0.047	4.895	4.451	4.667	9.763	9.653	9.708
0.064	3.784	3.909	3.848	9.379	9.074	9.225
0.086	3.559	2.687	3.110	8.741	9.665	9.197
0.118	3.129	2.820	2.971	9.542	10.369	9.953
0.164	2.349	2.950	2.656	8.074	9.322	8.710
0.236	2.546	2.411	2.476	9.515	9.957	9.741
0.337	2.864	2.719	2.782	6.223	9.134	7.557
0.447	3.003	0.731	1.700	13.869	5.639	8.202
x	$\left(\frac{\Delta N}{N}\right)^{\overrightarrow{\Leftarrow}}_{p}$	$\left(\frac{\Delta N}{N}\right)^{\overrightarrow{\Rightarrow}}_{p}$	$\left(\frac{\Delta N}{N}\right)^{Tot}_{p}$	$\left(\frac{\Delta N}{N}\right)^{\overrightarrow{\Leftarrow}}_{\bar{p}}$	$\left(\frac{\Delta N}{N}\right)^{\overrightarrow{\Rightarrow}}_{\bar{p}}$	$\left(\frac{\Delta N}{N}\right)^{Tot}_{\bar{p}}$
0.033	1.608	1.735	1.668	6.238	6.103	6.163
0.047	1.424	1.587	1.504	7.312	6.529	6.913
0.064	1.543	1.213	1.368	6.324	6.694	6.508
0.087	1.243	2.038	1.630	6.190	6.205	6.190
0.117	1.059	1.588	1.318	5.195	4.363	4.776
0.164	1.715	0.917	1.286	5.601	4.274	4.925
0.238	0.822	1.085	0.945	4.511	5.104	4.805
0.333	0.458	0.774	0.550	16.053	8.434	10.868
0.422	0.558	1.899	1.258	4.563	12.127	6.375

Table A.5: The fractional uncertainties of the hadron yield.

x	P_u^{inc}	$P_{\bar{u}}^{inc}$	P_d^{inc}	$P_{\bar{d}}^{inc}$	P_s^{inc}	$P_{\bar{s}}^{inc}$
0.033	0.5790	0.2034	0.1123	0.0583	0.0236	0.0234
0.048	0.6087	0.1803	0.1135	0.0541	0.0217	0.0218
0.065	0.6402	0.1566	0.1150	0.0491	0.0197	0.0194
0.087	0.6760	0.1305	0.1155	0.0442	0.0169	0.0170
0.118	0.7186	0.0997	0.1154	0.0383	0.0141	0.0140
0.166	0.7714	0.0670	0.1112	0.0293	0.0105	0.0106
0.240	0.8267	0.0421	0.1006	0.0178	0.0065	0.0063
0.340	0.8736	0.0259	0.0864	0.0076	0.0033	0.0033
0.447	0.9078	0.0135	0.0727	0.0029	0.0015	0.0015
x	$P_u^{\pi^+}$	$P_{\bar{u}}^{\pi^+}$	$P_d^{\pi^+}$	$P_{\bar{d}}^{\pi^+}$	$P_s^{\pi^+}$	$P_{\bar{s}}^{\pi^+}$
0.033	0.6476	0.1690	0.0831	0.0683	0.0143	0.0176
0.047	0.6782	0.1493	0.0780	0.0655	0.0118	0.0172
0.065	0.7121	0.1295	0.0731	0.0606	0.0094	0.0152
0.087	0.7481	0.1059	0.0680	0.0576	0.0073	0.0131
0.118	0.7912	0.0786	0.0640	0.0506	0.0056	0.0101
0.166	0.8421	0.0519	0.0570	0.0381	0.0037	0.0073
0.239	0.8895	0.0312	0.0484	0.0244	0.0021	0.0044
0.338	0.9315	0.0190	0.0371	0.0097	0.0008	0.0018
0.450	0.9602	0.0088	0.0265	0.0035	0.0003	0.0008
x	$P_u^{\pi^-}$	$P_{\bar{u}}^{\pi^-}$	$P_d^{\pi^-}$	$P_{\bar{d}}^{\pi^-}$	$P_s^{\pi^-}$	$P_{\bar{s}}^{\pi^-}$
0.033	0.5172	0.2523	0.1445	0.0513	0.0160	0.0187
0.047	0.5314	0.2375	0.1504	0.0488	0.0143	0.0176
0.064	0.5480	0.2194	0.1594	0.0440	0.0126	0.0165
0.087	0.5674	0.1981	0.1693	0.0414	0.0100	0.0138
0.118	0.6027	0.1621	0.1813	0.0352	0.0076	0.0110
0.165	0.6580	0.1169	0.1814	0.0287	0.0058	0.0092
0.238	0.7199	0.0788	0.1751	0.0172	0.0035	0.0055
0.338	0.7690	0.0518	0.1668	0.0084	0.0015	0.0025
0.447	0.8002	0.0294	0.1659	0.0029	0.0005	0.0012
x	$P_u^{K^+}$	$P_{\bar{u}}^{K^+}$	$P_d^{K^+}$	$P_{\bar{d}}^{K^+}$	$P_s^{K^+}$	$P_{\bar{s}}^{K^+}$
0.033	0.6158	0.1479	0.0999	0.0430	0.0160	0.0774
0.047	0.6512	0.1274	0.0951	0.0360	0.0130	0.0773
0.065	0.6957	0.0983	0.0888	0.0319	0.0095	0.0757
0.087	0.7421	0.0738	0.0807	0.0267	0.0063	0.0704
0.118	0.7753	0.0545	0.0799	0.0205	0.0055	0.0644
0.166	0.8295	0.0336	0.0693	0.0145	0.0035	0.0497
0.239	0.8755	0.0215	0.0586	0.0100	0.0020	0.0324
0.338	0.9187	0.0103	0.0480	0.0027	0.0009	0.0193
0.449	0.9530	0.0029	0.0333	0.0008	0.0002	0.0098
x	$P_u^{K^-}$	$P_{\bar{u}}^{K^-}$	$P_d^{K^-}$	$P_{\bar{d}}^{K^-}$	$P_s^{K^-}$	$P_{\bar{s}}^{K^-}$
0.033	0.4824	0.2497	0.0920	0.0618	0.0919	0.0224
0.047	0.4810	0.2339	0.0860	0.0572	0.1219	0.0200
0.065	0.4752	0.2317	0.0820	0.0539	0.1420	0.0152
0.087	0.4891	0.2174	0.0787	0.0514	0.1489	0.0145
0.118	0.5256	0.1901	0.0794	0.0472	0.1455	0.0123
0.165	0.5972	0.1461	0.0814	0.0403	0.1255	0.0095
0.237	0.6796	0.1111	0.0770	0.0298	0.0970	0.0055
0.336	0.7660	0.0855	0.0693	0.0160	0.0603	0.0029
0.443	0.8191	0.0593	0.0677	0.0073	0.0426	0.0039

Table A.6: The purities for the proton target as a function of x.

x	P_u^{inc}	$P_{\bar{u}}^{inc}$	P_d^{inc}	$P_{\bar{d}}^{inc}$	P_s^{inc}	$P_{\bar{s}}^{inc}$
0.033	0.4864	0.2510	0.1570	0.0548	0.0254	0.0254
0.048	0.5000	0.2361	0.1671	0.0495	0.0236	0.0238
0.065	0.5128	0.2213	0.1788	0.0438	0.0218	0.0215
0.087	0.5280	0.2031	0.1929	0.0371	0.0196	0.0194
0.118	0.5440	0.1813	0.2116	0.0296	0.0167	0.0167
0.166	0.5609	0.1492	0.2424	0.0212	0.0132	0.0132
0.239	0.5716	0.1006	0.2946	0.0149	0.0093	0.0090
0.338	0.5685	0.0496	0.3606	0.0107	0.0052	0.0053
0.445	0.5444	0.0219	0.4217	0.0064	0.0027	0.0028
x	$P_u^{\pi^+}$	$P_{\bar{u}}^{\pi^+}$	$P_d^{\pi^+}$	$P_{\bar{d}}^{\pi^+}$	$P_s^{\pi^+}$	$P_{\bar{s}}^{\pi^+}$
0.033	0.5713	0.2040	0.1280	0.0617	0.0163	0.0187
0.047	0.5938	0.1871	0.1296	0.0584	0.0139	0.0172
0.065	0.6155	0.1708	0.1338	0.0525	0.0121	0.0154
0.087	0.6424	0.1531	0.1350	0.0461	0.0098	0.0136
0.118	0.6666	0.1338	0.1423	0.0388	0.0074	0.0111
0.165	0.6947	0.1076	0.1558	0.0280	0.0057	0.0083
0.238	0.7159	0.0710	0.1843	0.0200	0.0034	0.0054
0.337	0.7317	0.0333	0.2169	0.0138	0.0015	0.0028
0.446	0.7423	0.0137	0.2332	0.0087	0.0007	0.0015
x	$P_u^{\pi^-}$	$P_{\bar{u}}^{\pi^-}$	$P_d^{\pi^-}$	$P_{\bar{d}}^{\pi^-}$	$P_s^{\pi^-}$	$P_{\bar{s}}^{\pi^-}$
0.033	0.3952	0.3204	0.1962	0.0505	0.0166	0.0213
0.047	0.3872	0.3192	0.2110	0.0468	0.0147	0.0211
0.064	0.3766	0.3188	0.2318	0.0410	0.0125	0.0193
0.087	0.3699	0.3098	0.2561	0.0365	0.0106	0.0172
0.118	0.3664	0.2931	0.2894	0.0278	0.0080	0.0153
0.165	0.3712	0.2505	0.3394	0.0212	0.0059	0.0117
0.237	0.3682	0.1812	0.4232	0.0153	0.0038	0.0083
0.337	0.3460	0.0928	0.5425	0.0115	0.0018	0.0055
0.446	0.2905	0.0407	0.6596	0.0059	0.0011	0.0024
x	$P_u^{K^+}$	$P_{\bar{u}}^{K^+}$	$P_d^{K^+}$	$P_{\bar{d}}^{K^+}$	$P_s^{K^+}$	$P_{\bar{s}}^{K^+}$
0.033	0.5280	0.1801	0.1492	0.0406	0.0191	0.0830
0.047	0.5440	0.1649	0.1541	0.0353	0.0140	0.0877
0.065	0.5790	0.1411	0.1553	0.0281	0.0113	0.0852
0.087	0.6086	0.1192	0.1543	0.0218	0.0084	0.0877
0.118	0.6292	0.1006	0.1628	0.0167	0.0071	0.0836
0.165	0.6536	0.0786	0.1824	0.0100	0.0050	0.0704
0.237	0.6729	0.0499	0.2182	0.0076	0.0031	0.0484
0.337	0.6824	0.0216	0.2558	0.0046	0.0017	0.0340
0.444	0.6693	0.0073	0.2989	0.0031	0.0010	0.0203
x	$P_u^{K^-}$	$P_{\bar{u}}^{K^-}$	$P_d^{K^-}$	$P_{\bar{d}}^{K^-}$	$P_s^{K^-}$	$P_{\bar{s}}^{K^-}$
0.033	0.3799	0.3053	0.1318	0.0566	0.1034	0.0230
0.047	0.3618	0.3101	0.1309	0.0500	0.1249	0.0224
0.065	0.3404	0.3186	0.1334	0.0448	0.1444	0.0183
0.086	0.3219	0.3314	0.1344	0.0420	0.1552	0.0151
0.117	0.3251	0.3280	0.1480	0.0345	0.1526	0.0117
0.165	0.3384	0.3095	0.1723	0.0268	0.1418	0.0112
0.236	0.3626	0.2521	0.2261	0.0207	0.1309	0.0076
0.334	0.3863	0.1653	0.3210	0.0191	0.1027	0.0056
0.440	0.3959	0.1017	0.4143	0.0136	0.0722	0.0024

Table A.7: The purities for the neutron target as a function of x.

x	$\Delta P_u^{\pi^+}$	$\Delta P_{\bar{u}}^{\pi^+}$	$\Delta P_d^{\pi^+}$	$\Delta P_{\bar{d}}^{\pi^+}$	$\Delta P_s^{\pi^+}$	$\Delta P_{\bar{s}}^{\pi^+}$
0.033	0.0014	0.0021	-0.0038	0.0026	-0.0013	-0.0010
0.048	0.0184	-0.0087	-0.0065	0.0009	-0.0015	-0.0026
0.065	0.0249	-0.0151	-0.0068	0.0014	-0.0018	-0.0025
0.087	0.0262	-0.0147	-0.0072	-0.0010	-0.0014	-0.0020
0.118	0.0225	-0.0131	-0.0050	-0.0027	-0.0006	-0.0012
0.166	0.0149	-0.0079	-0.0047	-0.0007	-0.0004	-0.0012
0.239	0.0118	-0.0039	-0.0040	-0.0023	-0.0005	-0.0011
0.338	0.0046	-0.0030	-0.0007	-0.0007	-0.0001	0.0000
0.449	-0.0031	0.0000	0.0030	0.0004	-0.0002	-0.0002
x	$\Delta P_u^{\pi^-}$	$\Delta P_{\bar{u}}^{\pi^-}$	$\Delta P_d^{\pi^-}$	$\Delta P_{\bar{d}}^{\pi^-}$	$\Delta P_s^{\pi^-}$	$\Delta P_{\bar{s}}^{\pi^-}$
0.033	-0.0289	0.0252	0.0060	0.0004	-0.0013	-0.0013
0.047	-0.0352	0.0243	0.0172	-0.0024	-0.0021	-0.0019
0.064	-0.0344	0.0202	0.0213	-0.0012	-0.0029	-0.0028
0.087	-0.0349	0.0145	0.0280	-0.0038	-0.0021	-0.0016
0.118	-0.0271	0.0100	0.0227	-0.0035	-0.0012	-0.0009
0.165	-0.0297	0.0060	0.0294	-0.0032	-0.0009	-0.0016
0.238	-0.0265	0.0054	0.0241	-0.0011	-0.0009	-0.0010
0.338	-0.0189	0.0043	0.0159	-0.0010	-0.0002	0.0000
0.448	-0.0153	0.0035	0.0121	-0.0001	-0.0003	-0.0001
x	ΔP_u^{K+}	$\Delta P_{\bar{u}}^{K+}$	ΔP_d^{K+}	$\Delta P_{\bar{d}}^{K+}$	ΔP_s^{K+}	$\Delta P_{\bar{s}}^{K+}$
0.033	-0.0054	-0.0195	-0.0040	-0.0040	-0.0050	0.0379
0.048	0.0066	-0.0259	-0.0115	-0.0065	-0.0046	0.0418
0.065	0.0018	-0.0161	-0.0096	-0.0081	-0.0035	0.0356
0.087	0.0025	-0.0129	-0.0161	-0.0065	-0.0011	0.0342
0.118	0.0061	-0.0093	-0.0186	-0.0024	-0.0019	0.0260
0.166	0.0046	-0.0053	-0.0127	-0.0015	-0.0013	0.0161
0.238	0.0024	-0.0029	-0.0100	-0.0030	-0.0008	0.0142
0.338	0.0050	-0.0013	-0.0085	-0.0007	-0.0006	0.0062
0.448	-0.0049	0.0029	0.0002	-0.0004	0.0006	0.0017
x	$\Delta P_u^{K^-}$	$\Delta P_{\bar{u}}^{K^-}$	$\Delta P_d^{K^-}$	$\Delta P_{\bar{d}}^{K^-}$	$\Delta P_s^{K^-}$	$\Delta P_{\bar{s}}^{K^-}$
0.033	-0.0870	0.0335	-0.0144	0.0032	0.0642	0.0002
0.047	-0.1067	0.0502	-0.0185	0.0039	0.0711	0.0000
0.064	-0.0978	0.0515	-0.0269	0.0042	0.0667	0.0024
0.086	-0.1141	0.0627	-0.0196	0.0019	0.0670	0.0022
0.117	-0.0865	0.0433	-0.0239	0.0039	0.0629	0.0001
0.164	-0.0941	0.0459	-0.0186	0.0058	0.0601	0.0009
0.237	-0.0562	0.0360	-0.0158	-0.0003	0.0336	0.0027
0.336	-0.0643	0.0356	-0.0038	0.0017	0.0273	0.0036
0.445	-0.0060	0.0237	-0.0251	-0.0012	0.0108	-0.0021

Table A.8: The systematic uncertainty on the purities for the proton target due to the fragmentation model.

x	$\Delta P_u^{\pi^+}$	$\Delta P_{\bar{u}}^{\pi^+}$	$\Delta P_d^{\pi^+}$	$\Delta P_{\bar{d}}^{\pi^+}$	$\Delta P_s^{\pi^+}$	$\Delta P_{\bar{s}}^{\pi^+}$
0.033	-0.0074	0.0064	0.0134	-0.0013	-0.0059	-0.0052
0.047	-0.0124	0.0026	0.0310	-0.0131	-0.0040	-0.0042
0.065	-0.0155	0.0017	0.0403	-0.0195	-0.0036	-0.0035
0.087	-0.0165	0.0013	0.0427	-0.0208	-0.0031	-0.0036
0.118	-0.0173	-0.0019	0.0441	-0.0204	-0.0021	-0.0024
0.165	-0.0188	-0.0003	0.0397	-0.0172	-0.0019	-0.0015
0.237	-0.0210	-0.0012	0.0364	-0.0122	-0.0010	-0.0010
0.337	-0.0283	-0.0006	0.0336	-0.0036	-0.0004	-0.0006
0.446	-0.0152	0.0010	0.0157	-0.0012	-0.0001	-0.0003

x	$\Delta P_u^{\pi^-}$	$\Delta P_{\bar{u}}^{\pi^-}$	$\Delta P_d^{\pi^-}$	$\Delta P_{\bar{d}}^{\pi^-}$	$\Delta P_s^{\pi^-}$	$\Delta P_{\bar{s}}^{\pi^-}$
0.033	-0.0016	0.0003	-0.0178	0.0286	-0.0051	-0.0047
0.047	0.0095	-0.0022	-0.0197	0.0196	-0.0030	-0.0042
0.065	0.0161	-0.0022	-0.0218	0.0135	-0.0028	-0.0027
0.087	0.0190	-0.0039	-0.0218	0.0125	-0.0022	-0.0037
0.118	0.0210	-0.0021	-0.0176	0.0023	-0.0011	-0.0025
0.165	0.0241	-0.0027	-0.0159	-0.0031	-0.0006	-0.0018
0.238	0.0226	-0.0014	-0.0079	-0.0114	-0.0007	-0.0012
0.337	0.0071	-0.0026	0.0037	-0.0067	-0.0003	-0.0013
0.447	-0.0282	0.0000	0.0341	-0.0056	-0.0004	-0.0001

x	ΔP_u^{K+}	$\Delta P_{\bar{u}}^{K+}$	ΔP_d^{K+}	$\Delta P_{\bar{d}}^{K+}$	ΔP_s^{K+}	$\Delta P_{\bar{s}}^{K+}$
0.033	-0.0097	-0.0057	0.0129	-0.0119	-0.0089	0.0233
0.048	-0.0222	-0.0080	0.0339	-0.0363	-0.0046	0.0372
0.065	-0.0224	-0.0077	0.0204	-0.0336	-0.0039	0.0471
0.087	-0.0215	-0.0059	0.0252	-0.0326	-0.0027	0.0375
0.118	-0.0235	-0.0046	0.0180	-0.0255	-0.0020	0.0376
0.165	-0.0227	-0.0020	0.0226	-0.0198	-0.0019	0.0238
0.237	-0.0231	-0.0022	0.0146	-0.0132	-0.0011	0.0248
0.338	-0.0185	-0.0022	0.0184	-0.0078	0.0003	0.0096
0.444	-0.0148	-0.0016	0.0107	0.0015	0.0000	0.0043

x	ΔP_u^{K-}	$\Delta P_{\bar{u}}^{K-}$	ΔP_d^{K-}	$\Delta P_{\bar{d}}^{K-}$	ΔP_s^{K-}	$\Delta P_{\bar{s}}^{K-}$
0.033	-0.0285	0.0120	-0.0713	0.0528	0.0408	-0.0058
0.047	-0.0310	0.0071	-0.0982	0.0539	0.0721	-0.0041
0.064	-0.0307	0.0057	-0.0990	0.0648	0.0606	-0.0014
0.086	-0.0361	0.0023	-0.0884	0.0630	0.0615	-0.0023
0.117	-0.0321	0.0019	-0.0947	0.0685	0.0545	0.0020
0.165	-0.0374	0.0033	-0.0877	0.0725	0.0495	-0.0001
0.235	-0.0296	0.0075	-0.0938	0.0745	0.0420	-0.0006
0.334	-0.0276	0.0056	-0.0568	0.0550	0.0192	0.0045
0.439	-0.0154	0.0018	-0.0355	0.0410	0.0081	-0.0002

Table A.9: The systematic uncertainty on the purities for a neutron target due to the fragmentation model.

x	$\Delta P_u^{\pi^+}$	$\Delta P_{\bar{u}}^{\pi^+}$	$\Delta P_d^{\pi^+}$	$\Delta P_{\bar{d}}^{\pi^+}$	$\Delta P_s^{\pi^+}$	$\Delta P_{\bar{s}}^{\pi^+}$
0.033	0.0242	0.0169	0.0037	0.0056	0.0020	0.0024
0.047	0.0221	0.0158	0.0039	0.0055	0.0012	0.0017
0.064	0.0200	0.0140	0.0038	0.0054	0.0010	0.0014
0.086	0.0175	0.0120	0.0036	0.0052	0.0008	0.0011
0.117	0.0142	0.0099	0.0032	0.0051	0.0006	0.0009
0.164	0.0111	0.0077	0.0025	0.0047	0.0005	0.0007
0.234	0.0087	0.0053	0.0025	0.0038	0.0004	0.0006
0.347	0.0068	0.0050	0.0027	0.0034	0.0001	0.0004
0.431	0.0055	0.0035	0.0033	0.0020	0.0001	0.0006
x	$\Delta P_u^{\pi^-}$	$\Delta P_{\bar{u}}^{\pi^-}$	$\Delta P_d^{\pi^-}$	$\Delta P_{\bar{d}}^{\pi^-}$	$\Delta P_s^{\pi^-}$	$\Delta P_{\bar{s}}^{\pi^-}$
0.033	0.0252	0.0222	0.0066	0.0039	0.0021	0.0023
0.047	0.0238	0.0218	0.0073	0.0038	0.0013	0.0015
0.064	0.0228	0.0210	0.0076	0.0036	0.0010	0.0013
0.086	0.0210	0.0196	0.0080	0.0035	0.0009	0.0011
0.117	0.0188	0.0183	0.0078	0.0037	0.0008	0.0010
0.165	0.0164	0.0161	0.0071	0.0033	0.0007	0.0009
0.231	0.0146	0.0131	0.0076	0.0028	0.0005	0.0007
0.334	0.0151	0.0129	0.0107	0.0021	0.0003	0.0006
0.454	0.0200	0.0114	0.0180	0.0017	0.0006	0.0004
x	$\Delta P_u^{K^+}$	$\Delta P_{\bar{u}}^{K^+}$	$\Delta P_d^{K^+}$	$\Delta P_{\bar{d}}^{K^+}$	$\Delta P_s^{K^+}$	$\Delta P_{\bar{s}}^{K^+}$
0.033	0.0257	0.0135	0.0044	0.0032	0.0017	0.0103
0.047	0.0220	0.0119	0.0045	0.0030	0.0010	0.0078
0.064	0.0197	0.0105	0.0043	0.0027	0.0007	0.0071
0.086	0.0169	0.0082	0.0039	0.0023	0.0006	0.0068
0.116	0.0137	0.0066	0.0035	0.0021	0.0005	0.0060
0.163	0.0103	0.0047	0.0028	0.0019	0.0003	0.0048
0.226	0.0080	0.0034	0.0027	0.0012	0.0003	0.0035
0.326	0.0056	0.0021	0.0030	0.0007	0.0003	0.0026
0.445	0.0053	0.0022	0.0043	0.0000	0.0000	0.0018
x	$\Delta P_u^{K^-}$	$\Delta P_{\bar{u}}^{K^-}$	$\Delta P_d^{K^-}$	$\Delta P_{\bar{d}}^{K^-}$	$\Delta P_s^{K^-}$	$\Delta P_{\bar{s}}^{K^-}$
0.033	0.0293	0.0189	0.0053	0.0039	0.0111	0.0018
0.048	0.0281	0.0193	0.0051	0.0036	0.0094	0.0013
0.065	0.0275	0.0194	0.0049	0.0035	0.0088	0.0009
0.086	0.0267	0.0192	0.0048	0.0034	0.0091	0.0007
0.117	0.0255	0.0198	0.0048	0.0039	0.0089	0.0006
0.163	0.0247	0.0195	0.0044	0.0041	0.0088	0.0007
0.234	0.0248	0.0183	0.0042	0.0033	0.0092	0.0006
0.336	0.0267	0.0226	0.0057	0.0027	0.0100	0.0004
0.449	0.0280	0.0226	0.0043	0.0000	0.0126	0.0000

Table A.10: The systematic uncertainty on the purities for the proton target due to the systematic uncertainty on the unpolarized PDFs.

x	$\Delta P_u^{\pi^+}$	$\Delta P_{\bar{u}}^{\pi^+}$	$\Delta P_d^{\pi^+}$	$\Delta P_{\bar{d}}^{\pi^+}$	$\Delta P_s^{\pi^+}$	$\Delta P_{\bar{s}}^{\pi^+}$
0.033	0.0072	0.0061	0.0180	0.0138	0.0021	0.0024
0.047	0.0071	0.0059	0.0182	0.0140	0.0014	0.0016
0.064	0.0069	0.0056	0.0185	0.0140	0.0011	0.0013
0.086	0.0067	0.0052	0.0182	0.0137	0.0009	0.0012
0.116	0.0062	0.0047	0.0171	0.0136	0.0008	0.0010
0.164	0.0062	0.0043	0.0154	0.0128	0.0006	0.0009
0.234	0.0081	0.0039	0.0141	0.0109	0.0005	0.0007
0.322	0.0131	0.0038	0.0167	0.0098	0.0004	0.0006
0.467	0.0231	0.0043	0.0273	0.0082	0.0006	0.0011

x	$\Delta P_u^{\pi^-}$	$\Delta P_{\bar{u}}^{\pi^-}$	$\Delta P_d^{\pi^-}$	$\Delta P_{\bar{d}}^{\pi^-}$	$\Delta P_s^{\pi^-}$	$\Delta P_{\bar{s}}^{\pi^-}$
0.033	0.0116	0.0046	0.0167	0.0185	0.0020	0.0024
0.047	0.0120	0.0043	0.0172	0.0198	0.0012	0.0017
0.064	0.0122	0.0040	0.0180	0.0206	0.0009	0.0014
0.086	0.0125	0.0036	0.0182	0.0215	0.0008	0.0012
0.117	0.0126	0.0033	0.0176	0.0226	0.0006	0.0010
0.164	0.0136	0.0031	0.0163	0.0233	0.0005	0.0009
0.235	0.0170	0.0027	0.0155	0.0233	0.0005	0.0008
0.329	0.0240	0.0031	0.0194	0.0277	0.0006	0.0006
0.441	0.0330	0.0009	0.0298	0.0332	0.0009	0.0014

x	$\Delta P_u^{K^+}$	$\Delta P_{\bar{u}}^{K^+}$	$\Delta P_d^{K^+}$	$\Delta P_{\bar{d}}^{K^+}$	$\Delta P_s^{K^+}$	$\Delta P_{\bar{s}}^{K^+}$
0.033	0.0085	0.0034	0.0192	0.0112	0.0018	0.0100
0.047	0.0081	0.0032	0.0185	0.0113	0.0011	0.0080
0.064	0.0077	0.0027	0.0184	0.0106	0.0008	0.0075
0.086	0.0071	0.0022	0.0180	0.0098	0.0007	0.0075
0.118	0.0068	0.0018	0.0167	0.0093	0.0006	0.0069
0.161	0.0066	0.0015	0.0151	0.0085	0.0004	0.0066
0.236	0.0086	0.0012	0.0139	0.0066	0.0003	0.0060
0.324	0.0139	0.0007	0.0171	0.0053	0.0003	0.0050
0.445	0.0259	0.0000	0.0287	0.0014	0.0000	0.0078

x	$\Delta P_u^{K^-}$	$\Delta P_{\bar{u}}^{K^-}$	$\Delta P_d^{K^-}$	$\Delta P_{\bar{d}}^{K^-}$	$\Delta P_s^{K^-}$	$\Delta P_{\bar{s}}^{K^-}$
0.034	0.0091	0.0043	0.0205	0.0141	0.0107	0.0022
0.048	0.0091	0.0040	0.0201	0.0156	0.0092	0.0012
0.065	0.0088	0.0038	0.0206	0.0168	0.0082	0.0009
0.086	0.0087	0.0035	0.0207	0.0184	0.0078	0.0006
0.118	0.0089	0.0035	0.0208	0.0206	0.0076	0.0007
0.163	0.0104	0.0035	0.0211	0.0235	0.0076	0.0006
0.233	0.0144	0.0035	0.0232	0.0271	0.0088	0.0007
0.331	0.0267	0.0032	0.0284	0.0420	0.0133	0.0008
0.424	0.0389	0.0126	0.0489	0.0587	0.0267	0.0000

Table A.11: The systematic uncertainty on the purities for a neutron target due to the systematic unertainty on the unpolarized PDFs.

x	Q^2	A_p	σ_{stat}	σ_{syst}			
0.033	1.22	0.0996	0.0176	0.0091			
0.048	1.45	0.1102	0.0175	0.0093			
0.065	1.68	0.1131	0.0181	0.0088			
0.087	1.93	0.1941	0.0208	0.0143			
0.118	2.34	0.2366	0.0205	0.0178			
0.166	3.16	0.2819	0.0216	0.0208			
0.240	4.54	0.3854	0.0239	0.0283			
0.340	6.56	0.4760	0.0430	0.0344			
0.447	9.18	0.6102	0.0750	0.0467			
x	Q^2	$A_p^{h^+}$	$\sigma_{stat}^{h^+}$	$\sigma_{syst}^{h^+}$	$A_p^{h^-}$	$\sigma_{stat}^{h^-}$	$\sigma_{syst}^{h^-}$
0.034	1.21	0.1097	0.0299	0.0077	0.0724	0.0341	0.0054
0.048	1.44	0.1640	0.0316	0.0113	0.1262	0.0365	0.0087
0.065	1.72	0.1361	0.0329	0.0096	0.0901	0.0382	0.0057
0.087	2.06	0.2075	0.0370	0.0147	0.0953	0.0442	0.0066
0.118	2.58	0.3011	0.0356	0.0212	0.1860	0.0445	0.0135
0.166	3.52	0.2851	0.0384	0.0209	0.1770	0.0498	0.0127
0.239	5.03	0.4223	0.0456	0.0292	0.2360	0.0639	0.0165
0.338	7.09	0.4046	0.0914	0.0291	0.5696	0.1339	0.0387
0.448	9.76	0.7586	0.1756	0.0519	0.4957	0.2715	0.0341
x	Q^2	$A_p^{\pi^+}$	$\sigma_{stat}^{\pi^+}$	$\sigma_{syst}^{\pi^+}$	$A_p^{\pi^-}$	$\sigma_{stat}^{\pi^-}$	$\sigma_{syst}^{\pi^-}$
0.033	1.22	0.0800	0.0353	0.0058	0.0675	0.0388	0.0053
0.047	1.50	0.1336	0.0387	0.0091	0.1450	0.0431	0.0095
0.064	1.87	0.0829	0.0408	0.0067	0.0649	0.0461	0.0039
0.087	2.38	0.2312	0.0459	0.0157	0.0714	0.0536	0.0047
0.118	3.08	0.3163	0.0458	0.0212	0.0754	0.0547	0.0057
0.166	4.22	0.3017	0.0525	0.0201	0.1572	0.0645	0.0105
0.238	5.83	0.2784	0.0695	0.0197	0.2696	0.0889	0.0187
0.337	7.97	0.5566	0.1530	0.0373	0.3461	0.1995	0.0233
0.449	10.49	0.8651	0.3185	0.0558	0.4490	0.4343	0.0352

Table A.12: The Born asymmetries for the proton target.

x	Q^2	A_d	σ_{stat}	σ_{syst}	σ_{RICH}				
0.033	1.22	0.0203	0.0078	0.0015					
0.048	1.45	0.0248	0.0080	0.0017					
0.065	1.69	0.0396	0.0085	0.0023					
0.087	1.95	0.0440	0.0100	0.0031					
0.118	2.35	0.0777	0.0099	0.0054					
0.166	3.18	0.1137	0.0107	0.0081					
0.240	4.55	0.1621	0.0121	0.0114					
0.339	6.58	0.2932	0.0228	0.0195					
0.446	9.16	0.3161	0.0412	0.0236					
x	Q^2	$A_d^{h^+}$	$\sigma_{stat}^{h^+}$	$\sigma_{syst}^{h^+}$	$\sigma_{RICH}^{h^+}$	$A_d^{h^-}$	$\sigma_{stat}^{h^-}$	$\sigma_{syst}^{h^-}$	$\sigma_{RICH}^{h^-}$
0.033	1.21	0.0080	0.0146	0.0007		-0.0125	0.0162	0.0013	
0.048	1.44	0.0112	0.0156	0.0018		0.0074	0.0174	0.0014	
0.065	1.73	0.0484	0.0162	0.0028		0.0380	0.0185	0.0022	
0.087	2.07	0.0754	0.0185	0.0043		0.0179	0.0212	0.0033	
0.118	2.60	0.0350	0.0179	0.0038		0.0739	0.0213	0.0040	
0.166	3.56	0.1326	0.0194	0.0087		0.0775	0.0245	0.0065	
0.238	5.04	0.1469	0.0237	0.0104		0.1712	0.0315	0.0103	
0.338	7.12	0.2372	0.0504	0.0151		0.3001	0.0700	0.0175	
0.446	9.61	0.1901	0.0995	0.0149		0.1499	0.1481	0.0128	
x	Q^2	$A_d^{\pi^+}$	$\sigma_{stat}^{\pi^+}$	$\sigma_{syst}^{\pi^+}$	$\sigma_{RICH}^{\pi^+}$	$A_d^{\pi^-}$	$\sigma_{stat}^{\pi^-}$	$\sigma_{syst}^{\pi^-}$	$\sigma_{RICH}^{\pi^-}$
0.033	1.22	-0.0172	0.0175	0.0011	0.0084	-0.0113	0.0183	0.0014	0.0029
0.047	1.50	0.0180	0.0192	0.0022	0.0027	-0.0231	0.0203	0.0012	0.0134
0.064	1.87	0.0130	0.0201	0.0016	0.0050	0.0457	0.0218	0.0028	0.0154
0.087	2.36	0.0449	0.0226	0.0029	0.0007	0.0056	0.0245	0.0020	0.0168
0.118	3.07	0.0966	0.0223	0.0061	0.0096	0.0884	0.0249	0.0045	0.0079
0.165	4.18	0.1207	0.0257	0.0079	0.0013	0.0144	0.0298	0.0035	0.0309
0.238	5.80	0.1089	0.0343	0.0073	0.0166	0.2039	0.0413	0.0116	0.0004
0.338	7.93	0.3179	0.0815	0.0202	0.0416	0.3860	0.0988	0.0209	0.0388
0.446	10.24	0.0856	0.1695	0.0115	0.0038	-0.1323	0.2159	0.0182	0.0492
x	Q^2	$A_d^{K^+}$	$\sigma_{stat}^{K^+}$	$\sigma_{syst}^{K^+}$	$\sigma_{RICH}^{K^+}$	$A_d^{K^-}$	$\sigma_{stat}^{K^-}$	$\sigma_{syst}^{K^-}$	$\sigma_{RICH}^{K^-}$
0.033	1.22	0.0048	0.0479	0.0022	0.0205	-0.0471	0.0597	0.0039	0.0309
0.048	1.50	0.0171	0.0496	0.0043	0.0355	0.0312	0.0661	0.0041	0.0054
0.065	1.86	0.1469	0.0504	0.0083	0.0347	0.0097	0.0701	0.0051	0.0198
0.086	2.33	0.1220	0.0561	0.0079	0.0013	-0.0554	0.0811	0.0046	0.0198
0.118	3.08	0.0399	0.0534	0.0046	0.0120	0.0292	0.0830	0.0029	0.0206
0.165	4.23	0.1436	0.0593	0.0104	0.0099	0.0722	0.0993	0.0069	0.0012
0.238	5.81	0.1445	0.0773	0.0120	0.0052	0.0871	0.1411	0.0067	0.0278
0.336	7.76	0.4389	0.1747	0.0270	0.0125	-0.2504	0.3422	0.0202	0.1089
0.448	10.20	0.4641	0.3692	0.0400	0.0866	1.4585	0.7001	0.0859	0.0258

Table A.13: The Born asymmetries for the deuterium target.

x	$\frac{\Delta u}{u}$	σ_{stat}	σ_{syst}	σ_{PDF}	$x \cdot \Delta u$	σ_{stat}	σ_{syst}	σ_{PDF}
0.033	0.0855	0.1180	0.0856	0.0152	0.0296	0.0409	0.0296	0.0053
0.048	0.1368	0.1107	0.0217	0.0037	0.0515	0.0417	0.0082	0.0014
0.065	0.1913	0.0978	0.0356	0.0062	0.0785	0.0401	0.0146	0.0025
0.087	0.4864	0.0909	0.0784	0.0078	0.2185	0.0408	0.0352	0.0035
0.118	0.5086	0.0774	0.0633	0.0087	0.2525	0.0384	0.0314	0.0043
0.166	0.4731	0.0757	0.0436	0.0078	0.2623	0.0420	0.0242	0.0043
0.239	0.4445	0.0855	0.0364	0.0395	0.2652	0.0510	0.0217	0.0235
0.339	0.5805	0.0650	0.0558	0.0070	0.3241	0.0363	0.0312	0.0039
0.447	0.7272	0.1087	0.0684	0.0120	0.3121	0.0467	0.0294	0.0052
x	$\frac{\Delta d}{d}$	σ_{stat}	σ_{syst}	σ_{PDF}	$x \cdot \Delta d$	σ_{stat}	σ_{syst}	σ_{PDF}
0.033	-0.1236	0.1529	0.0390	0.0144	-0.0337	0.0417	0.0106	0.0039
0.048	0.0588	0.1452	0.0543	0.0050	0.0167	0.0412	0.0154	0.0014
0.065	-0.1336	0.1307	0.0362	0.0059	-0.0394	0.0385	0.0107	0.0018
0.087	-0.2572	0.1303	0.0495	0.0064	-0.0789	0.0400	0.0152	0.0020
0.118	-0.4876	0.1185	0.0841	0.0127	-0.1552	0.0377	0.0268	0.0040
0.166	-0.0918	0.1337	0.0675	0.0073	-0.0296	0.0431	0.0218	0.0024
0.239	-0.5218	0.1646	0.0822	0.0683	-0.1536	0.0485	0.0242	0.0201
0.339	-0.2799	0.1988	0.1694	0.0207	-0.0628	0.0446	0.0380	0.0046
0.447	-0.8133	0.4074	0.2454	0.1141	-0.1158	0.0580	0.0349	0.0162
x	$\frac{\Delta \bar{u}}{\bar{u}}$	σ_{stat}	σ_{syst}	σ_{PDF}	$x \cdot \Delta \bar{u}$	σ_{stat}	σ_{syst}	σ_{PDF}
0.033	0.3382	0.3342	0.2189	0.0310	0.0437	0.0432	0.0283	0.0040
0.048	0.2484	0.3677	0.0471	0.0106	0.0288	0.0426	0.0055	0.0012
0.065	0.0166	0.3938	0.1200	0.0203	0.0017	0.0403	0.0123	0.0021
0.087	-0.7151	0.4585	0.3508	0.0786	-0.0624	0.0400	0.0306	0.0069
0.118	-0.8989	0.5391	0.3395	0.1182	-0.0621	0.0372	0.0235	0.0082
0.166	-0.9022	0.8403	0.3491	0.1835	-0.0432	0.0402	0.0167	0.0088
0.239	1.4742	1.6410	0.3868	0.7165	0.0446	0.0496	0.0117	0.0217
x	$\frac{\Delta \bar{d}}{\bar{d}}$	σ_{stat}	σ_{syst}	σ_{PDF}	$x \cdot \Delta \bar{d}$	σ_{stat}	σ_{syst}	σ_{PDF}
0.033	-0.2281	0.2819	0.0380	0.0334	-0.0338	0.0418	0.0056	0.0049
0.048	-0.6238	0.2921	0.1076	0.0356	-0.0862	0.0404	0.0149	0.0049
0.065	0.0174	0.2847	0.0513	0.0115	0.0022	0.0360	0.0065	0.0015
0.087	-0.2239	0.3103	0.0605	0.0264	-0.0267	0.0370	0.0072	0.0031
0.118	0.5412	0.3144	0.1621	0.0429	0.0577	0.0335	0.0173	0.0046
0.166	-0.9546	0.4561	0.0734	0.1109	-0.0828	0.0396	0.0064	0.0096
0.239	0.4523	0.8380	0.1470	0.4395	0.0237	0.0439	0.0077	0.0230
x	$\frac{\Delta s}{s}$	σ_{stat}	σ_{syst}	σ_{PDF}	$x \cdot \Delta s$	σ_{stat}	σ_{syst}	σ_{PDF}
0.033	0.4734	0.7492	0.1871	0.1323	0.0317	0.0502	0.0125	0.0089
0.048	0.6071	0.6361	0.1952	0.0546	0.0365	0.0382	0.0117	0.0033
0.065	-0.0537	0.5805	0.0441	0.0089	-0.0029	0.0313	0.0024	0.0005
0.087	-0.1243	0.6248	0.1422	0.0320	-0.0059	0.0297	0.0067	0.0015
0.118	-0.3359	0.6516	0.0756	0.0354	-0.0133	0.0258	0.0030	0.0014
0.166	1.3956	0.8851	0.0912	0.1252	0.0418	0.0265	0.0027	0.0037
0.239	-1.2674	1.5039	0.3911	0.1444	-0.0230	0.0273	0.0071	0.0026

Table A.14: The quark polarizations and helicity distribution evaulated at a fixed value of $Q_0^2 = 2.5\ \mathrm{GeV}^2$.

Bibliography

[1] Murray Gell-Mann. A schematic model of baryons and mesons. *Phys. Lett.*, 8:214–215, 1964.

[2] G. Zweig. An SU(3) model for strong interaction symmetry and its breaking. 2. CERN-TH-412.

[3] Richard P. Feynman. Very high-energy collisions of hadrons. *Phys. Rev. Lett.*, 23:1415–1417, 1969.

[4] M. J. Alguard et al. Deep inelastic scattering of polarized electrons by polarized protons. *Phys. Rev. Lett.*, 37:1261, 1976.

[5] M. J. Alguard et al. Deep inelastic e p asymmetry measurements and comparison with the bjorken sum rule and models of the proton spin structure. *Phys. Rev. Lett.*, 41:70, 1978.

[6] Guenter Baum et al. A new measurement of deep inelastic e p asymmetries. *Phys. Rev. Lett.*, 51:1135, 1983.

[7] J. Ashman et al. A measurement of the spin asymmetry and determination of the structure function g_1 in deep inelastic muon proton scattering. *Phys. Lett.*, B206:364, 1988.

[8] J. Ashman et al. An investigation of the spin structure of the proton in deep inelastic scattering of polarized muons on polarized protons. *Nucl. Phys.*, B328:1, 1989.

[9] D. Adams et al. Measurement of the spin dependent structure function $g_1(x)$ of the proton. *Phys. Lett.*, B329:399–406, 1994.

[10] K. Abe et al. Precision measurement of the proton spin structure function g_1^p. *Phys. Rev. Lett.*, 74:346–350, 1995.

[11] K. Abe et al. Precision measurement of the deuteron spin structure function g_1^d. *Phys. Rev. Lett.*, 75:25–28, 1995.

[12] Hideyuki Kobayashi. Study of spin structure of the proton with hadron coincidence measurement of polarized deep inelastic scattering. 2000. PhD thesis, Tokyo Institute of Technology, Japan.

[13] Fumiko Sato. Flavor asymmetry of the polarized light sea quarks from deep inelastic scattering at hermes. 2001. Master thesis, Tokyo Institute of Technology, Japan.

[14] Richard P. Feynman. Photon-hadron interactions. *Reading*, 1972.

[15] John R. Ellis and Robert L. Jaffe. A sum rule for deep inelastic electroproduction from polarized protons. *Phys. Rev.*, D9:1444, 1974.

[16] M. Anselmino, A. Efremov, and E. Leader. The theory and phenomenology of polarized deep inelastic scattering. *Phys. Rept.*, 261:1–124, 1995.

[17] Jr. Callan, Curtis G. and David J. Gross. High-energy electroproduction and the constitution of the electric current. *Phys. Rev. Lett.*, 22:156–159, 1969.

[18] J. J. Aubert et al. Measurement of the deuteron structure function F_2 and a comparison of proton and neutron structure. *Phys. Lett.*, B123:123, 1983.

[19] A. C. Benvenuti et al. A high statistics measurement of the proton structure functions $F_2(x, Q^2)$ and r from deep inelastic muon scattering at high Q^2. *Phys. Lett.*, B223:485, 1989.

[20] M. R. Adams et al. Proton and deuteron structure functions in muon scattering at 470 gev. *Phys. Rev.*, D54:3006–3056, 1996.

[21] M. Arneodo et al. Measurement of the proton and the deuteron structure functions, ${F_2}^p$ and ${F_2}^d$. *Phys. Lett.*, B364:107–115, 1995.

[22] L. W. Whitlow, E. M. Riordan, S. Dasu, Stephen Rock, and A. Bodek. Precise measurements of the proton and deuteron structure functions from a global analysis of the slac deep inelastic electron scattering cross-sections. *Phys. Lett.*, B282:475–482, 1992.

[23] A. Aktas et al. Measurement of the proton structure function F_2 at low Q^2 in qed compton scattering at hera. *Phys. Lett.*, B598:159–171, 2004.

[24] S. Chekanov et al. Measurement of the neutral current cross section and F_2 structure function for deep inelastic e+ p scattering at hera. *Eur. Phys. J.*, C21:443–471, 2001.

[25] J. Breitweg et al. Measurement of the proton structure function F_2 at very low Q^2 at hera. *Phys. Lett.*, B487:53–73, 2000.

[26] Andrew Mehta. Structure function measurements and polarised cross section measurements from hera. 2004.

[27] K. Abe et al. Measurements of $R = \sigma_l/\sigma_t$ for 0.03 $< x <$ 0.1 and fit to world data. *Phys. Lett.*, B452:194–200, 1999.

[28] P. L. Anthony et al. Deep inelastic scattering of polarized electrons by polarized He-3 and the study of the neutron spin structure. *Phys. Rev.*, D54:6620–6650, 1996.

[29] K. Abe et al. Measurements of the proton and deuteron spin structure functions g_1 and g_2. *Phys. Rev.*, D58:112003, 1998.

[30] K. Abe et al. Precision determination of the neutron spin structure function g_1^n. *Phys. Rev. Lett.*, 79:26–30, 1997.

[31] P. L. Anthony et al. Measurement of the deuteron spin structure function $g_1^d(x)$ for 1 $(\mathrm{GeV/c})^2 < Q^2 < 40\ (\mathrm{GeV/c})^2$. *Phys. Lett.*, B463:339–345, 1999.

[32] P. L. Anthony et al. Measurements of the Q^2 dependence of the proton and neutron spin structure functions g_1^p and g_1^n. *Phys. Lett.*, B493:19–28, 2000.

[33] B. Adeva et al. Spin asymmetries A_1 and structure functions g_1 of the proton and the deuteron from polarized high energy muon scattering. *Phys. Rev.*, D58:112001, 1998.

[34] B. Adeva et al. Spin asymmetries A_1 of the proton and the deuteron in the low x and low Q^2 region from polarized high energy muon scattering. *Phys. Rev.*, D60:072004, 1999.

[35] A. Airapetian et al. Measurement of the proton spin structure function g_1^p with a pure hydrogen target. *Phys. Lett.*, B442:484–492, 1998.

[36] K. Ackerstaff et al. Measurement of the neutron spin structure function g_1^n with a polarized He-3 internal target. *Phys. Lett.*, B404:383–389, 1997.

[37] K. Abe et al. Measurement of the proton and deuteron spin structure function g_2 and asymmetry A_2. *Phys. Rev. Lett.*, 76:587–591, 1996.

[38] K. Abe et al. Measurement of the neutron spin structure function g_2^n and asymmetry A_2^n. *Phys. Lett.*, B404:377–382, 1997.

[39] P. L. Anthony et al. Measurement of the proton and deuteron spin structure functions g_2 and asymmetry A_2. *Phys. Lett.*, B458:529–535, 1999.

[40] P. L. Anthony et al. Precision measurement of the proton and deuteron spin structure functions g_2 and asymmetries A_2. *Phys. Lett.*, B553:18–24, 2003.

[41] J. D. Bjorken and Emmanuel A. Paschos. Inelastic electron proton and gamma proton scattering, and the structure of the nucleon. *Phys. Rev.*, 185:1975–1982, 1969.

[42] Edmond L. Berger. Semiinclusive inelastic electron scattering from nuclei. Invited paper to be publ. in Proc. of NPAS Workshop on Electronuclear Physics with Internal Targets, Stanford, CA, Jan 5-8, 1987.

[43] J. P. Albanese et al. Quark charge retention in final state hadrons from deep inelastic muon scattering. *Phys. Lett.*, B144:302, 1984.

[44] C. Caso et al. Review of particle physics. *Eur. Phys. J.*, C3:1–794, 1998.

[45] Y. Goto et al. Polarized parton distribution functions in the nucleon. *Phys. Rev.*, D62:034017, 2000.

[46] M. Arneodo et al. A reevaluation of the gottfried sum. *Phys. Rev.*, D50:1–3, 1994.

[47] S. A. Larin. The next-to-leading QCD approximation to the Ellis-Jaffe sum rule. *Phys. Lett.*, B334:192–198, 1994.

[48] J. D. Bjorken. Applications of the chiral U(6)X(6) algebra of current densities. *Phys. Rev.*, 148:1467–1478, 1966.

[49] B. Adeva et al. Polarised quark distributions in the nucleon from semi- inclusive spin asymmetries. *Phys. Lett.*, B420:180–190, 1998.

[50] K. Ackerstaff et al. Flavor decomposition of the polarized quark distributions in the nucleon from inclusive and semi-inclusive deep- inelastic scattering. *Phys. Lett.*, B464:123–134, 1999.

[51] M. Gluck, E. Reya, M. Stratmann, and W. Vogelsang. Models for the polarized parton distributions of the nucleon. *Phys. Rev.*, D63:094005, 2001.

[52] J. Blumlein and H. Bottcher. QCD analysis of polarized deep inelastic scattering data and parton distributions. *Nucl. Phys.*, B636:225–263, 2002.

[53] M. Hirai, S. Kumano, and N. Saito. AAC analysis of polarized parton distributions with uncertainties. 2004.

[54] A. Airapetian et al. Flavor decomposition of the sea quark helicity distributions in the nucleon from semi-inclusive deep- inelastic scattering. *Phys. Rev. Lett.*, 92:012005, 2004.

[55] A. Airapetian et al. Quark helicity distributions in the nucleon for up, down, and strange quarks from semi-inclusive deep-inelastic scattering. 2004.

[56] A. A. Sokolov and I. M. Ternov. On polarization and spin effects in the theory of synchrotron radiation. *Phys. Dokl.*, 8:1203–1205, 1964.

[57] M. Beckmann et al. The longitudinal polarimeter at hera. *Nucl. Instrum. Meth.*, A479:334–348, 2002.

[58] F. Stock et al. The filtex / hermes polarized hydrogen atomic beam source. *Nucl. Instrum. Meth.*, A343:334–342, 1994.

[59] K. Ackerstaff et al. Hermes spectrometer. *Nucl. Instrum. Meth.*, A417:230–265, 1998.

[60] J. Blouw et al. Design and performance of a large microstrip gas tracker for hermes. *Nucl. Instrum. Meth.*, A434:227–243, 1999.

[61] J. T. Brack et al. The hermes forward tracking chambers: Construction, operation, and aging effects. *Nucl. Instrum. Meth.*, A469:47–54, 2001.

[62] S. Bernreuther et al. The hermes back drift chambers. *Nucl. Instrum. Meth.*, A416:45–58, 1998.

[63] H. Avakian et al. Performance of the electromagnetic calorimeter of the hermes experiment. *Nucl. Instrum. Meth.*, A417:69–78, 1998.

[64] H. Avakian et al. Performance of f101 radiation resistant lead glass shower counters. *Nucl. Instrum. Meth.*, A378:155–161, 1996.

[65] H. Tanaka et al. A gain monitoring system with a nd:yag laser for the photomultipliers of the hermes experiment. *Nucl. Instrum. Meth.*, A515:725–732, 2003.

[66] N. Akopov et al. The hermes dual-radiator ring imaging cerenkov detector. *Nucl. Instrum. Meth.*, A479:511–530, 2002.

[67] T. Ypsilantis and J. Seguinot. Theory of ring imaging cherenkov counters. *Nucl. Instrum. Meth.*, A343:30–51, 1994.

[68] E. Aschenauer et al. Optical characterization of n = 1.03 silica aerogel used as radiator in the rich of hermes. *Nucl. Instrum. Meth.*, A440:338–347, 2000.

[69] H. Yokogawa and M. Yokoyama. Hydrophobic sillica aerogels. *Journal of NonCrystaline Solids*, 186:23, 1995.

[70] I. Adachi et al. Study of a threshold cherenkov counter based on silica aerogels with low refractive indices. *Nucl. Instrum. Meth.*, A355:390–398, 1995.

[71] F. Sato. Study of the rich mirror reflectivity. 2000. HERMES-RICH-Internal Note 00-011.

[72] Y. Miyachi. Aerogel tile effect study in the rich program using the experiment data. 2002. HERMES-RICH-Internal Note 02-04.

[73] I. McLaren et al. Epio - experimental physics input output package. *CERN Program Library Long Writeup*, pages 1–101, 1993.

[74] CERN Programming Techniques Group. Adamo(aleph data model) - an entity relationship programming system. *CERN Program Library Long Writeup*, Version 3.3, 1994.

[75] Wander Wolfgang. Reconstruction of high-energy scattering events in the hermes experiment. (in german). DESY-HERMES-96-23.

[76] P. J. Mulders and R. D. Tangerman. The complete tree-level result up to order 1/q for polarized deep-inelastic leptoproduction. *Nucl. Phys.*, B461:197–237, 1996.

[77] K. A. Oganessyan, L. S. Asilyan, M. Anselmino, and E. De Sanctis. Spin-independent and double-spin cos(phi) asymmetries in semi-inclusive pion electroproduction. *Phys. Lett.*, B564:60–64, 2003.

[78] R. Brun et al. Geant - detector description and simulation tool. *CERN program library*, page Writeup W5013, 1993.

[79] I. Akushevich, H. Bottcher, and D. Ryckbosch. Radgen 1.0: Monte carlo generator for radiative events in dis on polarized and unpolarized targets. 1998.

[80] I. V. Akushevich and N. M. Shumeiko. Radiative effects in deep inelastic scattering of polarized leptons by polarized light nuclei. *J. Phys.*, G20:513–530, 1994.

[81] I. Akushevich, A. Ilichev, N. Shumeiko, A. Soroko, and A. Tolkachev. Polrad 2.0: Fortran code for the radiative corrections calculation to deep inelastic scattering of polarized particles. *Comput. Phys. Commun.*, 104:201–244, 1997.

[82] B. Desplanques. Deuteron d state probability and energy dependent n n interactions. *Phys. Lett.*, B203:200–204, 1988.

[83] R. Machleidt, K. Holinde, and C. Elster. The bonn meson exchange model for the nucleon nucleon interaction. *Phys. Rept.*, 149:1–89, 1987.

[84] S. K. Singh, W. Leidemann, and H. Arenhovel. The role of electromagnetic form-factors in meson exchange currents. *Z. Phys.*, A331:509–518, 1988.

[85] G. Ingelman, A. Edin, and J. Rathsman. Lepto 6.5 - a monte carlo generator for deep inelastic lepton-nucleon scattering. *Comput. Phys. Commun.*, 101:108–134, 1997.

[86] Torbjorn Sjostrand. High-energy physics event generation with pythia 5.7 and jetset 7.4. *Comput. Phys. Commun.*, 82:74–90, 1994.

[87] Felix M. Menden. Determination of the gluon polarization in the nucleon. DESY-THESIS-2001-060.

[88] Bo Andersson, G. Gustafson, G. Ingelman, and T. Sjostrand. Parton fragmentation and string dynamics. *Phys. Rept.*, 97:31, 1983.

[89] R. D. Field and R. P. Feynman. A parametrization of the properties of quark jets. *Nucl. Phys.*, B136:1, 1978.

[90] H. L. Lai et al. Global QCD analysis of parton structure of the nucleon: Cteq5 parton distributions. *Eur. Phys. J.*, C12:375–392, 2000.

[91] M. Gluck, E. Reya, and A. Vogt. Dynamical parton distributions revisited. *Eur. Phys. J.*, C5:461–470, 1998.

[92] Alan D. Martin, R. G. Roberts, W. James Stirling, and R. S. Thorne. Parton distributions: A new global analysis. *Eur. Phys. J.*, C4:463–496, 1998.

[93] J. Pumplin et al. New generation of parton distributions with uncertainties from global QCD analysis. *JHEP*, 07:012, 2002.

[94] Daniel Stump et al. Inclusive jet production, parton distributions, and the search for new physics. *JHEP*, 10:046, 2003.

[95] J. Wendland. Polarized parton distributions measured at the hermes experiment. *AIP Conf. Proc.*, 698:595–598, 2004.

[96] R. J. Barlow. A gauide to the use of statistical methods in the physical sciences. 1989.

[97] M. Wakamatsu. A chiral theory of light-flavor sea-quark distributions in the nucleon. 2002.

[98] S. Kretzer. Fragmentation functions from flavour-inclusive and flavour-tagged e+ e- annihilations. *Phys. Rev.*, D62:054001, 2000.

[99] X. Zheng et al. Precision measurement of the neutron spin asymmetry A_1^n and spin-flavor decomposition in the valence quark region. *Phys. Rev. Lett.*, 92:012004, 2004.